Diverse behavioral representation by neocortical PV interneuron dynamics converges between SI and V1

Alexander Ian More
B.S. Northeastern University, Behavioral Neuroscience

A thesis dissertation submitted in partial fulfillment of the requirements for the degree of
Doctor of Philosophy in the Department of Neuroscience at Brown University

Providence, Rhode Island
May 2023

This dissertation by Alexander Ian More is accepted in its present form by the Department of Neuroscience as satisfying the dissertation requirement for the degree of Doctor of Philosophy.

Date_____   _____
                              Christopher Moore, Ph.D., *Advisor*
                              Department of Neuroscience
                              Brown University

Recommended to the Graduate Council

Date_____   _____
                              Barry Connors, Ph.D., *Reader*
                              Department of Neuroscience
                              Brown University

Date_____   _____
                              David Berson, Ph.D., *Reader*
                              Department of Neuroscience
                              Brown University

Date_____   _____
                              Shane Crandall, Ph.D., *Reader*
                              Department of Physiology
                              Michigan State University

Approved by the Graduate Council

Date_____   _____
                              Thomas A. Lewis, Ph.D.
                              Dean of the Graduate School
                              Brown University

Curriculum Vitae

Alexander Ian More

Education

<u>Brown University</u>   Providence, RI
Ph.D. Degree in Neuroscience   Expected March 2023
Studies: Neural Systems, Cell and Molecular Neuroscience, Cognitive Neuroscience
Mentor: Dr. Christopher Moore
GPA: 4.0

<u>Northeastern University</u>   Boston, MA
Bachelor of Science Degree in Behavioral Neuroscience   August 2014
Honors: Magna Cum Laude 2014, Psi Chi, Nu Rho Psi, Dean's List 2011, 2012, 2014
Studies: Sensation and Perception, Psychopharmacology, Animal Behavior, Stem Cells
GPA: 3.64

Research Experience

<u>Moore Laboratory</u>   January 2016 – Present
Ph.D. Student   Providence, RI
- Actively studied bioluminescent-optogenetics with simultaneous *in vivo* bioluminescent imaging and extracellular electrophysiology
- Facilitated the development of a novel method to control neural activity with bioluminescent light sources
- Currently completing experiments utilizing two-photon microscopy to evaluate neocortical dynamics in the rodent visual system during visual detection
- Performed rodent surgery for chronic *in vivo* experiments, including viral injections, cranial window implantation, and head-fixation
- Analyzed neocortical calcium imaging and electrophysiology data using MATLAB

<u>Pfizer Neuroscience</u>   May 2014 – May 2015
Imaging Technician   Cambridge, MA
- Actively studied calcium channels in NR2B and M1 receptors with confocal microscopy
- Facilitated the development of a high throughput assay to evaluate the NR2B receptor
- Conducted experiments utilizing a spinning-disk confocal system to evaluate calcium flux at the membrane, and various subcellular location
- Maintained cell lines and executed tissue culture protocols, including transfection, bacterial transformation, and promoter induction

<u>Pfizer Neuroscience</u>   July 2013- December 2013
Research Intern   Cambridge, MA
- Actively studied symptoms of schizophrenia and depression in a behavioral assay with model mice
- Designed and conducted behavioral studies to assess motivation of mice in a Progressive Ratio operant procedure
- Performed studies to reverse the effects of dopaminergic antagonists and kappa opioid receptor agonists in the Progressive Ratio operant procedure

- Validated use of Progressive Ratio assay for phenotyping battery and drug screening

<u>NU, Center for Translational Neuroimaging</u>   May 2012- May 2014
Research Assistant   Boston, MA
- Lead a study on Activity-Based Anorexia in Prairie voles
- Actively studied oxytocin in Prairie voles
- Executed fMRI-imaging protocols to study effects of anorexia in Prairie voles
- Performed necessary tasks including acclimation of rats to MRI apparatus, imaging of rats in MRI, as well as monitoring oxytocin levels in Prairie voles

Abstracts and Presentations

More AI, Deister CA, Scott DN, Moore CI. *Diverse behavioral representation in PV interneuron dynamics is conserved across neocortical areas but may diverge between Neocortical layers 2/3 in mice.* Society for Neuroscience Conference. 2022.

More AI, Murphy JW, Lambert GG, Deister CA, Brown T, McKissick O, Torreblanca Zanca A, Gregory DB, Hochgeschwender U, Shaner NC, Moore CI. *Precise and sustained manipulation of selected cell ensembles through photoswitchable Bioluminescent-Optogenetics (PS BL-OG).* Society for Neuroscience Conference. 2021.

More AI, Deister CA, Tulett AR, Moore CI. *Neocortical interneuron subtype dynamics in mouse visual cortex: a potential cortical circuit motif for sensory detection.* Society for Neuroscience Conference. 2019.

More AI, Deister CA, Moore CI. *Parvalbumin-positive interneuron ensemble dynamics in the primary visual cortex during mouse visual detection.* Society for Neuroscience Conference. 2018.

Gomez-Ramirez M, Murphy JW, More AI, Pal A, Lipscombe D, Hochgeschwender U, Moore CI. *Tracking neocortical dynamics using genetically-encoded bioluminescent molecules in vivo.* Society for Neuroscience Conference. 2018.

Moore CI, Sliva DD, Yanagi KS, Oyalowo AC, More AI, Deister CA, Pescosolido M, St. Laurent R, Allen JJ, Lipscombe D, Hart AC. *The Brown University Neuropracticum: Advanced graduate training at the marine biological laboratory.* Society for Neuroscience Conference. 2018.

Gomez-Ramirez M, More AI, Pal A, Connors BW, Kauer JA, Lipscombe D, Hochgeschwender U, Moore CI. *Imaging and regulation of cortical neurons using bioluminescent molecules: A biological method for tracking neural dynamics and driving optogenetic elements in-vivo.* Society for Neuroscience Conference. 2017.

Gomez-Ramirez M, More AI, Kauer J, Connors B, Hochgeschwender U, Moore CI. *Bioluminescent-Optogenetics: A Systematic Investigation of the Neurophysiological Effects of BL-OG in vivo.* Society for Neuroscience Conference. 2016.

Hanks AN, More AI, Hughes ZA. *The Use of Progressive Ratio as a Preclinical Index of Anhedonia.* The Society of Biological Psychiatry. 2014.

Publications

More AI, Deister CA, Moore CI. *Layers II/III of mouse sensory Neocortex diverge in inhibitory behavioral representation during sensory detection.* 2023 in preparation.

Deister CA, Brown TC, Voigts J, More AI, Becheck S, Lichtin R, Moore CI. *Neocortical inhibitory imbalance predicts successful sensory detection.* Cell Reports. 2023 in submission.

Gomez-Ramirez M, More AI, Friedman NG, Hochgeschwender U, Moore CI. *The BioLuminescent-Optogenetics in vivo response to coelenterazine is proportional, sensitive, and specific in Neocortex.* Journal of Neuroscience Research. 2019.

Skills and Interests

Lab Skills *In vivo*:
- Proficient in all methods of rodent brain surgery, including head-fixation, viral injections, cannula implantation, and cranial window implantation; Simultaneous bioluminescent imaging and extracellular electrophysiology; Two-photon imaging during rodent behavior; Conducting behavioral assays, including somatosensory and visual psychophysics and detection in mice; Conducting behavioral assays with voles and rats, including Progressive Ratio and Activity-Based Anorexia; Proficient at mouse, vole, and rat subcutaneous, intraperitoneal, oral gavage dosing

Lab Skills *In vitro*:
- Proficient at tissue culture techniques and maintaining cell lines; DNA transfection and promoter induction; Molecular cloning and bacterial transformation

Lab Skills Imaging and Software:
- Data analysis using MATLAB; Management of large data sets; Proficient at utilizing *MED-PC* software; Data analysis utilizing *Zen*, *Image,* and *GraphPad Prism 5* software

Interests: Playing classical piano, brain science outreach, skiing, performing live music

Volunteer Experience

<u>BrainStation</u>   September 2016 – Present
President and Founder   Providence, RI
- Incorporated an educational non-profit organization to teach brain science to elementary school students
- Developed an age-appropriate curriculum to introduce basic brain science to students in the earliest years of school
- Taught over 3,000 students about the brain and how the nervous system functions
- Created a platform for other volunteers to join BrainStation and conduct outreach
- Implemented promotional content for the non-profit through the website, www.brainstation.us

<u>Frontiers for Young Minds</u>   July 2018 –Present
Science Mentor   Providence, RI
- Mentored middle-school children on the scientific process, including experimental design and peer review
- Conducted a peer review session to allow students to review a current scientific article written by children, for children
- Informed students about careers in scientific research, medicine, and healthcare

<u>Franciscan Children's Hospital</u>   January 2013 – January 2014
Child Life Assistant   Brighton, MA
- Facilitated a positive experience for children staying long-term in a hospital
- Provided social opportunities for patients by playing with the children, or playing music for them

Acknowledgements

My graduate career at Brown University has been the best tenure I've experienced in my professional career. I have worked in numerous neuroscience settings including academic research, pharmaceutical research, and graduate research. The most supportive and thorough mentorship I've received has been in my graduate research, and I have been supported by my mentors in full.

I would first like to thank Dr. Christopher Moore, who allowed me to join his lab at the beginning of my second year of graduate school. I first performed a rotation with Dr. Moore during my spring semester of first year. I found the lab environment to be challenging and stimulating, two qualities I hoped to find in my graduate school lab. Dr. Moore met with me frequently even though I was a rotation student, and we spent several meetings discussing future goals for Bioluminescent-Optogenetics. I was even able to contribute to the BL-OG group with a literature review and preliminary surgeries that facilitated the *in vivo* BL-OG research. Dr. Moore did not initially take me as a full lab member, and I performed a second rotation in the interest of joining his lab. However, he continued to meet with me and provide support, and after this second rotation I became a full lab member.

Dr. Moore has continued to provide immense support for the years of my graduate school career. I have been fortunate to meet with him often and frequently, and I have spent up to three hours per week meeting with him. This occurs through lab meetings, BL-OG meetings, and my personal meeting each week. Dr. Moore has always been available despite his obligations as the Associate Director of the Carney Institute for Brain Science. I routinely discuss science with him after hours or on weekends, and this has greatly improved my capabilities and passion for science. I hope to stay connected with Dr. Moore going forward, both personally and professionally.

I would next like to thank Dr. Manuel Gomez-Ramirez for his mentorship and guidance. Dr. Gomez-Ramirez first allowed me to rotate within the Moore lab, and his support, mentorship, and vocality was the needed step for me to join the Moore lab. Dr. Gomez-Ramirez continued to guide me after I finished my first co-authored paper with him, and to this day we have a strong relationship despite his faculty position in Rochester, New York.

Dr. Christopher Deister was my next post-doctoral mentor during my time in the Moore lab. Dr. Deister not only helped me hone my behavioral training skills, but he taught me the basics of programming and the art of two-photon microscopy. Dr. Deister allowed me to support his paper with my own research, which has led to another co-authorship

from my graduate career. Dr. Deister has not only been supportive to me, but has been a major supporter of the Moore lab in general, having facilitated everything from mentorship, to the building of rigs, to the analysis of data for many lab members.

I would finally like to thank my Mother, Alexis More, without whom I would not have achieved a graduate school career and eventual degree. Alexis has made several sacrifices for me throughout my life, and as a single mother she has made sure that my time as an only child was never one as a lonely child. We are best friends, and her support is invaluable to me. I hope to make her proud with this degree and to alleviate the stress I have put her through during my time in graduate school. I could not ask for a better family, and more specifically a better mother.

Table of Contents

List of Figures and Tables

**Abstract of "Diverse behavioral representation by PV
interneuron dynamics converges between SI and V1"
by Alexander I. More, Ph.D., Brown University, May 2023**

The Neocortex is a complex brain structure that represents the outside world, optimizes

behavior, and provides associations based on prior learning. The Neocortex achieves

these computations through flexible neural representations created by many cell types

and mechanisms. Local inhibitory interneurons are leading contributors, acting through

inhibition to shape excitatory activity. Parvalbumin-positive interneurons (PV) are the

most numerous interneurons in Neocortex and exert powerful local control on signal

relay by neighboring pyramidal cell ensembles. Despite intensive study, substantial

debate exists as to how PV contribute to active processing, with opposing views

regarding the value of their increased versus decreased activity.

In this thesis, I describe the discovery of two distinct PV cell ensembles that show

increased and decreased activity that predicts success in sensory detection, a motif

shared between Primary Somatosensory (SI) and Visual Neocortex (V1). Specifically,

the "Hit" PV ensemble fires more on successfully perceived trials, while the "Miss"

ensemble shows decreased activity. Our modeling suggests that Hit PV receive

contextual signals that they translate into optimal signal relay and improved perception.

Specifically, the model predicts that increased Hit PV firing suppresses Miss PV, in turn

disinhibiting pyramidal neurons and amplifying sensory relay. Further, discoveries I

made in V1 support the view that the Hit PV ensemble is key to contextual behavioral

control. First, I found that Hit PV predominate in Layer II versus Layer III, consistent with

enhanced top-down input. Second, I discovered a substantial population of non-sensory

Hit PV, attuned to context and not the outside world, a feature not found amongst Miss PV.

To study PV selectively, I employed two-photon calcium imaging combined with a threshold-level sensory detection task. To selectively control activity in such genetically-defined cell classes, I helped develop a unique optogenetic-chemogenetic combined molecular control tool, Bioluminescent-Optogenetics (BL-OG). I further helped develop tools for photo-switching BL-OG efficacy 'on' with 2-photon light. This new tool should provide a direct method for selectively controlling specific, functionally-defined ensembles, such as those I discovered in V1.

These results demonstrate a common computational architecture exists among PV cells across Primary Sensory Neocortical areas, and show direct evidence for functional specialization of Layer II versus Layer III.

Chapter 1: Introduction

The Neocortex: A Distinct Mammalian Invention

Mammals are defined by their innate flexibility in behavior and their ability to learn and then rapidly apply that information for survival. Mammals are also defined by a unique brain structure, the Neocortex, which both distinguishes mammals from other vertebrates and has elaborated massively within mammalian evolution (Schroder et al., 1997; Loomba et al., 2022). This structure is known for its numerous cell types, laminar differentiation, and computational columnar units (Ramon y Cajal, 1911; Mountcastle, 1957).

The Mammalian Neocortex: Made of Six Layers

Anatomically, the laminar differentiation of the Neocortex has been well-characterized over more than a century of neuroscience research, with some of its first descriptions being reported in the mid-1800's (Meynert, 1867). Korbinian Brodmann further expanded on this concept by describing localization of function within the Neocortex (Brodmann, 1909). Today, accepted Neocortical areas, and more widely the brain, are still largely based on Brodmann's identification and nomenclature.

The laminar structures that define the Neocortex are the six layers, labeled from layer I as most superficial, to layer VI as furthest from the Neocortical surface. In the Primary Sensory Neocortex, the focus of my doctoral research, these six layers can be further broadly characterized as *granular*, *infragranular,* and *supragranular* layers. The

granular layer, or Layer IV, receives input from the lemniscal thalamus in sensory Neocortex (Hubel and Wiesel, 1962; Hubel et al., 1977; Kleinfeld and Deschenes, 2011). Accordingly, this input layer tends to faithfully represent information, with receptive fields more similar to those of the thalamus (Hubel and Wiesel, 1962; Miller et al., 2001). Output from layer IV is almost entirely intra-columnar (Miller et al., 2001). The infragranular layers, in contrast, make extensive intracortical and subcortical connections (Svoboda and Sheperd, 2005). These Layers V and VI often contain information about execution of action (Sheets and Shepherd, 2011). They also send substantial input to the columnar layers above them, playing a key role in shaping their response to dynamic stimuli (Olsen et al., 2012; Voigts et al., 2020). The supragranular layers, particularly Layers II and III, are the subject of my doctoral research. These layers are generally intracortically interconnected (Petersen et al., 2003). They are also uniquely plastic (Armstrong-James et al., 1994) and, as discussed below and throughout my thesis, are highly context dependent in their activity (Voigts et al., 2020). Voigts et al. (2020) found that deviant stimuli enhanced tactile detection, and that this enhancement was encoded in Layers II/III. These highly specific tuning properties were, in turn, regulated by layer VI activity (Voigts et al., 2020).

Why Did the Neocortex Evolve? For Context-Specific Processing of Learned Information

A standard view of the Neocortex is that it is needed for basic perceptual functions, such as identifying oriented bars in the visual field (Hubel and Wiesel, 1959). Many lines of emerging evidence, however, including the fact that basic perceptual abilities

4

are often exquisite in non-mammals, suggest that it evolved for a different reason (Allman, 1990; Kaas, 2006). This unique machine might serve a unique mammalian skill set: context-specific processing of learned information. For example, the Neocortex demonstrates plasticity and associative models that predict and represent the dimensions of sensory stimuli we encounter (Mountcastle et al., 1957; Sur et al., 1980; Feldman and Brecht, 2005; Palagina et al., 2018). Additionally, the Neocortex contains high-dimensional and flexible neural representations that can represent peripheral signals important for sensory perception and perceptual learning (Glickfeld et al., 2013; Siegle et al., 2014; Rikhye et al., 2017).

How to Implement Flexible Routing: Inhibitory Interneurons

Inhibitory local interneurons are the primary source of inhibition in the brain and regulate local circuit activity in the Neocortex (Alitto and Dan, 2010; Ko et al., 2011; Rudy et al. 2011). Inhibitory interneurons are conserved across mammalian species including the mouse, monkey, and human. In fact, inhibition is critical enough that there is ten-fold greater inhibitory to inhibitory connections in humans compared to mice (Loomba et al. 2022).   Parvalbumin-positive interneurons (PV) are one class of inhibitory cells amongst many, including vasointestinal peptide interneurons and somatostatin-positive interneurons (Rudy et al., 2011; Rikhye et al., 2021).   These PV sculpt cortical circuits in sensory cortices, including the visual Neocortex and somatosensory Neocortex (Lee et al., 2014; Lu et al., 2014; Cardin et al., 2009). Because of PV's role in feed-forward inhibition from sensory thalamus to Neocortex, they are a likely candidate for inhibitory release to facilitate perception (Cruikshank et al., 2007).

One Key Role of Interneuron Inhibition: Feedforward Inhibition

Balanced excitation and inhibition are critical for neural representations throughout the brain, including the Neocortex (Galarreta and Hestrin, 1998; Hirsch et al., 2015). Excitatory pyramidal neurons and inhibitory interneurons are two broad classes of cells in the Neocortex that represent sensory information from the outside world (Hu et al., 2014; Markram et al., 2004; Siegle et al., 2014; Shin and Moore, 2019). These excitatory and inhibitory networks can be altered with the allocation of attention, and excitatory activity must be inhibited to provide balance amongst Neocortical circuits (Kim et al., 2016).

Feedforward inhibition is one of the most common roles attributed to interneurons. As information comes into the neocortex from the lemniscal thalams, it synapses onto both excitatory and inhibitory cells. This prevents runaway excitation as the inhibitory cells are coupled to the excitatory cells. PV cells play a role in feedforward inhibition by mediating the excitation in Layer IV of the Neocortex (Cruikshank et al., 2007). Further, PV cells in primary somatosensory Neocortex (SI) even receive stronger inputs from the thalamus and an increased number of connections compared to pyramidal cells (Cruikshank et al., 2007).

FS/PV: The Largest Class of Inhibitory Interneurons, Ideally Positioned to Gate Information Flow

As mentioned above, PV, fast-spiking cells (PV/FS) are well-positioned to regulate Neocortical dynamics. Genetic methods to label PV in Neocortex almost exclusively

label basket cells and chandelier cells in Layers II/III (Cardin et al., 2009). Basket PV are somatic and often wrap the soma of pyramidal cells with their axonal arbors. Chandelier cells are axo-axonic and contact the axon initial segment of pyramidal cells. Both types, however, provide powerful inhibition of pyramidal cells.

Further, PV are often critical in the emergence of gamma oscillations, which are rhythmic fluctuations in local field potentials in a range broadly spanning 30-100 Hz (Cardin et al., 2009). They are predicted by some to be key to attentional routing of information (Fries et al., 2001). Additionally, selective optogenetic drive of PV are known in mice to induce gamma rhythms and sculpt sensory responsivity, as per their above-described role in thalamic feedforward inhibition and improve attentional processing (Cardin et al. 2009; Sohal et al., 2009; Attalah et al., 2012; Kim et al. 2016). Several studies have tied PV, and their dynamics on single trials, to perceptual success (Siegle et al., 2014; Kim et al., 2016; Shin and Moore 2019). In 2014, Siegle et al. demonstrated stimulation of PV at gamma frequencies could enhance the detection of difficult-to-perceive tactile stimuli.

While these many lines of evidence link PV to perceptual success and, by extension, mammalian flexibility, the functional role of PV cells during behavior remains debated. Several studies demonstrate that PV have suppressive effects on perception and behavioral performance during task behavior (Sachidanandan et al., 2016; Atallah et al., 2012). However, when stimulated with certain parameters PV have been shown to enhance perception (Siegle et al., 2014; Shin and Moore, 2019; Lee et al., 2012).

These findings suggest that PV may play a dual role in both enhancing and suppressing perception, although exactly how remains poorly understood. Theoreticians demonstrate the release of inhibition as an important step for information processing, but the exact pattern of inhibitory activity amongst inhibitory cell types is not as conclusive. PV inhibitory cells provide the gate-keeping mechanism that keeps pyramidal cells balanced during development and matured states (Faglioni et al., 2004; Hirsch et al., 2015).

FS/PV: Also Ideal for Disinhibition? A New Model from Our Lab

The release of inhibition is critical to allow the flow of prioritized information in the Neocortex. This mechanism, disinhibition, allows the release of neurons from somatic hyperpolarization.   There has been strong emphasis on vasointestinal peptide interneurons (VIP cells) and their inhibition of somatostatin positive interneurons (SOM cells). For example, research demonstrates that the disinhibition of pyramidal cells by VIP cell and SOM cell interactions can facilitate perception during active whisking. Specifically, VIP cells recruited by vibrissae motor cortex can disinhibit pyramidal cells in SI carrying perceptually relevant signals (Gentet et al., 2012; Lee et al., 2013). While VIP disinhibition is a canonical circuit motif, PV cells can also have disinhibitory connections.

Recently, a study demonstrated that PV cells emerge into distinct ensembles predictive of successful perception and failed perception during detection tasks (Deister et al., 2023). During this task, behaviorally representative PV ensembles emerged where one

subgroup fired more on successful trials, or hits, during detection, and another subgroup developed that fired less on successful trials and more on failed trials, or misses. These groups were explained by a computational model that demonstrated opponent inhibition as a necessary feature for successful information processing (Deister et al., 2023).

This model is one of top-down imbalance, in which certain PV ensembles are selectively prioritized over others by top-down inputs (Deister et al., 2023). These selected ensembles receive more imbalanced feedback excitation than their counterparts, which are strongly driven by bottom-up, feedforward activity. The model demonstrates that PV will receive balanced feedforward inhibition in the absence of strong top-down feedback. However, when top-down signals prioritize one ensemble above another, this attentional state will cause imbalance amongst the PV groups. This leads to opponent inhibition in which ensembles develop that predict both hits and misses in the detection task. While one ensemble increases firing on Hit trials, the other decreases firing and increases firing on Miss trials.

Layer II versus Layer III: Distinct Nodes for Neocortical Computation?
The Neocortex can also be further divided with some layers being subdivided into sublamina, although Layers II and III are often combined as a single unit (Gur and Snodderly, 2008; Xu and Callaway, 2009; Weiler et al., 2022), as indicated by the designation 'supragranular,' used above. Differences between Layers II/III, a key focus of my work, have been largely ignored. Layers II and III of the rodent Neocortex are not defined by a cytoarchitectural boundary. However, Layer II and Layer III do have

distinct cell morphologies. Neurons in Layer II, specifically pyramidal cells, have a more

ovoid shape and smaller apical dendrites (Peters and Kara, 1985). Layer III pyramidal

cells have an apical dendrite that reaches Layer I in SI (Schroder and Luhmann, 1997).

Additionally, this distinction of a longer apical dendrite in Layer III pyramidal cells holds

in visual Neocortex (Gilbert and Wiesel, 1979).

Transcolumnar and intralaminar pathways have been well characterized in the mouse

between Layers II and III and describe different circuitry. Layer II has dense

intralaminar and transcolumnar arbors in the mouse sensory Neocortex. These arbors

target Layer II and Layer Va, specifically (Svoboda and Shepherd, 2005; Larsen and

Callaway, 2006). Layer II also has a strong Va input that is not as distinct in Layer II

(Lefort et al., 2009). Layer III transcolumnar projections are sparser than Layer II, as

are the intralaminar projections. These target Layer Vb and collaterals in Layer IV

(Svoboda and Shepherd, 2005; Larsen and Callaway, 2006). PV interneuron inputs in

Layer III are dominated by Layer IV with small transcolumnar input. Layer III also

demonstrates strong experience-dependent plasticity (Feldman and Brecht, 2005;

Huang et al., 2009). While Layers II and III depend on context, there must be strong

factors that contribute to differential representations in these Neocortical layers.

Inhibition provides a strong candidate for these differential representations, based on

inhibitory neurons' ability to provide synchronous activity and sensory transformations in

Neocortex (Gibson et al., 1999).

Functional Distinctions Between Layers II and III: Context-Dependent Processing

Importantly, functional differences across the layers have been extensively studied (Jones, 2000; Callaway, 1998; Harris and Shepherd, 2015). Computationally, the superficial layers of Neocortex have strong contextual dependence and attentional drive (Hyvarinen et al., 1980). Hyvarinen et al. discovered that during a primate tactile vibration discrimination task, cells at the border of Layer I and II were highly influenced by attention. Further, the separation of Layers II and III have been newly supported by recent research in the mouse that discriminates between the two layers. In auditory mouse Neocortex, differential representations were discovered that distinguish Layers II and III (Meng et al., 2017). Additionally, a study by Prakash Kara and colleagues found an unexpected dependence of cortical depth on neural activity. This study evaluated the effect of visual grating stimuli in V1, and found that the directional selectivity of neurons in V1 increases with depth. Specifically, they found that directional selectivity is larger in Layer III versus Layer II. Additionally, in the mouse somatosensory Neocortex, functional distinctions during active whisking have also been observed that differ amongst Layer II and III. In this study, Simon Peron's group found that touch responses were sparser and more reliable in Layers II versus Layer III of mouse barrel Neocortex (Voelcker et al., 2022).

The Present Research: Dissecting the Role of FS/PV In Layers II and III in Perceptual Success

To directly address the question of how Layers II and III FS/PV might contribute to perception, we used two-photon imaging in two distinct primary sensory Neocortices. Two-photon imaging uses pulsed laser light to activitate fluorescence of

genetically-identified cell types (Denk et al., 1990). This method is ideal for interneuron population dynamics because of its ability to not only identify large groups of genetically-targeted PV interneurons, but also to record their activity with GCaMP6, a calcium indicator (Chen et al., 2013). In the limitations of this study, GCaMP6 is not a measurement of spiking or voltage changes, but rather of calcium concentration in the cytosol. This is a proxy for activity and not necessarily a reflection of individual action potentials. Additionally, GCaMP6 expression has a low signal-to-noise ratio in PV cells, and these caveats can be addressed with future experiments. Nevertheless, two-photon population imaging of identified PV interneurons expressing GCaMP6 provides a strong method to evaluate the role of PV in perceptual success in Layers II and III.

Chapter 2: The BioLuminescent‑OptoGenetic *in vivo* response to coelenterazine is proportional, sensitive, and specific in Neocortex

This chapter is composed of an original manuscript that I contributed to with Dr. Manuel Gomez-Ramirez and others. I performed surgeries, built a bioluminescence imaging recording apparatus, conducted extracellular electrophysiological recordings, and analyzed control groups for this paper. In 2019 it was accepted for publication in The Journal of Neuroscience Research. Further, I tested and validated new BL-OG constructs that allow for specific activation of activity-defined ensembles. This Chapter highlights the development of tools that will allow us to test hypothesis-driven questions about sensory Neocortex. It contains the original manuscript with a further discussion that highlights the development of a new BL-OG tool that is photoswitchable. The authors of this manuscript are listed below.

Gomez‑Ramirez, M., More, A. I., Friedman, N. G., Hochgeschwender, U., & Moore, C. I. (2019). The bioluminescent‑optogenetic *in vivo* response to coelenterazine is proportional, sensitive, and specific in neocortex. *Journal of Neuroscience Research*, *98*(3), 471–480. https://doi.org/10.1002/jnr.24498

Abstract:

Here, we demonstrate that BL-OG can be used as a gain modulator and that bioluminescence can lead to a corresponding change in neuronal firing of cortical neurons. We show that the BL-OG response is sensitive, specific, and proportional in mouse Neocortex. Additionally, we probed whether BL-OG enhances cell sensitivity to sensory stimuli and whether this construct can be used to dynamically control cell activity *in-vivo.*

To execute these original experiments, we injected the LMO3 construct into mouse primary somatosensory Neocortex (SI) and performed simultaneous bioluminescence imaging and electrophysiological recordings while stimulating the vibrissae of the animal before and after injections of CTZ. Our data demonstrated that BL-OG regulates cell activity systematically in the mouse Neocortex under anesthetized conditions. Bioluminescence is both an optogenetic and chemogenetic method, and with any chemogenetic method it is imperative to identify a dosage regime in which the small molecule driver does not produce off-target effects. In addition to showing that bioluminescence can modulate multi-unit activity (MUA) in the Neocortex of mice, we also identified a dosage regime of CTZ that produced neither off-target effects nor cellular toxicity. While this construct was the first proof of principle that BL-OG can drive MUA *in-vivo* further additions have been made to the BL-OG toolkit that afford different capabilities and neuroscientific questions. One such molecule provides photo-switchable BL-OG and can be controlled temporally with the addition of pulsed light.

BL-OG provides a chemogenetic method for optogenetic manipulation of excitable cells that can regulate broad regions of the brain. Recently, we are developing a photoswitchable (PS) version of BL-OG that uses pulsed light to activate bioluminescence and drive only the activated nearby optogenetic molecules and channels. This method provides an alternative to conventional holography with several benefits (Carillo-Reid 2019, Marshel et al., 2019). This PS BL-OG construct, AAV-hSyn-VChR-link-OfoEK, provides an additional and complementary tool to holographic optogenetic modulation through its chemogenetic control, optical report of activation, and ability to reach deeper neural targets.

Photoswitching chemogenetics provides a temporal report of the photoswitch-effect that allows a unique opportunity for visual monitoring of the time course of activation. This activation of the molecule is coincident with an optical report of the substrate reaching its target. Additionally, PS BL-OG affords more permissive time control of specific cell selection of genetically identified cells and can reach deeper targets than conventional holographic stimulation (Figure 6). While conventional optogenetic stimulation is difficult in deeper regions of the brain, PS BL-OG enables deeper neural control through its ability to prime channels to be turned on with pulsed light. This supports behavioral modulation on longer time scales during whole behavioral training sessions *in vivo* and across days of training.

Introduction

BioLuminescent (BL) light production can modulate neural activity and behavior through co-expressed OptoGenetic (OG) elements, an approach termed "BL-OG." Yet, the

relationship between BL-OG effects and bioluminescent photon emission has not been characterized *in vivo*. Further, the degree to which BL-OG effects strictly depend on optogenetic mechanisms driven by bioluminescent photons is unknown. Crucial to every neuromodulation method is whether the activator shows a dynamic concentration range driving robust, selective, and nontoxic effects. We systematically tested the effects of four key components of the BL-OG mechanism (luciferin, oxidized luciferin, luciferin vehicle, and bioluminescence), and compared these against effects induced by the Luminopsin-3 (LMO3) BL-OG molecule, a fusion of slow burn Gaussia luciferase (sbGLuc) and Volvox ChannelRhodopsin-1 (VChR1). We performed combined bioluminescence imaging and electrophysiological recordings while injecting specific doses of Coelenterazine (substrate for sbGluc), Coelenteramide (CTM, the oxidized product of CTZ), or CTZ vehicle. CTZ robustly drove activity in mice expressing LMO3, with photon production proportional to firing rate. In contrast, low and moderate doses of CTZ, CTM, or CTZ vehicle did not modulate activity in mice that did not express LMO3. We also failed to find bioluminescence effects on neural activity in mice expressing an optogenetically nonsensitive LMO3 variant. We observed weak responses to the highest dose of CTZ in control mice, but these effects were significantly smaller than those observed in the LMO3 group. These results show that in Neocortex *in vivo*, there is a large CTZ range wherein BL-OG effects are specific to its active chemogenetic mechanisms.

Novel genetic- and optical-based methods that target specific cell types provide a powerful strategy for probing neural mechanisms that underlie perception and action (Berglund, Tung, et al., 2016; Boyden, Zhang, Bamberg, Nagel, & Deisseroth, 2005;

Cardin et al., 2009; Fenno, Yizhar, & Deisseroth, 2011; Kim, Adhikari, & Deisseroth, 2017; Knopfel et al., 2010; Nichols & Roth, 2009; Roth, 2016; Tung, Gutekunst, & Gross, 2015; Zhang, Wang, Boyden, & Deisseroth, 2006; Zhu, Feng, Schwartz, Gebhart, & Prescott, 2015). Of such approaches, optogenetic and chemogenetic strategies are the most widely employed. The former provides high spatio-temporal precision, while the latter provides broad coverage and minimally invasive delivery of the activating driver.

BioLuminescent OptoGenetics ("BL-OG") is an emerging dual strategy that provides both optogenetic and chemogenetic capabilities. In this approach, binding of an oxidative enzyme (luciferase) to a small light-emitting molecule (luciferin) drives bioluminescence that, in turn, regulates a neighboring opsin (Berglund, Birkner, Augustine, & Hochgeschwender, 2013; Berglund, Clissold, et al., 2016; Berglund, Fernandez, Gutekunst, Hochgeschwender, & Gross, 2019; Berglund, Tung, et al., 2016; Birkner, Berglund, Klein, Augustine, & Hochgeschwender, 2014; Park et al., 2017; Prakash, Medendorp, & Hochgeschwender, 2018; Tung et al., 2015; Tung, Shiu, Ding, & Gross, 2018; Zenchak et al., 2018). To ensure proximity of the bioluminescent reaction to the recipient opsin, the *luminopsin* (LMO) construct was invented, in which a luciferase is linked to the optogenetic element by a short 15 amino acids linker (Berglund, Tung, et al., 2016). Here, we use LMO3, a molecule that tethers the slow-burn Gaussia luciferase (sbGLuc) to Volvox Channelrhodopsin-1 (VChR1; Figure 1a), and uses the substrate coelenterazine (CTZ) to generate bioluminescence. This single molecule permits both chemogenetic regulation by peripheral injection of a luciferin (Berglund et al., 2013; Berglund, Tung, et al., 2016; Birkner et al., 2014; Tung

et al., 2015), and local optogenetic regulation by external light application or direct intracortical injection of the luciferin (Tung et al., 2015). The BL-OG strategy has several additional distinctive benefits, including the robust biocompatibility of its components, and photon production that confirms the activator reached its target (e.g., by imaging while administering the drug). Further, while existing BL-OG implementations have employed luciferases that bind the luciferin Coelenterazine (CTZ), multiple distinct and noninteracting classes of luciferin are potentially viable (Haddock, Moline, & Case, 2010), providing multiple independent pathways for distinct forms of simultaneous modulation.
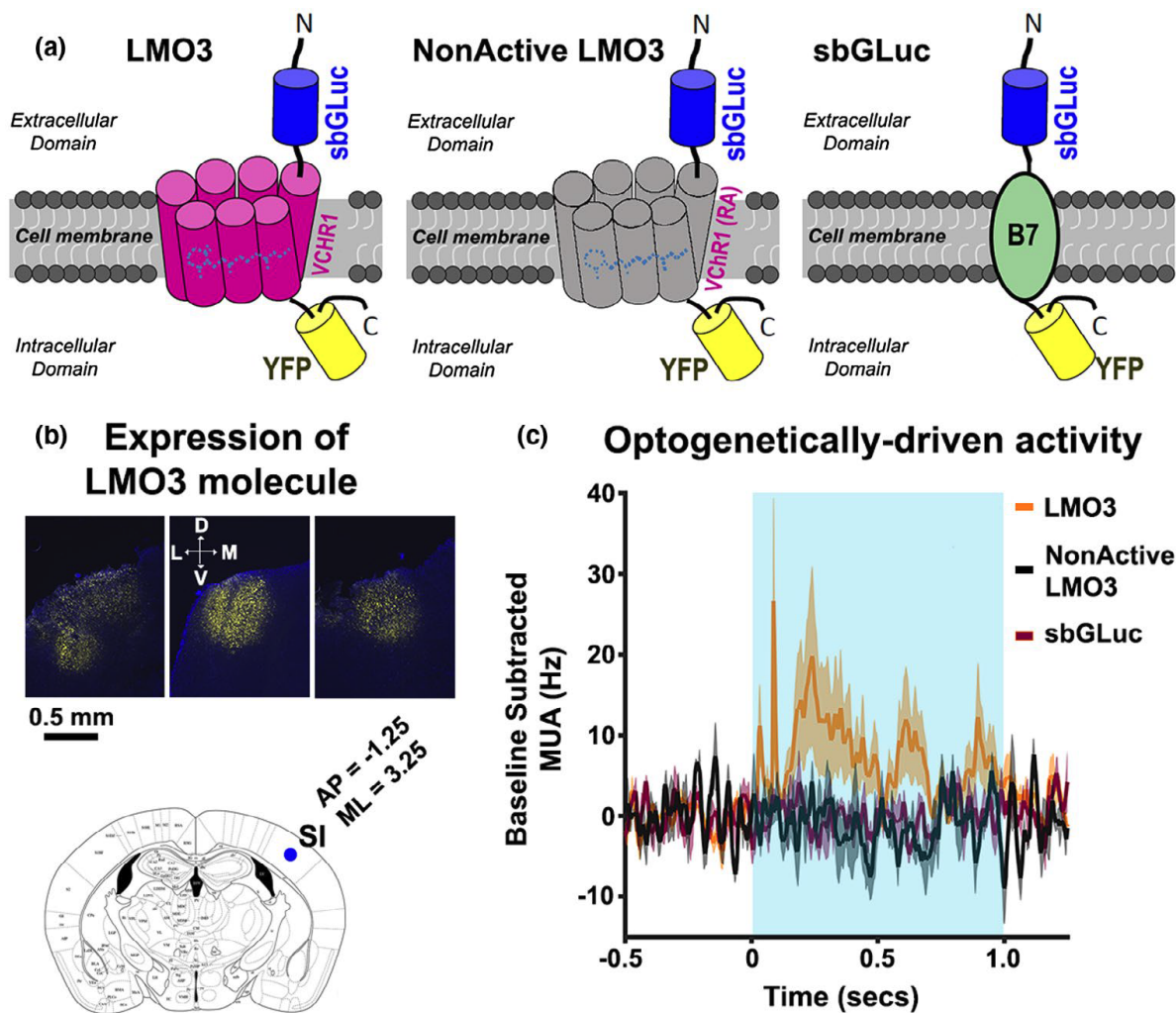
Figure 1: (a) Schematic illustration of the genetically engineered molecules: LMO3 (left), NonActive LMO3 (center), and sbGLuc (right). In the LMO3 molecule, the luciferase slow-burn Gaussia (sb-GLuc) is tethered to the opsin Volvox Channelrhodopsin1 (VChR1) and the enhanced yellow fluorescent protein (eYFP). The NonActive LMO3 is structurally the same as the LMO3 molecule, except that the VChR1 has an arginine–alanine point mutation that renders the opsin nonfunctional, indicated by the gray color of the VChR1. The sbGLuc is linked to the membrane using the B7 transmembrane protein with the luciferase located outside the cell. (b) Representative histological images showing eYFP expression in the left SI of three animals (upper panels). The lower panel shows a brain slice of a mouse atlas at location A/p = −1.25, M/L = 3.25 relative to Bregma. The blue circle indicates the depth of the injection site (~500 μm). We injected in three locations relative to the blue circle: Location 1 (A/p = −0.75 M/L = 2.75), Location 2 (A/p = 0.5, M/L = 0), and Location 3 (A/p = −1.75 M/L = 2.75). All injections were made the same depth (500 μm) (mouse brain atlas was adapted from http://labs.gaidi.ca/mouse-brain-atlas/). (c) Spiking activity in the LMO3 (orange trace), NonActive LMO3 (black trace), and sbGLuc (violet trace) groups in response to LED stimulation. The data show increases in spiking activity for the LMO3 group only, indicating that only this cohort expressed a functional optogenetic element.

Activators (e.g., chemicals or light) used in all neuromodulation methods have a regime of nonspecificity. The most widely employed chemogenetic method, Designer Receptors Exclusively Activated by Designer Drugs (DREADDs), is driven by clozapine n-oxide (CNO) (Urban & Roth, 2015). MacLaren and colleagues (2016) showed that CNO has adverse behavioral effects in naïve rats, possibly because CNO is converted into Clozapine (an antipsychotic) through endogenous body mechanisms (Gomez et al., 2017). Light stimulation can also impact local cellular processes by a variety of intrinsic mechanisms, including photovoltaic/photoelectric effects (Kozai & Vazquez, 2015). A crucial challenge for neuromodulation methods is to determine a dose (or intensity) range of the activator that evokes a proportional modulation, so that a desired effect is consistently achieved throughout repeated trials.

Here, we systematically tested the relationship between BL-OG neural modulation and photon production, and the possibility that nonspecific components of its bioluminescent reaction modulate neuronal spiking. To this end, we expressed LMO3 in mice, a BL-OG construct previously demonstrated to robustly activate neurons (Berglund, Clissold, et al., 2016; Berglund, Tung, et al., 2016; Prakash et al., 2018), and drive behavioral responses when activated by CTZ (Berglund, Tung, et al., 2016; Zenchak et al., 2018). We tested whether the neural response in LMO3-expressing mice was proportional to CTZ dose and photon production. The BL-OG mechanism requires catalysis of CTZ, which generates its oxidized derivative, Coelenteramide (CTM). As such, we also tested the effects of CTZ, CTM, or vehicle control (the compound that renders water-soluble CTZ) on neural spiking in naïve mice. We also assayed the effects of bioluminescence itself on neural activity by injecting CTZ in mice expressing sbGLuc without a functional opsin or the sbGLuc alone. BL-OG effects in mice expressing LMO3 were highly sensitive, showing proportional increases in neural firing and photon production in response to increasing doses of CTZ. Systematic responses were not observed in any control condition. We only observed weak, but significant, responses to the highest CTZ dose in naïve mice and mice not expressing a functional opsin. These results show a selective and robust regime for driving neocortical activation with the BL-OG method.

METHODS

Animals

Thirty-six mice (16 females, 20 males, C57BL/6NHsd from Jackson Labs, 10–26 weeks) were utilized in the experiments. Mice were housed in a vivarium with reverse light–dark

cycle (12 hr each phase) and given *ad libidum* access to water and food. All procedures were conducted in accordance with the guidelines of the National Institute of Health and with approval of the Animal Care and Use Committee of Brown University.

BL-OG construct and viral injections

Figure 1a shows schematics of each genetically engineered molecule used in this paper, and Table 1 describes the different molecules and chemical agents injected in each cohort. The LMO3 molecule (sbGLuc-VChR1-EYFP) (Berglund, Clissold, et al., 2016) consists of human codon optimized Gaussia luciferase carrying two methionine-to-leucine mutations (M43L/M110L; sbGLuc) (Welsh, Patel, Manthiram, & Swartz, 2009) fused to the extracellular N-terminus of Volvox Channelrhodopsin 1 (VChR1-EYFP) (Zhang et al., 2008). For the NonActive LMO3 (R115A) construct, a nonfunctional arginine-to-alanine point mutation described for ChR2 (R120A) (Kato et al., 2012) was introduced into the VChR1 sequence. All molecules were packaged in an AAV2/9 vector with the human synapsin 1 promoter. For the GLuc-only construct, the sequence coding for VChR1 was replaced by the sequence for the B7 transmembrane region from the mouse CD80 antigen (Chou et al., 1999), generating sbGLuc-B7-EYFP. The luciferase is tethered to the cell membrane extracellularly without the optogenetic element.

Table 1. Description of the molecule each cohort expressed and the chemical agents injected

Cohort	Chemical injected	Molecule expression

LMO3	CTZ	LMO3
CTM	CTM	None
Vehicle	Vehicle	None
GLuc	CTZ	NonActive LMO3 sbGLuc-B7
CTZ	CTZ	None

We injected 450 nl of the virus across three locations in left primary somatosensory (SI) Neocortex (150 nl per site). Injections were made through a burr hole placed 500 μm M/L and 500 μm A/P relative to Bregma in SI (−1.25 A/P and 3.25 M/L relative to Bregma). Specifically, injection 1 was made at A/p = −1.25 M/L = 3.75, injection 2 was made at A/p = −0.75 M/L = 2.75, and injection 3 was made A/p = −1.75 M/L = 2.75. Figure 1b shows examples of viral expression data, and an atlas illustration of the injections. The virus was drawn into a glass micropipette attached to a Quintessential Stereotaxic Injector (QSI, Stoelting) that was lowered 500 μm below the cortical surface. Viral constructs were infused at a rate of 7.5 nl/min, and pipettes were held in place for 5 min following infusions before retracting from the brain. The scalp incision was manually sutured or glued using Gluture (Abbott Laboratories). Dexamethasone was given intraperitoneally (0.1 mg/kg) to reduce brain inflammation, and Slow Release Buprenex was given subcutaneously to aid postsurgery comfort (0.1 mg/kg). The median time between viral transduction surgery and experiments was 28 days (min = 26

days, max time = 74 days). There was no systematic relationship between expression time and bioluminescence ($p > .05$; $r = .007$) or MUA ($p > .05$; $r = .021$).

Luciferin injections

Water-soluble CTZ (Nanolight Technology, Catalog #3031 Coelenterazine-SOL *in vivo)* was diluted in sterile water (1 mg/ml) to yield a concentration of 2.36 mM. CTZ injections were done directly in Neocortex. In a preliminary subset of LMO3-expressing mice, we also assayed BL-OG effects by injecting CTZ via intraperitoneal, intravenous, and intraventricular routes (data not shown). Water-soluble CTM was purchased from Nanolight Technology, and diluted in sterile water (1 mg/ml) to yield a concentration of 2.43 mM. The vehicle was also purchased from Nanolight Technology, and diluted in sterile water (1 mg/ml). Local cortical injections of CTZ, CTM, and vehicle spanned 0.2, 0.4, and 1 µl, respectively, at an injection rate of 1.25 µl/min. All cortical injections were delivered using a Hamilton Nanosyringe with a 34-gauge needle that was attached to a motorized injector (Stoelting Quintessential Stereotaxic Injector, QSI).

Imaging and electrophysiology recordings

Bioluminescence was measured using an electron multiplier charge-coupled device (EMCCD) camera (Ixon 888, Andor) attached to a Navitar Zoom 6000 lens system (Navitar, 0.5× lens). The camera's sensor was 1,024 × 1,024 pixels, with a 13.4 µm × 13.4 µm pixel size. Images were collected in a custom-made light-tight chamber with an exposure time of 10 s, and the EM gain set to 30. Imaging data were recorded using the Solis image acquisition and analysis software (Solis 4.29, Andor). A TTL pulse was

used to synchronize the onset of imaging and electrophysiological data in each experimental block.

Neurophysiological activity was recorded using a 32-channel laminar electrode (Optoelectrode, A1x32-Poly2-5mm-50s-177-OA32LP, Neuronexus). The laminar electrode was composed of two columns of 16 channels with each contact spaced 50 μm apart. The electrode had an optical fiber (105 μm diameter) attached to the recording side of the electrode shank that terminated 200 μm above the most superficial electrode. The electrode was lowered 900 μm past the cortical surface. Neural activity was acquired using the open source OpenEphys system (http://www.open-ephys.org/). Neural data were recorded with a sampling rate of 20 KHz, and referenced to a supra-dural electrode chronically implanted over right occipital Neocortex.

Optogenetic stimulation

Optogenetic stimulation was achieved by delivering 40-Hz light pulses of 470-nm wavelength. Each pulse intensity was 0.5 mW/cm2, 0.07 s in length, and with the probability drawn from a Poisson distribution (rate = 40 Hz). The entire 40-Hz pulse train lasted 1 s. Light was controlled using a Mightex LED driver (SLA-1200-2) that delivered power to a Thorlabs fiber-coupled LED. A patch cable from the fiber-coupled LED was attached to a bare ferrule-coupled connector in the optoelectrode.

Sequence of events

Experiments were performed under isoflurane delivered at ~1% (range 0.75%–2%). Approximately 1 hr prior to recording, a craniotomy that covered virally transduced sites

was performed, and animals were transferred from the surgical suite to the experimental chamber. The order of CTZ cortical injection doses was randomized across animals. Each session began with 10 s of baseline recordings. Sensory vibrissal stimuli were applied before and after CTZ injection (3–5-s interstimulus interval; ISI). Note however, that analyses were conducted on activity during the prestimulus because our goal was to assay BL-OG effects uncontaminated by sensory-driven activity. Data associated with tactile stimulation are not reported as receptive fields were inconsistent or absent in a subset of recordings.

In a subset of animals expressing LMO3 (N = 7), we performed optogenetic studies to assay whether opsins were driven using standard optical methods. We performed similar experiments in animals expressing the sbGLuc-only and the NonActive-LMO3 molecule. Figure 1c shows mean activity in response to LED activity in the 470-nm range for animals expressing LMO3 (orange trace), sbGLuc-only (violet trace), and NonActive LMO3 (black trace). The data show activation in LMO3 mice only, indicating that the VChR1 opsin was functional in this cohort.

Histology

After each experiment, mice were euthanized with isoflurane and perfused transcardially with 4% paraformaldehyde (PFA). The brain was removed and kept in PFA at 4°C for 36 hr after perfusion. The brain was cryoprotected in 30% sucrose for another 36 hr prior to tissue slicing. Mice brains were sectioned in 50-µm slices on a cryostat (Leica CM30505), and mounted on glass slides for imaging on an inverted fluorescent microscope (Zeiss Axiovert 200M; 10× EC Plan-NeoFluar objective).

Regions of viral expression were then compared to a brain atlas (Allen Mouse Brain

Atlas) to confirm the correct location of the SI viral expression (see Figure 1b).

Analyses

Images were converted to 16-bit tiff files and analyzed using custom-based scripts in

MATLAB. Pixel values higher than three standard deviations from the mean present for

only a single frame were deleted, and images were smoothed using a 2 × 2 pixel filter.

For each pixel, bioluminescence was expressed as a relative measure by subtracting

the averaged activity between the initial frame and the frame prior to CTZ injection from

all recorded frames. Statistical significance of bioluminescent activity was assayed

using nonparametric bootstrapping statistics. For each pixel, we computed the mean of

25 randomly extracted frames prior to the CTZ injection, and built a surrogate

distribution by repeating this procedure 5,000 times. Bioluminescent activity of each

pixel after CTZ injection was compared against the surrogate distribution. Significant

activity was defined as data values greater than 95% of the surrogate values for at least

three consecutive frames.

Electrophysiological data were analyzed using custom scripts in MATLAB. Data were

downsampled ($n = 2$) and notch filtered at 60 Hz to reduce ambient noise. Proxies of

multiunit activity (MUA) were derived by filtering the raw data with a high-pass filter (500

and 2,500 Hz), and rectifying the filtered data. Outliers were removed by deleting data

points that were nine standard deviations greater than the average power value. A value

of one (i.e., a spike) was assigned to data points that were four standard deviations

greater than the mean. All other points were assigned a zero value. We convolved MUA

activity with an asymmetric Gaussian filter (30-ms duration, with a rising slope = 19.91

mV/s) to derive instantaneous MUA (Gomez-Ramirez, Trzcinski, Mihalas, Niebur, &

Hsiao, 2014). Individual observations used in the statistics comprised averaged activity

between −1,500 and −500 ms prior to the onset of the tactile stimulus. Statistical effects

were assayed using nonparametric bootstrapping statistics, with a significant activity

defined as values greater than 95% of the surrogate values. The data that support the

findings of this study are available from the corresponding author upon reasonable

request.

RESULTS

**Bioluminescent photon generation is proportional to neural firing in
LMO3-expressing mice**

We performed simultaneous electrophysiology and high-sensitivity imaging in primary

somatosensory Neocortex (SI) in mice transduced with LMO3 (N = 10). Figure 2a

shows an example of enhanced bioluminescence following CTZ injection. Figure 2b

shows the bioluminescence and MUA time courses for the ROI depicted in Figure 2a

(*dashed box*) near the electrode (*white circle*) and injection cannula (*red circle*).
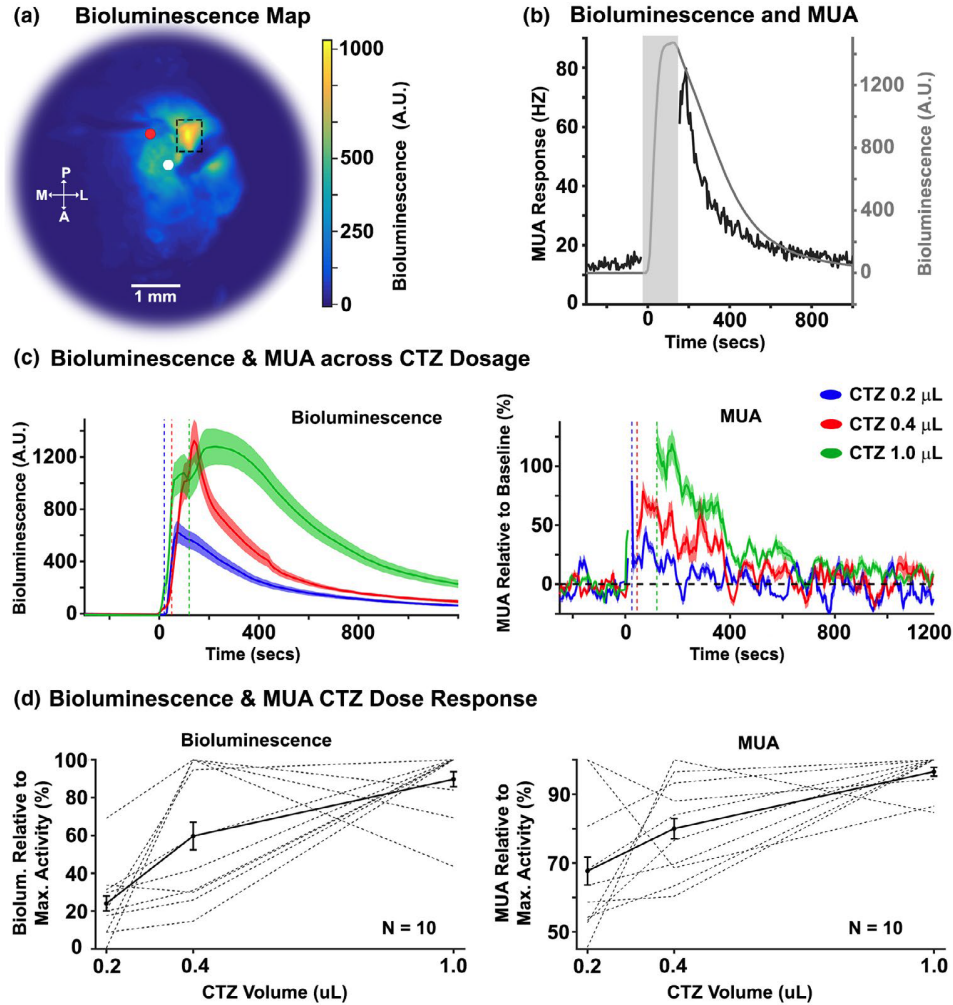
(a) Bioluminescence Map

(b) Bioluminescence and MUA

(c) Bioluminescence & MUA across CTZ Dosage

Bioluminescence

MUA

CTZ 0.2 μL
CTZ 0.4 μL
CTZ 1.0 μL

(d) Bioluminescence & MUA CTZ Dose Response

Bioluminescence

MUA

N = 10

N = 10

Figure 2: BL-OG effects as a function of CTZ dose. (a) Representative example of a normalized bioluminescence color map in response to a 1.0-μl injection of CTZ directly in Neocortex. A = anterior, P = posterior, M = medial, L = lateral. The white and red circles indicate the surface locations of the electrode and injector, respectively. The electrode and syringe were inserted at angles between ~20º and 45º, and to different depths relative to dura (electrode ~900 μm, and syringe ~500 μm). (b) Bioluminescence (gray trace) and MUA (black trace) time courses within the ROI in Figure 2a (dashed box). The gray rectangle indicates the time of CTZ onset/offset for the 1.0-μl CTZ dose condition with a ±30 s window added. The discontinuity in the MUA response stemmed from a mechanical and electrical artifact created by the QSI injector. (c) Left and right panels show normalized bioluminescence and MUA as a function of CTZ dose for direct cortical injection conditions, respectively (*N* = 10). The dotted vertical lines indicate the offset of the injection for each CTZ dose condition. (d) Left and right panels show normalized bioluminescence and MUA for each animal, relative to the CTZ dose that evoked the max response, respectively (*N* = 10)

To systematically compare the sensitivity and proportionality of the optical and

neurophysiological response, we injected three CTZ doses (0.2, 0.4, and 1.0 μl) (Figure

2c). All dose levels of CTZ significantly increased bioluminescence relative to baseline at the mouse group level ($p < .0001$, mean 0.2 µl = 419.75, mean 0.4 µl = 715.15, mean 1.0 µl = 1,233.14), as well as in each mouse ($p < .0001$), with the exception of two mice at the lowest dose ($p = .15$ and $p = .101$). The CTZ injection also increased MUA at the group level. Specifically, we found significant increases in MUA for the 0.4 µl (mean = 41.39%; $p = .039$), and 1.0 µl (mean = 71.22%; $p = .01$) CTZ doses. We observed a trend toward significance for the 0.2-µl condition (mean = 22.48%; $p = .09$). At the individual mouse level, we observed significant

Figure 3: MUA as a function of bioluminescence. The relationship is shown between averaged bioluminescence and MUA for each CTZ dose condition in the LMO3 (circle symbol) and GLuc (diamond symbol) cohorts for the time period (0–400 s after injection of CTZ). The larger symbols indicate the mean activity for each CTZ dose condition.

We failed to see significant modulations in MUA at the mouse group level during later time periods (400–800 s) for any CTZ dose condition (0.2 µl = 0.04%, $p > .05$; 0.4 µl = 7.90%, $p > .05$; 1.0 µl = 22.82%, $p > .05$). However, at the individual mouse level, we observed significant MUA increases in two mice for 0.2 µl ($p < .05$), two mice for 0.4 µl CTZ ($p < .05$), and four mice for 1.0 µl CTZ ($p < .05$). Importantly, we observed significant increases in bioluminescence during the latter periods (400–800 s) for all CTZ doses (0.2 µl = 154.78, $p < .0001$; 0.4 µl = 232.24, $p < .0001$;


30
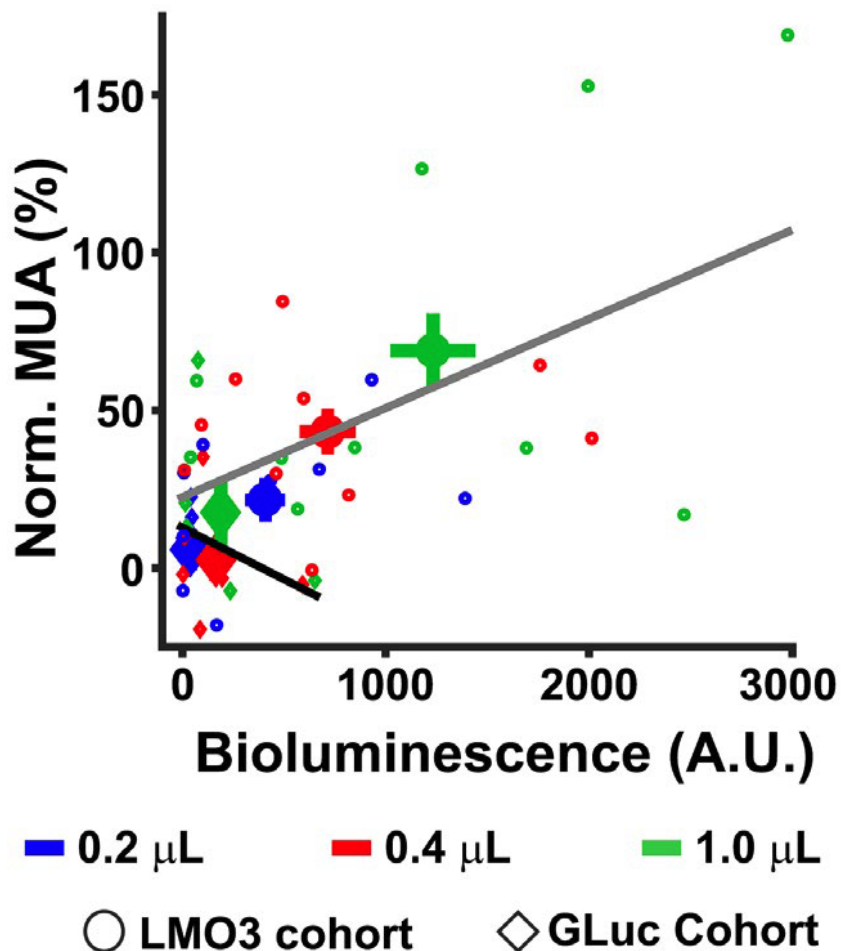
1.0 µl = 671.99, $p < .0001$) at the group level. At the individual mouse level, we observed significant bioluminescence in 9 mice for 0.2 µl CTZ ($p < .05$), 9 mice for 0.4 µl CTZ ($p < .05$), and 10 mice for 1.0 µl CTZ ($p < .05$). This discrepancy between bioluminescence and MUA effects could either reflect weak bioluminescent light that is unable to drive detectable neural activity, adaptation of the neural response, and/or adaptation of optogenetic sensitivity to sustained bioluminescent production.

modulations in MUA in six mice for 0.2-µl CTZ ($p < .05$), eight mice for 0.4-µl CTZ ($p < .05$), and nine mice for 1.0-µl CTZ ($p < .05$). The left and right panels of Figure 2d show bioluminescence (left panel) and MUA (right panel) responses normalized to the highest CTZ response of each animal, respectively. Linear regression analyses revealed a systematic relationship between bioluminescence and MUA ($p < .001$, $R_2 = .36$; see Figure 3; gray regression line).

Elements of the BL-OG reaction create minimal off target effects *in vivo*

We assayed whether CTZ, CTM, or vehicle drive spiking activity through non-BL-OG-related mechanisms, by injecting these chemicals directly in SI of non-expressing mice (Figure 4a *upper three panels*). For the CTZ cohort ($N = 8$), we did not observe significant changes in MUA to the 0.2 µl (2.89%, $p > .05$) or 0.4 µl CTZ doses (2.26% $p > .05$). However, we found modest, but significant, MUA increases when injecting the largest dose of CTZ (1.0 µl = 12.79%, $p = .045$). For the CTM cohort ($N = 8$), no significant modulations for any dose conditions were observed (0.2 µl = −2.89%, $p > .05$; 0.4 µl = 0.63%, $p > .05$; 1.0 µl = 5.71%, $p = .09$). We also failed to find significant MUA changes in the vehicle cohort for any dose (0.2 µl = 0.4%, $p > .05$; 0.4 µl = 2.59%, $p > .05$; 1.0 µl = 2.77%, $p > .05$). As expected, we also failed to observe bioluminescent responses to any dose condition for the CTZ, CTM, and vehicle cohorts ($p > .05$).

(a) MUA effects: Control groups

CTZ Cohort

CTM Cohort

CTZ-Vehicle Cohort

GLuc Cohort

■ 0.2 μL   ■ 0.4 μL   ■ 1.0 μL
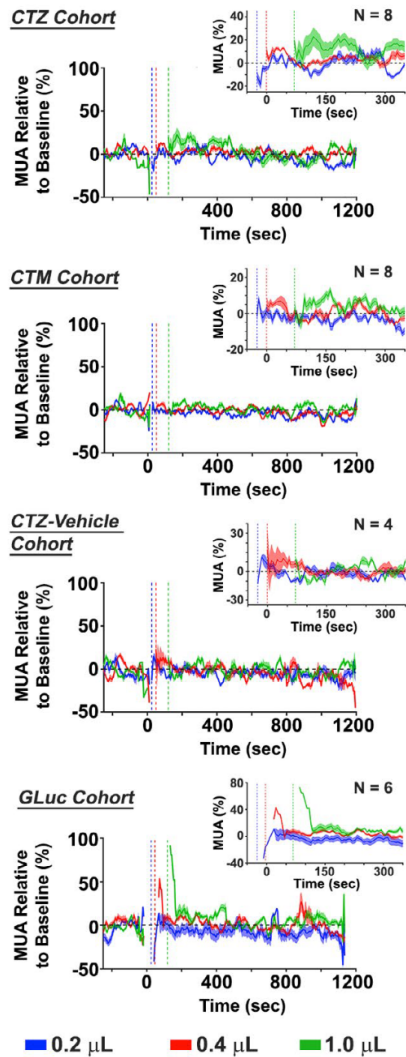
(b) Bioluminescence GLuc cohort
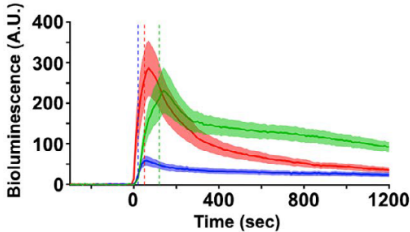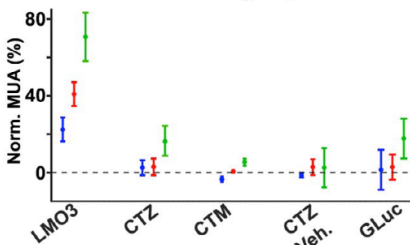
(c) Mean MUA across groups and dose

Figure 4: MUA and bioluminescence in control groups. (a) BL-OG effects on MUA are shown for the control groups. The top graph shows MUA effects in the CTZ naïve group. The data revealed significant increases in the 1.0-μl condition. The second and third row graphs show MUA data in the CTM and vehicle naïve groups, respectively. The data did not reveal MUA changes for any dose condition in either group. The bottom row shows MUA changes for the GLuc cohort. Similar to the CTZ naïve group, we observed modest increases in MUA for the largest CTZ dose. The inset in all graphs shows an enlarged view of activity between −50 and 350 s after chemical injection. (b) The bioluminescent response across CTZ doses for the GLuc cohort is shown. Systematic increases in bioluminescence were observed with increases in CTZ dose. (c) MUA activity across all cohorts and chemical doses. The strongest MUA modulations were observed in the LMO3 group, with small changes for the largest CTZ dose for the CTZ naïve and GLuc groups

To test for effects of bioluminescence on spiking activity, we injected a molecule that expressed sbGLuc or an LMO3 molecule with a mutation in the opsin that rendered the VChR1 nonfunctional in different animals. MUA responses in these conditions were similar, and not statistically different from each other (sbGLuc: 0.2 μl = 6.73%, 0.4 μl = −0.24%, 1.0 μl = 17.85%; NonActiveLMO3: 0.2 μl = −3.74%, 0.4 μl = 5.97%, 1.0 μl = 17.62%); thus, we combined the two datasets, a cohort we termed "GLuc" (Figure 4a *lower panels*, and Figure 4b). Injections of CTZ yielded no MUA changes in the 0.2 μl (1.49%, *p* > .05) or 0.4 μl CTZ dose (2.87%, *p* > .05). However, similar to the CTZ cohort, we found modest significant increases in the 1.0-μl CTZ condition (17.74%, *p* < .01). We observed proportional

modulations in bioluminescence in response to CTZ (0.2 µl = 38.52 $p < .05$; 0.4 µl = 165.48 $p < .05$; 1.0 µl = 188.58 $p < .05$) (see Figure 4b), but, importantly, failed to see a relationship between MUA and bioluminescent photon production ($R_2 = 0.09$; $p > .05$, see Figure 3, black regression line).

We compared MUA effects between the CTZ and GLuc cohorts to assay whether the slight increase in MUA for the GLuc versus CTZ cohort (17.74% vs. 16.28%) was due to the bioluminescent reaction or just unaccounted noise. The data revealed no significant differences between the two groups ($p = .61$), indicating that MUA modulations in the GLuc group are likely driven by the CTZ chemical itself. A summary of the mean MUA effects for each chemical dose condition and cohort tested is shown in Figure 4c.

Temporal properties of the BL-OG effect

We investigated the duration of the BL-OG effect by determining the continuity of significant MUA increases for all CTZ doses in the LMO3 group. We classified a statistically significant time point when two consecutive time points had an increase in MUA greater than 95% of points as compared to a surrogate distribution built from the CTZ preinjection data (Figure 5). The data revealed continuous BL-OG effects for the largest CTZ dose that commenced at the earliest time point analyzed after CTZ onset, and lasted for ~160 s (see inset Figure 5 green trace). Similarly, continuous BL-OG effects in the 0.4 µl started right after CTZ injection, but only lasted ~40 s (red trace in Figure 5 inset). However, there was a long period (~120 s) where MUA BL-OG effects in the 0.4-µl condition trended toward significance ($p < .1$). Continuous BL-OG effects in

the 0.2-μl CTZ condition were not observed for any time point (blue trace in Figure 5 inset).
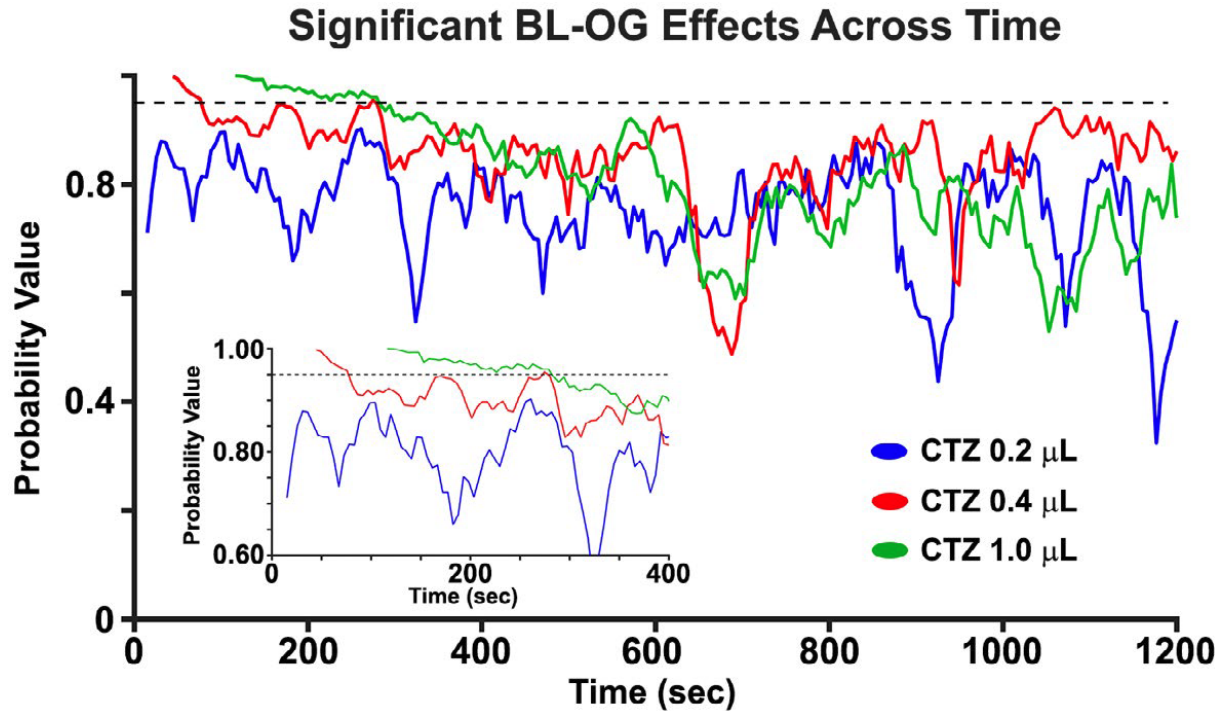
Figure 5: BL-OG effects as a function of time. BL-OG effects on MUA across time for all CTZ doses in the LMO3 group. The inset shows a zoomed in view of the probability values in the first ~400 s. Note that the first 24, 48, and 120 s are not plotted because of the injection artifact for the 0.2, 0.4, and 1.0 μl, respectively.

DISCUSSION

We investigated the relationship between bioluminescence and optogenetic excitation of neural activity in anesthetized mice expressing LMO3, and found a systematic relationship between bioluminescence and MUA in animals expressing the LMO3 construct. We also tested the effects of four major elements of the BL-OG reaction on spiking activity (CTZ, CTM, vehicle, and bioluminescence). We failed to observe a dose

range where CTM or vehicle modulated MUA. The largest CTZ dose modestly increased neural activity in naïve mice and GLuc cohorts, with no differences in MUA effects between the two groups. These findings suggest that CTZ itself can have nonspecific excitatory effects in high concentrations, with selective effects across a large dose range. Taken together, these data indicate that BL-OG is a viable method for regulating activity of genetically identified neurons *in vivo*. We recommend using a CTZ dose that evokes selective effects, and, when appropriate, testing for possible off target effects when applying this method in new regions and cell types.

Relationship between bioluminescence and MUA

A major focus of our study was to characterize the relationship between bioluminescence and changes in neural activity relative to CTZ dose. We observed a systematic relationship between bioluminescent activity and MUA (Figures 2b and 3), indicating that the LMO3 molecule robustly drives optogenetic elements *in vivo*. The data also revealed a systematic relationship between bioluminescence and MUA as a function of CTZ dose, with larger infusions of CTZ leading to greater MUA and bioluminescence. The dynamic range of this effect spanned ~75%, demonstrating that BL-OG effects can be parametrically varied within a large range depending on the CTZ dose used.

Maximal effects of BL-OG were observed during the early phase of CTZ administration (0–400 s), and BL-OG effects gradually decreased across time. While reliable bioluminescent signals were observed during 400–800 s for all CTZ doses, we failed to find MUA modulations in any CTZ condition at the group level. However, we did observe

significant MUA increases in a small subset of animals. Also, for the largest CTZ condition we observed continuous BL-OG effects commencing at the beginning of the CTZ injection and lasting for ~160 s. We found similar, but weaker and shorter, effects for the 0.4 µl CTZ dose, whereas no effects in the 0.2 µL CTZ dose, suggesting that BL-OG effects for these doses require a larger integration time to elicit long-lasting statistically significant modulations.

Targeted concentration range of CTZ

A major goal of this paper was to assay potential off target effects of four major elements of the BL-OG strategy. Previous chemogenetic studies have shown that driving agents can cause neural artifacts (MacLaren et al., 2016), and light activation can modulate neural activity (Kozai & Vazquez, 2015). We found that neither CTM, the oxidized product of CTZ, nor vehicle modulated neural spiking activity. Similar findings were observed for the lower CTZ doses in both CTZ and GLuc cohorts. Yet, we observed modest increases in MUA in response to the largest CTZ dose.

A key question for all neuromodulation methods is to determine the threshold level at which nonspecific effects emerge. In the case of chemogenetic drivers, the threshold implies a dose at which the activating molecule yields robust responses while producing negligible off target effects. While the specific approach used here (direct neocortical injection) may not be the preferred administration strategy for some BL-OG applications (e.g., in free behavior studies), these results nevertheless indicate a substantial range of CTZ levels across which neocortical nonspecific effects are not a significant concern.

Advantage of using luciferases to monitor and control neural ensembles

The use of luciferases for studying and manipulating brain circuits has several distinctive advantages over other chemogenetic methods: (a) In our BL-OG strategy, a single molecular construct provides both optogenetic and chemogenetic activation options. As such, LMOs can facilitate integrated experiments, whereby a distributed system of neurons can be activated by systemic injection of a chemical, or distinct subregions can be controlled by local injections or delivery of light through a fiber optic in the same animal. (b) Unlike most chemogenetic options, the rapidly expanding family of optogenetic options in combination with the broad range of existing luciferases and luciferins (Haddock et al., 2010), provide an expanded toolkit to meet specific experimental needs. These options include direct ion channel opening (e.g., using Channelrhodopsin variants) or other light-dependent applications (e.g., engagement of G-protein pathways, as accessed by DREADDs). (c) Because distinct luciferins are typically not cross-reactive with non-matched luciferases (Haddock et al., 2010), multiple independent BL-OG targets could be independently activated in the same preparation by the choice of luciferins. (d) BL-OG has the unique feature of reporting the successful delivery of a pharmacological agent (a luciferin) by emitting light. Even simple optical detection techniques can provide real-time insight into the efficacy and time course of chemical delivered to the preparation (e.g., by peripheral injection). (e) Other uses of bioluminescence to study brain functions have been developed (Inagaki & Nagai, 2016; Inagaki et al., 2017; Naumann, Kampff, Prober, Schier, & Engert, 2010), providing an even wider range of distinct applications. For instance, bioluminescent molecules have been used as reporters of cell activity in the calcium (Gomez-Ramirez

37

et al., 2017; Naumann et al., 2010; Saito et al., 2012) and voltage domain (Inagaki et al., 2017), and can be tethered to opsins to enable cellular-specific and real-time neural regulation (Pal et al., 2017).

Fiber optic drive of light-sensing molecules can achieve millisecond precision of neural modulation. However, chemogenetic strategies may be more advantageous when sustained modulation of defined populations, especially over widespread regions, is desired. Like most chemogenetic options, BL-OG obviates the need for invasive devices (e.g., implanted fiber optics). Invasive external devices delivering light (e.g., optical fibers) are challenging for many reasons, in part because implants represent a path for pathogens to reach the brain, a concern that is amplified in long-term chronic experiments lasting months or years. In addition, light from optical devices can be limited in its utility for continuously exciting (or inhibiting) a population for extended periods of time because power from photon emission can overheat tissue and lead to photodamage and/or photobleaching (Chirico, Cannone, Baldini, & Diaspro, 2003; Denk & Svoboda, 1997; Pashaie & Falk, 2013). Also, optical implants can be punitive when targeting disparate foci because insertion of several fibers can cause considerable tissue damage that lead to behavioral deficits. Chemogenetic solutions to this latter drawback are particularly encouraging because the ability to concomitantly modulate large scale, but functionally connected, cell ensembles is fundamental for interrogating neural codes underlying complex behavior of mammalian networks.

Further BL-OG development through the creation and testing of photoswitchable tools

In this Chapter, I described the creation of Bioluminescent-Optogenetic tools for the regulation of neural activity in Neocortex. However, this molecular control tool stimulates genetically-defined cells *en masse*. In Chapter 3 and 4, I describe subtypes of a genetically-defined population that differ in their activity during task performance. Crucial to the manipulation of these distinct ensembles is the ability to target cells based on their activity and not just their genetic definition.

To address this need, we are developing a photoswitchable version of BL-OG (PS BL-OG) that can be stimulated with two-photon light. This construct is composed of a bioluminescent molecule (Ofo) tethered to a fluorescent molecule (EK) tethered to an opsin (VChR1). When pulsed with violet light at 405 nm in one-photon, or 830 nm in two-photon, the novel photo-switchable bioluminescent molecule (developed by collaborator Nathan Shaner) Ofo shifts its emission wavelength from 455 nm to 525 nm, a wavelength which stimulates the fluorescent protein for light amplification. This increased and shifted light production provides a stronger emission to activate the red-shifted opsin, VChR1. The fact that it can be photo-switched allows us to achieve robust temporal and spatial control of this activation.

A key question is whether two-photon light at the appropriate wavelengths and locations could activate the construct. In a series of experiments, I tested the efficacy of two-photon excitation at 830 nm, an equivalent of violet one-photon light, on our new PS BL-OG construct. I found this wavelength could specifically activate this molecule in Neocortex, a nontrivial objective in the development of this technology. The flexibility of this activation can be seen in Figure 6, where we selectively (literally) 'wrote in' the name of one of the leading brain science discovery environments. The time course of

PS BL-OG is one suitable for behavioral experiments on the order of minutes, and

further ongoing studies are increasing the effectiveness of this molecule for
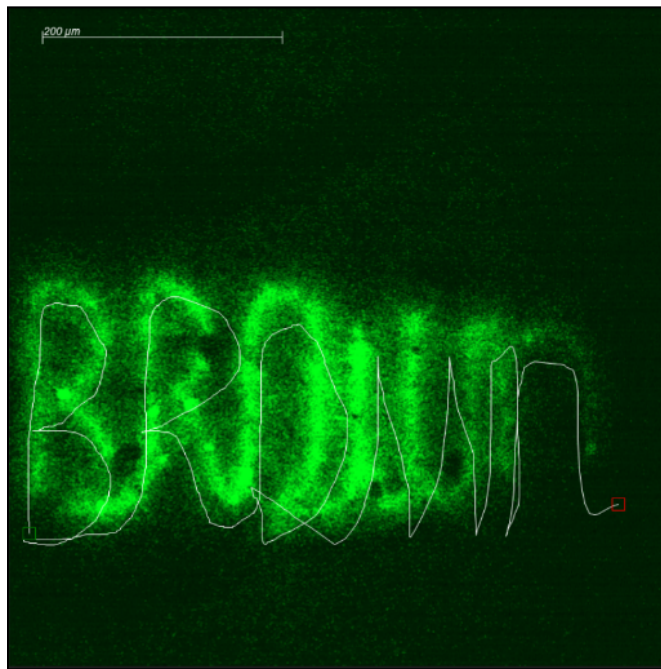
manipulation of activity-defined ensembles.

Figure 6. PS BL-OG activation of neuropil in sensory Neocortex.

Chapter 3: Neocortical Inhibitory Imbalance Predicts

Successful Sensory Detection

Chapter 3 describes the discovery of a novel Neocortical motif for sensory detection processing. Neuroscience research often addresses the activity of excitatory cells in the Neocortex. Inhibitory cells are equally critical to the balance of excitation and inhibition and sculpt circuit dynamics in Neocortex related to perception. In this original manuscript I contributed to with Dr. Christopher Deister and others, recently submitted for publication, we demonstrate that two activity-defined subtypes of fast-spiking parvalbumin-interneurons (FS/PV) demonstrate opposed dynamics during sensory detection. After initial evidence that these subgroups exhibit dual dynamics in Primary Somatosensory Neocortex (SI), I conducted a visual detection task in Primary Somatosensory Neocortex (V1) and subsequently confirmed this motif in a second Neocortical area. My testing of a pan-neuronally labeled group of mice and a FS/PV labeled group of mice led to Figure 5 of this manuscript, recently accepted for publication. The authors of this manuscript are listed below.

Deister, C. A., More, A. I., Voigts, J., Becheck S., Lichtin, R., Brown, T. C., Moore, C. I. (2023). Neocortical inhibitory imbalance predicts successful sensory detection. *In submission.*

Abstract

This Chapter is composed of research that investigates PV interneuron dynamics and the emergence of specific ensembles that predict perception and successful behavioral performance. Here, we discovered a Neocortical motif that is not only specific to primary somatosensory Neocortex, but also to primary visual Neocortex. We trained mice on tactile and visual detection tasks and recorded PV interneuron dynamics with two-photon calcium imaging in Layers II/III of sensory Neocortex. Dual separate and distinct PV ensembles emerged during task performance. One subtype predicted "Hit" trials with their post-stimulus activity, while the other predicted "Miss" trials, during tactile detection. Pan-neuronal labeling of the Neocortex and recordings from these labeled cells did not show evidence of miss-predictivity.

These ensembles led us to develop a computational model that explains the dynamics of PV and pan-neuronally labeled cells. This model explains these opposing inhibitory dynamics through imbalanced top-down excitation that selectively prioritizes certain ensembles above others. Specifically the top-down activity selects Hit cells during detection performance. The model is unique because it demonstrates that disinhibition of excitatory cells occurs when Miss cells are inhibited and thereby open a gate for the excitatory cells to carry perceptually relevant signals.

Introduction

Transient alterations in firing rate and correlations among neocortical pyramidal neurons predict perceptual performance. Fast-spiking parvalbumin-positive interneurons (FS/PV) are known to regulate these neural and network-level activity dynamics, and sensory ability, across a variety of time scales (McCormick et al., 1985; Lee et al., 2010; Siegle, Pritchett and Moore, 2014). FS/PV generate robust hyperpolarization of pyramidal neurons through highly effective somatic synapses (Kawaguchi et al., 2019; Cruikshank et al., 2007, Kubota et al., 2015). The magnitude and timing of this inhibition regulates sensory-evoked firing (Simons and Carvell, 1989; Pinto et al., 2000; Cardin et al., 2009), and the emergence of correlations on fast (millisecond) time-scales (Swallow, 2002; Cardin, 2009; Crochet et al., 2011). Based on these findings, and the broad range of inputs FS/PV integrate (Fino and Yuste, 2011), they are commonly viewed as a key final common pathway in determining the context-dependent output of a neocortical area.

While there is consensus that FS/PV are key to creating the optimal neocortical dynamics that underlie successful sensory processing, there are opposed theories concerning their role in sensory driven behaviors, where rapid feedforward integration interacts with ongoing feedback/top-down processing (Wang et al., 2013; Doiron et al., 2016). In one widely-held view, propagation of a sensory signal is enabled by suppression of FS/PV, causing disinhibition and increased firing in relay neurons. In the second view, increased FS/PV activity is crucial to creating the relative timing and rate dynamics observed in Neocortex during active processing.

Experimental evidence and multiple computational models support the first view, that FS/PV suppression is key to enhancing task-relevant firing in local relay cells (Vogels and Abbott, 2009; Wang and Yang, 2018). In rodent primary somatosensory Neocortex (SI), decreased FS/PV activity in upper Layer II predicts enhanced detection of suprathreshold vibrissa motions. Further, strong optogenetic stimulation of FS/PV suppresses detection of tactile inputs (Sachidhanandam et al., 2016), and chemogenetic suppression of FS/PV enhances detection (Chen et al., 2020). Similarly, optogenetic activation of FS/PV in V1 impairs contrast detection of visual stimuli (Glickfield et al., 2013; Cone et al., 2019). This disinhibitory/gating view of FS/PV in sensory perception is consistent with a circuit model in which upstream interneurons, most notably those expressing vasoactive intestinal peptide peptide (VIP; Zhang et al., 2014), increase their activity during active sensory processing and suppress FS/PV. This circuit model of primary sensory Neocortex has received wide support, including studies showing enhanced change detection following VIP stimulation in V1 (Wang and Yang, 2018; Tremblay et al., 2016; Cone et al., 2019).

In contrast, several studies have observed increased FS/PV activity in relevant neocortical representations during active information processing. Direct optogenetic stimulation of FS/PV in V1 can enhance visually-cued go-no go performance (Lee et al., 2012), allocation of selective attention drives greater FS firing in monkey higher visual Neocortex (Reynolds et al., 2000), and increased FS/PV rates in mouse frontal Neocortex predict task success in a selective attention paradigm (Kim et al., 2016). In SI, successful detection of vibrissa stimuli is predicted by enhanced firing of

sensory-responsive and non-sensory responsive FS (Shin and Moore, 2019), as does

emergence of endogenous and induced coherence of FS/PV firing at higher frequencies

(in the low gamma-range, 30-60 Hz) (Siegle et al., 2014; Shin and Moore, 2019).

Similarly, selective juxtacellular stimulation of single FS/PV in SI can reliably drive

detection responses in rodents trained to report vibrissa deflections (Houweling et al.,

2008; Doron et al., 2014). These data are consistent with models of signal relay that

propose that enhanced local interneuron activity can aid information processing (Garcia

Del Molino et al., 2017), including those emphasizing sharpening of tuning (Zhang et al.,

2014; Maunsell and Treue, 2006), generation of response gain through rebound from

inhibition (Tiesinga et al., 2004, Azouz and Gray, 2003), and the induction of beneficial

fast synchrony in relay neurons (Siegle et al., 2014; Shin and Moore, 2019, Sherfey et

al. 2020; Pritchett et al., 2015; Jadi and Sejnowski, 2020; Knoblich et al. 2010).

Increased FS/PV activity could also reflect the need to maintain excitatory-inhibitory

balance in a local cortical circuit under conditions when pyramidal firing increases (e.g.,

with the allocation of attention).

Further, modeling and data indicate that enhanced local inhibition can decrease

spike-count ('noise') correlations (R_{sc}). Decreased spike-count correlations are

commonly observed in neocortical areas engaged in active sensory processing,

including with the allocation of attention (Cohen and Maunsell, 2009) and the onset of

exploratory sensory behavior (Poulet and Petersen, 2008). A key computational

framework explaining the biophysics governing rate and correlation, introduced by de la

Rocha and colleagues (2007), predicts that increased rate in adjacent neurons should

parallel increased R_{sc}. This finding poses a potential conundrum, as increased firing rate is often reported in the same neocortical areas that show decorrelation (Reynolds et al., 2000; Cohen and Maunsell, 2009; Mitchell et al., 2009). Subsequent circuit models and experimental findings indicate that increased feedforward inhibition may decouple this rate-correlation dependence, leading to rate increases without parallel R_{sc} increases (Renart et al., 2010; Middleton et al. 2012). While a direct connection between such models and the neural dynamics occurring in specific cell types such as FS/PV during perception is largely unexplored, the decreased R_{sc} commonly found during active processing provides support for increased inhibition in representations engaged in information processing.

A third possibility is that functional subgroups of FS/PV play distinct roles during optimal processing, reflecting the different computational roles of their pyramidal targets (Doiron et al., 2016). Several kinds of diversity have been described for FS/PV, including anatomical and intrinsic physiological differences within Layers II/III (Markram et al., 2004; Zhu et al., 2004; Jiang et al., 2013; Lu et al., 2017), heterogeneity in sensory sensitivity and tuning (Runyan and Sur, 2013; Shin and Moore, 2019) and distinct responses to neuromodulators, running and arousal signals (Garcia-Junco-Clemente et al., 2019). As such, distinct FS/PV subgroups could play multiple distinct roles within a relevant neocortical representation.

Here, we found robust imaging and computational evidence for multiple and opposed FS/PV subgroups. To directly test FS/PV and pyramidal population dynamics that predict perception, and their generality, we conducted 2-photon imaging in SI and V1. In

both, we found that >30% of FS/PV predicted successful detection trials by modulating their firing rate, but that they were split between distinct subgroups firing more or less on hit trials. In both areas, a smaller, single group of predictive pyramidal neurons indicated detection by increased rate and correlation on hits. The majority of pyramidal neurons did not detectably change rates, and decorrelated on Hit trials.

To understand these data, we created several computational models. We found that a specific network architecture featuring opponent FS/PV subgroups could account for the rate and correlation dynamics observed across cell types and brain areas. In this circuit, decreased activity in a subgroup of FS/PV drove enhanced rate and correlation in their target, a pyramidal ensemble that predicted task performance. In contrast, increased FS/PV firing in a different subgroup balanced excitatory top-down drive to the broader population, leading to no change in firing probability in their targets, and decreased R_{sc}. Given that non-predictive neurons constitute the majority in SI (Crochet et al., 2011, Kwon et al., 2016, Shin and Moore, 2019), these computational and imaging findings are consistent with the common observation of decorrelation at the population level during active processing. This modeling framework also made novel predictions subsequently observed in the data. These findings show that FS/PV heterogeneity is a common motif across primary sensory areas, and indicate that inhibitory imbalance, supporting the creation of distinct pyramidal ensembles, is critical to optimal neocortical processing.

Methods

Animals/Surgeries. All procedures conformed to guidelines established by the National Institutes of Health, and were approved by Brown University's Institutional Animal Care and Use Committee. Eight heterozygous PV-cre (B6;129P2-Pvalbtm1(cre)Arbr/J; Silvia Arber via Jackson Laboratory) mice aged 8-11 weeks, of mixed sex, were used. All animals were housed in a vivarium on reverse light-cycle (9am-9pm dark cycle). Animals were housed singly after their initial surgery. Experiments were performed during the dark cycle. Animals were typically handled in darkness or under red LED illumination (~660 nm). On the day of surgery, healthy mice were induced into an anesthetic state with 2% isoflurane (in O_2), and injected with 0.05-0.1 mg/kg IP buprenorphine (an opiate analgesic). Isoflurane was lowered until mice reached a stable anesthetic plane, at which time the isoflurane was typically 0.5-1%. A titanium headpost was cemented to the exposed skull using strong dental cement (C&B Metabond; Parkell). The skull around the somatosensory Neocortex was thinned and flattened. A 3mm round craniotomy, centered at ~1.25mm posterior to bregma and ~3.25 mm lateral to the midline, was made[50]. Care was taken to minimize heating during the thinning and scoring process to maintain the integrity of the underlying dura.

Small (~10 nl) injections of AAV2/1-hSyn-GCaMP6s (HHMI/Janelia Farm, GENIE Project; produced by the U. Penn Vector Core) were made at a depth of ~200-300 μm around the posterior c-row whisker barrels (4-6 injections/animal), identified first by vascular landmarks (we later confirmed expression in the C1 or C2 barrel using intrinsic imaging after recovery). Injections were delivered at a rate of ~10 nl/min using a

stereotaxic-mountable syringe pump (QSI; Stoelting) modified slightly to drive a piston through a glass pipette pulled and beveled with a final tip diameter of 20-35 μm. The titer of the virus when it arrived was 2.6×10^{13} (GC/ml), which we diluted to 1.5×10^{13} (GC/ml) with PBS before injecting. A cranial window (Goldey et al., 2014) "plug" was made by stacking two 3mm coverslips (Deckgläser, #0 thickness; via Warner; CS-3R) under a 5mm coverslip (Deckgläser, #0 thickness; via Warner; CS-5R), which were adhered together with an optical adhesive (Norland Optical #71). The plug was inserted into the craniotomy and the edges of the larger 5mm glass were sealed with vetbond (3M) and then cemented in place. Care was taken to ensure the plane of the titanium headpost was level to the window's final plane, which noticeably minimized motion artifacts during imaging (Goldey et al., 2014). Dura was left intact, and generally stayed clear for many months. Animals were given at least three days to recover, at which time we performed intrinsic imaging to localize the c-row barrels, and started a water-restriction regimen. Two PV-cre animals were injected with AAV2/1-hSyn-Flex-GCaMP6s to restrict GCaMP6s expression to PV+ neurons. Three PV-cre animals were crossed to ai-14 (B6;129S6-Gt(ROSA)26Sortm14(CAG-tdTomato)Hze/J) reporter mice to visually identify putative PV+ neurons.

Behavior/Water-Restriction. Animals were placed on water-restriction for at least seven days (1-1.25 ml/day) prior to training. We interacted with animals almost daily as they were habituated to the imaging/behavioral apparatus. Once in the behavioral rig we restrained the posterior C-row whiskers, typically C1, C2 and C3. Whiskers were

placed into a L-shaped clamp that was closed 8 mm from the base of the whiskers. This clamp was attached to a piezo-electric plate bender (Noliac; CMBP09). At the beginning and end of each session we confirmed that the clamp was in the same place and held the same whiskers as when the experiment started. On the first day of training we focused on associating licking from an acrylic lick-port with whisker stimuli. Mice were imaged with a two-photon microscope (imaging details below) in a session where they received vibrissa stimulation and licked from a spout (all trials with stimulation were rewarded). After this conditioning session (100-300 trials), mice performed our behavioral task with ~1000 trials (2 sessions) of mostly highly perceptible stimuli. Once they displayed proficiency with the task (signal detection statistic for strong stimuli, $d' > 1$), all sessions were converted to 20-25% catch trials and stimuli drawn from a random interval allowing for coverage over their entire perceptible range. Mice typically ran 10-12 sessions before being taken off of water restriction. All sessions analyzed here came from days that showed a $d' >= 1$ with all stimulus amplitudes considered, even ones that were barely detectable; d' values were >2 when considering strong stimuli only.

Behavioral control was conducted using custom routines written in MATLAB (Mathworks) to interface with National Instruments DAQ boards. All waveforms were digitized at 10 kHz. Lick detection was made using an IR emitter/receiver pair (SparkFun; SEN-00241) centered across the tip of the lick-spout; the IR pair was calibrated daily. Solenoid valves (NResearch Inc.; 161T011) gated water flow and

vacuum return. Animals were free to move on a treadmill, which was tracked with a quadrature encoder (1024 counts/rev; Yumo; E6B2-CWZ3E).

We excluded trials where animals licked 500 ms before the onset of a stimulus. Sessions were aborted when animals were sated and disengaged from the task. Disengaged trials were identified by taking a running average of the animals' responses over a ten-trial block, and using a threshold of 1.5 standard deviations to define blocks of disengaged trials.

There were no stimulus cues and all behavior was done in a dark box with white masking noise present. Stimulus timing was essentially random: each trial had a fixed time of 8 seconds from a behavioral control perspective, but we randomly chose a time to insert a stimulus between 1 and 6 seconds after trial onset (100 µs increments). Stimulus amplitudes within the piezo's travel range were chosen randomly except for a fixed number of catch-trials (20-25%; stimulus amplitude=0) and maximal stimuli (5-10%), which were interleaved randomly, but had a fixed frequency. In addition, any false alarms (licking during the report window on a catch trial) led to an 8-16 second time out. The stimulus was a 20 Hz train of ten stimuli that each consisted of a fast cosine wave onset with a time to peak of 6 ms (from caudal to rostral) and a slow cosine return with a time to peak of 20 ms (from the deflected rostral point back to rest). The peak amplitude was varied to span the range of the piezo's travel and animal's psychophysical range (**Figures 1E** and **1F**).

Image Acquisition. The two-photon microscope was designed and constructed by Bruker/Prairie Technologies. We used an 8 kHz resonant galvanometer (CRS 8 kHz) for fast scanning in the x-axis, along with a non-resonant galvanometer (Cambridge 6215) to increment in the y-axis. Our imaging grids (frames) were 512 x 512 pixels and scanned in 33 ms. Pixel size was either 0.88 x 0.88 μm (Nikon 25x Objective Lens; 1.1 NA), or 0.8 x 0.8 μm (Nikon 16x Objective Lens; 0.8 NA). The objective was rotated to the same plane as the animal's window. GCaMP6s was excited by a pre-chirped Ti-Sapphire laser (Spectra Physics; MaiTai) tuned to 980 nm. Power measured at the objective entrance was 20-60 mW. Emitted photons were collected through the imaging path directed to a multi-alkali PMT (Hamamatsu; R3896) for detection (digitized with 14-bit resolution). Image acquisition was synchronized to behavioral control with TTL trigger pulses. A typical session lasted 1-2 hrs. We found no signs of activity 'run-down', substantial bleaching or cellular damage over the session, consistent with the low laser intensities used, the relatively long wavelength used to image GCaMP, and with other population imaging studies (Peron et al., 2015).

Image Analysis. All image analysis routines were written in MATLAB. Frames were collected as individual image files. A typical session produced 1-200,000 images. Most motion artifacts came from small movements in the x-y plane. Because our acquisition rate was faster than the frequency of mouse movements, we relied on rigid-body methods to align images. We used a discrete Fourier transform based method that calculated shifts with sub-pixel increments (Guizar-Sicairos et al., 2008). A registration template was constructed from averaging the first 10-100 images collected, or 10-100

images that had the lowest luminance value; both methods resulted in similarly stable images. Each image was aligned to the template. Mean and standard deviation projections of the registered stack were made, from which somatic regions of interests (ROIs) were made by hand. A binary mask from the segmented regions was made for later processing.

Fluorescence values were extracted from each ROI for each frame, and the mean for each cell was computed. In addition, we made annulus-shaped ROIs to estimate neuropil contamination (Chen et al., 2013) by eroding out 2o pixels from each somatic ROI and subtracting any other cell body that fell in this ring. This gave us two vectors of fluorescence values for the soma and the neuropil. We weighted the neuropil vector by 0.7, which was on the high side of contamination estimates we made by comparing the difference in blood vessels and their surround. The weighted neuropil vector was subtracted from the somatic vector to produce a corrected vector of fluorescence values. Images were collected at a frame rate of ~30 fps, a frame rate well above the temporal dynamics of GCaMP6s. In general, we were concerned with having an estimate of fluorescence changes in a 250 ms window. We therefore averaged fluorescence values in neighboring frames, after corrections, to get a final estimate of the fluorescence values with significantly improved signal-to-noise, but at an effective frame rate of ~15 fps (66 ms intervals).

Fluorescence value (F) traces were converted to a normalized df/f trace. We used an approach similar to previous population calcium imaging studies to estimate baseline F_o

fluorescence in each cell[52]. First, we estimated the number of events in each cell by counting the number of crossings made by the first derivative of each trace above a 2*standard-deviation threshold. This crude event rate estimate was used to rank the relative activity of neurons in one of ten bins from least active to most active. Second, we assigned quantile thresholds for baseline event rate estimates, from the median (0.5) for the least active neurons, to 0.05 for the most active neurons. Third, a sliding window (window length was 4-10 trials long (~40-80 seconds); the window shifted by one frame for each measurement) method was used to compute the F values in the lowest Nth quantile in the window (where N is the quantile threshold determined in step 2). The average of these F values were used as each frame's baseline (F_o). Lastly, F and F_o traces were used to make the final df/f trace given by ($(F(i)-F_o(i))/F_o(i)$), where i is the index for each frame. Records of df/f were grouped into trials and aligned to stimulus onsets for behavioral data for further analysis. We excluded neurons with filled nuclei[31], which we determined during segmentation by looking at time-lapse movies as well as average and variance projection images. We also looked for disproportionately long decay-time for spontaneous transients as an indication of filled neurons. These neurons comprised at most 2.2% of our imaging fields. Sensory-responsive neurons may appear to stop responding once their nucleus fills (Chen et al., 2013). The exclusion of neurons with filled nuclei, or the inclusion of neurons with filled nuclei that may have been missed, could have distorted our numbers in quantifying the number of sensory-responsive or non-responsive neurons were in our sample. Furthermore, hand-segmentation of neurons is inherently biased and GCaMP6s has a relatively low

background fluorescence, so we may have missed a number of non-responsive

neurons if they did not have an appreciable background average.

Statistical Methods. Most statistical comparisons were made using bootstrap methods,

other tests used are described in text. Differences in distributions were determined by

computing either the bootstrap distribution of mean differences or median differences (at

least 10,000 permutations for each test), depending on which metric created a normally

distributed bootstrap distribution. The 95% confidence interval was used to test null

hypothesis (the difference in distributions was zero). We aimed for an effective 95%

confidence interval, so we started with an α-value of 0.025 because all tests made were

two-tailed. We then scaled α to correct for multiple comparisons using the Bonferroni

method $(\alpha_{corrected} = \alpha/N_{comparisons})$. In the text the corrected 95% α for each test is reported

for clarity. Reported p-values were computed by determining the normal tail probability.

For experiments in which we defined a 'cut-off' for 'significant DP,' we define the 'alpha

value' in the standard way (α = 1 - confidence interval) and it defines the probability of

making a false-positive 'Type I' error. Thus, when we varied the alpha value to

determine the impact on the fraction of so-called 'hit' and 'miss' predictive neurons, by

increasing the alpha value we were decreasing our allowed confidence interval and

thereby allowing more Type I errors.

Neurometrics. For all neurons we normalized evoked df/f for different stimulus

amplitudes to the maximal value for all trials without respect to choice outcome and

conditioned on choice. We then attempted to fit every neuron's relationship between

normalized evoked df/f and stimulus amplitude with a Boltzmann-function of the form:

$y=max/(max+e^{(midPoint-X)/slopeFactor})$

where X is the independent variable (stimulus amplitude) and the fit parameters are a)

the midPoint which is the amplitude that leads to 50% of the maximal response, b) max,

which is the maximal response, and c) slopeFactor, which is the slope of the resulting

sigmoid near the midPoint. Curve fits were performed in MATLAB using a Non-linear

least squares method. We compared all neurons that had a 'good fit,' which was defined

as having an adjusted R-squared >0.5 and a midPoint within our stimulus range.

Detect Probability. We used receiver operating characteristic (ROC) analysis to

estimate Detect Probability (DP; Cook and Manusell, 2003). We used MATLAB routines

to construct ROC curves that used evoked df/f responses on threshold level trials to

determine if a choice was a Hit or a Miss, based on varying a decision variable. The

area under this curve was defined as DP. Chance prediction is a 1:1 correspondence

between correct responses and false-responses regardless of where the decision

variable was placed, which gives a straight line in an ROC plot and an area of 0.5

(**Figure 2a**). Prediction better than chance leads to values >0.5 and worse than chance

<0.5. In our case better than chance or worse than chance corresponded to whether

increased rates predicted hits (>0.5) or decreased rates predicted hits (<0.5). We

labeled these as Hit-predictive and Miss-predictive, respectively. To determine whether

our estimate of DP for each neuron was above or below chance we shuffled (1000

permutations) all trial labels and recomputed DP. We then used the resulting shuffle distribution to determine the mean DP expected by chance and variance.

Correlation Statistics. Pairwise correlations in evoked stimulus responses (noise correlation; r_{sc}) were measured by determining the Pearson's linear correlation coefficient ($r=r_{sc}$) for 'response' vectors, for pairs of neurons imaged in a session among a pre-determined group (i.e. non-predictive, hit-predictive etc.). The response vector consisted of a concatenated series of evoked df/f traces for all threshold-level hit, or miss trials. We define 'evoked df/f' here as the GCaMP6s (df/f) activity from the onset of the vibrissa stimuli and 250 ms after, which was the earliest reaction time, relative to a 150 ms baseline.

The noise correlation (r_{sc}) does not precisely, or uniquely, capture signs of direct mono-synaptic connections that can be discerned from spike train cross-correlogram (Cohen and Kohn, 2011), instead r_{sc} is proportional to the integral of a cross-correlogram on a hundred ms time-scale (Cohen and Kohn, 2011). Thus, r_{sc} captures direct and indirect cortico-cortical cell interactions, which are expected to be weak on average, but essentially ubiquitous (Ko et al., 2011). Because r_{sc} is expected to be weak, or non-existent in some cases, and subject to finite sampling, studies of this metric have relied on pooling Pearson r-values from large numbers of pairs, regardless of their p-values, and comparing these distributions to those expected from chance (which can be obtained by simple trial shuffling). For consistency, we adopted this same approach and thus did not use p-values in determining which r-values should be pooled.

We instead pooled all and confirmed that the correlation distributions were the result of true pairwise covariation that depended on the observed behavioral trial structure, and not chance.

Modeling. All neuronal models were implemented as conductance based leaky integrate and fire neurons in MATLAB using a dt of 1 μs. Each neuron's V_m was determined with the following equation: $C_m*dV_m/dt=-g_{Leak}*(V_m-E_{Leak})+I_{Syn}(t)$. When Vm reached a threshold of -40 mV a spike was logged and the membrane potential was reset to a resting value of -60 mV. The refractory period was 4 ms. I_{Syn} was the sum of an excitatory conductance and an inhibitory conductance: $I_{inhibitory}=g_{inhibitory}*(V_m-E_{inhibitory})$ and $I_{excititory}=g_{excititory}*(V_m-E_{excititory})$; C_m was 0.25 nF, E_{Leak} was -70 mV, $E_{inhibitory}$ was -75 mV and $E_{excitatory}$ was 0 mV. The synaptic conductances were modeled as an alpha-function using a decay time-constant of 5 ms for the excitatory conductance and 10 ms for the inhibitory conductance. The peak conductance (g_{bar}) was varied, but was typically in the 50 nS range. Feedforward excitation and inhibition was balanced 1:1 with inhibition lagging excitation by 5 ms. A noisy background current was applied to all neurons that was 10% of the maximal leak conductance (25 nS). Top-down excitation was modeled just as a feedforward conductance, but timed at 10 ms after an initial feedforward excitatory stimulus. Feedforward stimulus drive was modeled as a Poisson spike train with a 500 ms duration, a mean rate of 20 spikes/second and standard deviation of 20.

Results

A variety of electrophysiological correlates of detection success have been observed in

SI across species (Hyvarinen et al., 1980; Cauller and Kulics, 1991; de Lafuente and Romo, 2005; Carnevale et al., 2012; Carnevale et al., 2015; Stüttgen and Schwarz, 2008; Yang et al., 2016; Kwon et al., 2016; Sachidhanandam et al., 2013; Yamashita and Petersen, 2016; Takahashi et al., 2016; Jones et al., 2007; Chen et al., 2020). Among pyramidal neurons
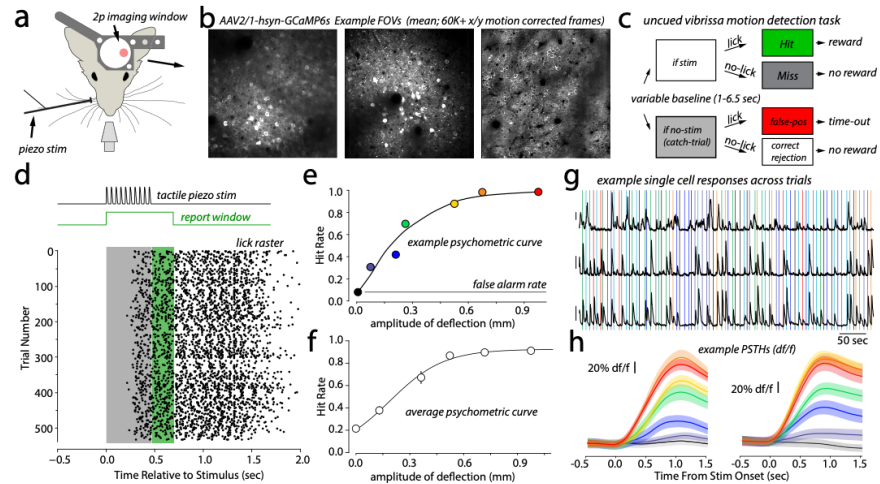
Figure 1. Population Calcium Imaging During an Uncued Tactile Detection Task
(a) A chronic cranial window and titanium 'headpost' allowed vSI imaging while trained animals licked for a water reward when they detected vibrissal stimulation. (b) Example fields of view showing the average intensity projections of > 60,000 rigidly aligned frames representing >50 minutes of continuous imaging in the C2 barrel of vS1. Data are shown from three animals that spanned the expressed range of infections. Neurons that appear to have 'filled' nuclei, are a combination of those that were filled, those that fired robustly during the task, and those that showed an integrated fluorescence value close to the exposure cutoff. *Left*, a dense infection 37 days after injection (0.2% neurons filled). *Middle*, a dense infection 156 days after injection (2.2% neurons filled; the highest percentage observed). *Right*, a sparser infection of layers 2/3 150 days after injection (0.5% neurons filled). (c) State diagram of the detection task. (d) Example session lick-raster, with lick times plotted as dots aligned to stimulus onset (zero). A lick in the stimulus presentation window (*gray*) or the extended report window (*green*) triggered water reward after the report window. (e) Psychometric/Detection curve from an example session. Hit rate is the proportion of trials in which the animal correctly reported stimulus detection by licking in the report window for a given amplitude stimulus. Example responses in *g* and *h* come from this session. (f) Average psychometric curve from six animals and eleven sessions, error bars are S.E.M.; fit is a Boltzmann-function. (g) Three example single cell responses. Each vertical bar represents a stimulus presentation of a particular amplitude (color code is the same as in e). Due to variable dwell time between trials, some traces show abrupt transitions towards the beginning and end of trials that result in apparent deviations from exponential decay. (h) Mean stimulus-aligned and normalized GCaMP6s signals (evoked df/f PSTHs) for two example sensory neurons (color code as in e).

in the vibrissae region of rodent primary somatosensory Neocortex (vSI; barrel cortex),

signals that predict successful detection include large-amplitude Ca^{2+} spikes in a subset

of Layer 5 neurons (Takahashi et al., 2016), enhanced subthreshold membrane potentials among nearly all pyramidal neurons of Layers 2/3 (Yang et al., 2016; Kwon et al., 2016; Sachidhanandam et al., 2013; Yamashita and Petersen, 2016), and enhanced action potential firing in the mean response (Shin and Moore, 2019), driven by a relatively small subset of these neurons (Yang et al., 2016; Kwon et al., 2016).

We built on this well-established precedent to assay the role of FS/PV. Head-fixed mice were trained on a vibrissae motion detection task, in which they reported randomly timed passive vibrissae stimuli by licking for a water reward, but otherwise withheld their licking responses when not presented with a stimulus (**Figures 1a, 1c and 1d**). A *false-alarm* was a trial where the mouse licked on a *catch trial*, where a randomly assigned zero amplitude sham-stimulus was presented (**Figure 1c**). *Correct rejections* were trials where mice did not lick on a catch-trial. The frequency of false-alarms relative to catch-trials was defined as the *chance* false-alarm rate. For this sample (n=6 mice), in vSI the average false-alarm rate was 21 ± 10% (mean ± SD) and showed a range of 3-31% (**Figure 1f**).   The amplitudes of presented stimuli varied randomly across trials, allowing us to determine the animal's psychophysical sensitivity range and threshold for each session (**Figure 1e**) relative to its chance report rate.

We interleaved highly salient *maximal stimuli* to help monitor task engagement (Chen et al., 2020). Disengaged blocks of trials were defined as those where the consistency in mean response rate to the maximal stimuli began to skew the otherwise normally-distributed correct response distribution, and showed little correlation with

underlying stimulus amplitude variations. This filtering helped ensure that misses were likely due to faster subjective trial-to-trial state variations (Yang et al., 2016; Kwon et al., 2016; Sachidhanandam et al., 2013; Yamashita and Petersen, 2016) rather than slower changes in criterion or motivational shifts (Hyvarinen et al., 1980; Carnevale et al., 2012; Carnevale et al., 2015; Carandini and Churchland, 2013; Luo and Maunsell, 2015). Psychometric curves with and without blocks of disengaged trials revealed that disengaged trials limited responses to all stimuli (linear scaling of the response curve), as opposed to mice developing a strategy of selectively responding (non-linearly) to easier stimuli. The mean reaction time for threshold-level deflections was 303 ± 11 ms (mean ± S.D.).

Head-fixed Imaging During an Uncued Vibrissae Detection Task

The activity of well-defined Layer 2/3 neurons (101-253/session) was imaged in behavioral sessions through a chronic cranial window (**Figures 1a** and **1b**) using two-photon calcium imaging. Imaging fields were centered on the boundaries of a barrel column (identified with intrinsic optical signal imaging) corresponding to one of the deflected vibrissae (**Figure 1b**; generally, the C1 or C2 barrel). We employed GCaMP6s (Chen et al., 2013), used previously in high resolution activity mapping of vSI (Peron et al., 2015) and for estimating rate and correlations in SI during behavior (Yang et al., 2016; Kwon et al., 2016). The sensitivity of GCaMP6s was sufficient to discern activity throughout the psychophysical range in many neurons (**Figures 1e, 1g** and **1h**). Our imaging fields were ~450 µm x 450 µm (**Figure 1b**), obtained at 15-30+ frames per second using a resonant galvanometer to scan the excitation laser. The kinetics of

GCaMP6s are relatively slow and are best interpreted as reflecting the relative spike rates integrated over hundreds of milliseconds. This approach allows measurements of relative rate changes and R_{sc} on >100 ms timescales, as in many perceptual studies linking behavioral dynamics to rate and correlation changes (Cook and Maunsell, 2002; Cohen and Maunsell, 2009; Cohen and Kohn, 2011; Gomez-Ramirez et al., 2014). Discerning precise action potential timing relative to each stimulus, and spike synchrony, was not possible. Image distortions caused by mouse movements were corrected using rigid-body methods (see *Methods* for
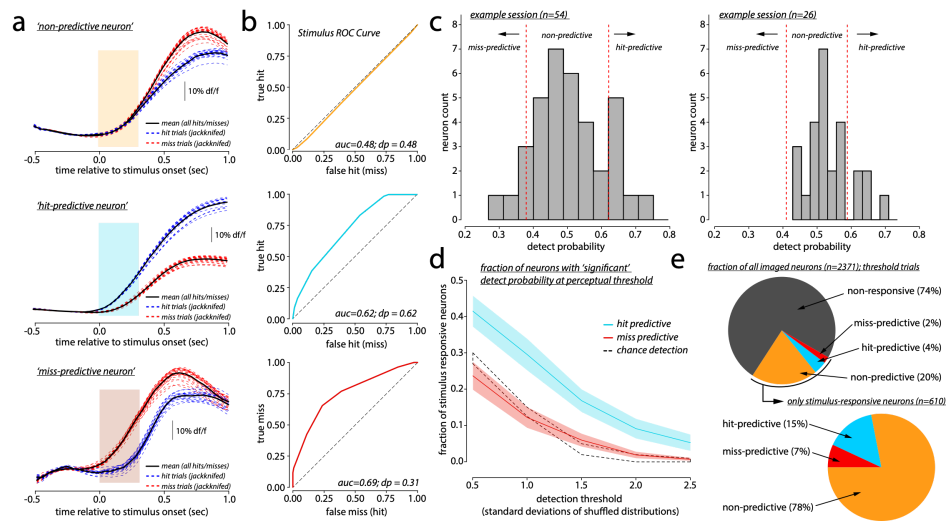

Figure 2. Perceptually Informative Rate Changes Among Putative Pyramidal Neurons at Threshold (a) Example responses at perceptual threshold on hit and miss-trials for three neurons imaged in the same session. Each blue and red dashed line is one of all possible jackknife (leaving trials out) permutations of the mean for hit and miss trials, respectively. The range of these curves is equivalent to the standard error of the mean, but allows a clearer insight into whether small groups of trials biased the mean. The thicker solid black lines in each jackknife group are the mean. The colored block that starts at 0 ms, and ends at 250 ms shows the temporal window used for our analyses. Top, the majority of sensory-responsive neurons showed chance performance at predicting the animal's detection report (hit vs. miss). We term these neurons non-predictive throughout the rest of the study. Middle, other neurons showed increases in evoked df/f on hit trials when compared to misses. We term these neurons as hit-predictive. Bottom, a smaller fraction of neurons showed greater df/f on miss-trials compared to hits. We termed these miss-predictive. (b) The resulting ROC curves for each of the examples in a. The inset of all curves show the area under the curves (auc) and the detect probability (DP). Note, that for the miss-predictive neuron the auc and DP are inverted (relative to 0.5; which was chance). (c) Detect probability (DP) for sensory-responsive neurons imaged in two example sessions, with variations in total neuron count. The vertical red lines are the 95% confidence intervals computed for the sample, shown here for reference. These confidence intervals were our statistically-defined cut-off for determining hit- and miss-predictive cells. (d) The fraction of stimulus-responsive neurons characterized as significant hit- (aqua lines) and miss-predictive (red lines) as a function of changing the alpha value. The black dashed lines are the upper and lower bounds using the same cut-offs in the shuffled data (chance observation). (e) Pie-charts summarizing the proportion of predictive types as a proportion of all cells imaged (top), or of sensory-responsive neurons (bottom).

each stimulus, and spike synchrony, was not possible. Image distortions caused by mouse movements were corrected using rigid-body methods (see *Methods* for

description). We placed mice on a linear treadmill that was continuously monitored for motion with a quadrature encoder. While mice had the option to run and move, they were stationary during the analyzed high-performance epochs. Small motions were common when animals licked for water rewards, and these data were not included. While trials with pre-stimulus motion were excluded, when we included the few trials with motion before or during stimulus presentation, psychometric curves, and our estimates of choice-conditioned firing rate differences, were not affected.

Overall Firing Rate Changes that Predicted Detection Success

Vibrissal stimuli are known to drive spiking in a relatively small proportion of neurons in Layers 2/3 of vSI (Yang et al., 2016; Kwon et al., 2016; Sachidhanandam et al., 2013; Yamashita and Petersen, 2016). We focused the present analyses on neurons that showed detectable sensory evoked activity. To classify neurons as sensory responsive, and to test the robustness of this classification, we used two commonly employed methods that compare responses to trials without vibrissae stimuli (Methods). Selection using cell-by-cell alpha criterion or population standard deviation cut-offs led to similar proportions of classified neurons, and the vast majority of classified neurons were the same in each case (0.24 ± 0.03 for 0.05 alpha detection vs. 0.26 ± 0.03 for a 1.5 standard deviation cut-off). We chose to use a standard deviation cutoff of 1.5 (corresponding to an alpha value of 0.05) as our 'benchmark' throughout the remainder of the study. This fraction of spike-responsive neurons is within the range of estimates typically made in Layers 2/3 of vSI (Peron et al., 2015; Stüttgen and Schwarz, 2008; Yang et al., 2016;

Kwon et al., 2016; Sachidhanandam et al., 2013; Yamashita and Petersen, 2016;

Takahashi et al., 2016; Chen et al., 2020).

A Small Group of SI Neurons Predicted Detection Success with Increased Rates

Ideal observer analysis was used to determine the fraction of trials each sensory

responsive neuron's stimulus-evoked df/f, integrated 0-250 ms post-stimulus, could

predict go from no-go responses. Correct classification rate was defined as the integral

of the receiver operating characteristic (ROC) curve (see Methods for details). This

integrated metric, in the context of detection tasks, is commonly referred to as "detect

probability" (DP)(Carnevale et al., 2012; Carnevale et al., 2015; Yang et al., 2016; Kwon

et al., 2016; Smith et al., 2011; Cook and Maunsell, 2002). We limited analysis to

GCaMP activity from 0-250 ms post-stimulus (**Figure 2a**; *colored blocks*). This

restriction helped ensure analyzed firing rate changes were not the result of overt motor

(e.g., tongue) responses.

In these ROC analyses, neurons can either show higher rates that predict hits, no

change, or higher rates that predicted misses. For most binary-classification problems,

ROC curves are above the unity line, and thus classification can be at chance (0.5;

Figures 2a and **2b**, *top*) or greater than chance (>0.5; **Figure 2a**, *middle*). Here,

performance 'worse than chance' (<0.5; **Figure 2a** and **2b**, *bottom*) corresponds to

higher firing rates on Miss trials than on Hit trials. For plotting purposes only, we inverted

the relationship between hits (i.e. sensitivity vs. specificity) and misses (i.e. specificity

vs. sensitivity) for neurons whose initial DP was <0.5 (**Figure 2a** and **2b**, *bottom*).

When all neurons classified as stimulus responsive were pooled, mean DP was 0.52 and the standard deviation was 0.09. This value is statistically greater than chance (p<0.002; Wilcoxon Rank Sum Test), and similar to aggregate data from SI in monkey and rat tactile detection studies (de Lafuente and Romo, 2005; Carnevale et al., 2012; Carnevale et al., 2015; Stüttgen and Schwarz, 2008).

We determined if, and how many sensory driven neurons in SI showed significant DP (Yang et al., 2016; Kwon et al., 2016) by first determining chance performance by shuffling trial outcomes and repeating standard ROC analysis for each neuron to produce a standard deviation estimate of the shuffled mean value (± 1.5 standard deviations was defined as significant). Under our conditions, this value corresponded to an alpha value of 0.05 and therefore a confidence interval of 95% (see Methods). **Figure 2c** shows DP from stimulus responsive neurons in two example sessions, and the bounds of the detection cut-off (*red vertical lines*). For our chosen significance cut-off (1.5 S.D./alpha=0.05), we found that 16.8 ± 3% of sensory responsive neurons were Hit predictive at threshold (**Figure 2d**). Hit predictive neurons were present in every imaging session. Miss predictive neurons were a much smaller proportion of neurons on average (6 ± 2%), effectively at chance levels (**Figure 2d**). We also did not observe Miss predictive neurons in all sessions. To systematically determine the degree to which the choice of cut-off influenced classification of Hit predictive neurons, we tested a range of significance criteria. For all criteria measured, the rate of observation of Hit predictive neurons was well above chance levels (**Figure 2d**, *blue curve*). Moving

our cut-off from an alpha value of 0.05 to a more liberal 0.15 resulted in an increase from 16.8% of hit-predictive neurons to 29.1%. Making our criteria more conservative (0.02) decreased this fraction to 9.1%. Further, there was no correlation between each session's standard deviation value (the classification threshold) and the fraction of Hit predictive neurons detected (p=0.56; n=14).

A potential technical confound that could impact the estimate of DP using calcium imaging is how close, or far, a given neuron's evoked GCaMP transients are from its saturation point. A neuron whose calcium buffers/indicators are near saturation could fail to report a difference in evoked df/f for the same stimulus on hit and miss trials because of a 'ceiling effect.' Also, GCaMP concentration variations could impact reliability in reporting activity due to signal-to-noise limitations. Deterministic examination of these issues in all neurons would require simultaneous electrophysiological recording from each, obviating the utility of imaging. However, the baseline fluorescence of each cell is correlated with these factors, allowing us to test the relation between high-expression, low-expression, or distance from saturation with DP in our sample. We computed these correlations for our entire sample on a session-by-session basis and found no correlation between baseline fluorescence and DP.

Determining Relationships Between Spike Count Correlations and Rate

The preceding results and analysis re-confirms that a subgroup of SI neurons can reliably predict detection signaling by examining changes in their sensory-evoked firing

rates. We then asked if these neurons show distinct correlations that could also predict detection? Or, if sensory-responsive neurons without rate-changes could predict detection with changes in their correlation states?

To test these hypotheses, we quantified the relationship between perceptual report (detection) and spike count correlations among neurons. The degree of correlation in the spiking responses among neurons to repeated presentations of identical stimuli is often measured on the hundreds of milliseconds timescale and are referred to as 'spike-count' correlations (R_{sc}; Cohen and Kohn, 2011; Smith et al., 2011; Shadlen and Newsome, 1998; Cohen and Maunsell, 2009; Mitchell et al., 2009; Middleton et al., 2012; Ruff and Cohen, 2014; Moreno-Bote et al., 2014; Doiron et al., 2016). Such correlations emerge because neurons can have shared variance that comes from common local synaptic connections or common drive, such as that conferred by cortical feedback ('top-down') inputs (Shadlen and Newsome, 1998; de la Rocha et al., 2007; Ko et al., 2011). Thus, the interactions in SI that confer DP to a group of pyramidal neurons may increase spiking correlations between the group 'selected' by common modulation. Increased correlations are also expected amongst hit-predictive neurons because increases in rates will cause increases in correlations, not only due to increases in chance spike overlap, but also because of intrinsic properties of neurons interacting with their input currents (de la Rocha et al., 2007). Despite these predictions, under many behavioral circumstances and across systems, spiking correlations have been observed to decrease under conditions in which rates in many neurons increase (Cohen and Maunsell, 2009; Mitchell et al., 2009; Ruff and Cohen, 2014). These

findings beg the question of whether those specific neurons showing rate increases also show correlation increases, in contrast to decorrelation amongst randomly-selected cells in the broader population.
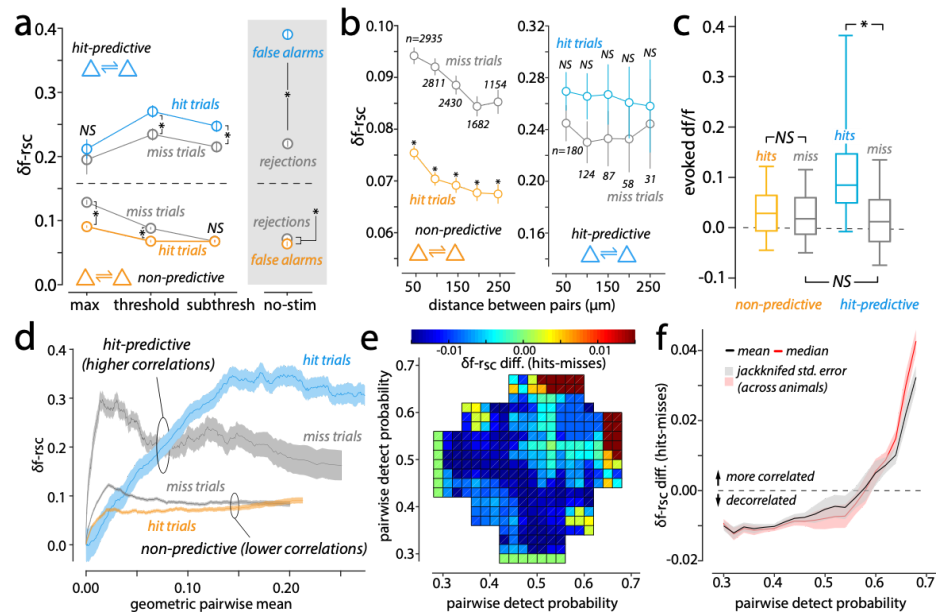
Figure 3. Distinct Spike Count Correlation Dynamics Between Predictive and Non-Predictive Neurons. (a) GCaMP-derived spike count correlations (δf-r_{sc}) for different stimulus amplitudes. δf-r_{sc} was calculated as the trial-by-trial correlation (Pearson product-moment correlation) between two neurons' evoked df/f responses. The mean δf-r_{sc} $\pm$ s.e.m. is shown for all pairs for different stimulus amplitudes denoted by each group name on the x-axis. The graph is divided by the *dashed line* by pairs that are 'choice-conditioned,' with δf-r_{sc} calculated between pairs of either hit-predictive neurons (blue dots vs adjacent gray dots) or non-predictive cells (orange dots vs. adjacent gray dots). Asterisks denote significant differences (p<0.0125; see text for details) between Hit and Miss trials for that stimulus bin, and NS denotes differences that were non-significant. (b) *Left*, δf-r_{sc} binned as a function of distance between all non-predictive pairs (left, orange/gray) and hit-predictive pairs (right, blue and gray) on threshold level trials. The number of pairs in each distance bin is noted below each gray dot. Asterisks denote significant differences (p<0.001; bootstrap difference test) between hit and miss distributions for each distance bin. (c) Box-plots showing the average stimulus-evoked df/f magnitude for non- and hit-predictive neurons. Left two columns show non-predictive evoked df/f measured on hit-trials (orange) and miss-trials (gray), these differences were not significant denoted by NS (p>0.5; bootstrap difference test). The remaining columns show hit-predictive evoked df/f also measured on hit-trials (blue) and miss-trials (gray). These differences were significant (p<0.001; bootstrap difference test). The NS noted between both groups' miss-trials indicates a non-significant difference (p>0.5; bootstrap difference test). (d) δf-r_{sc} plotted as a function of the geometric mean of stimulus-evoked df/f magnitude for hit-predictive cell correlations (blue vs gray; hit- and miss-trials, respectively) and for non-predictive cell correlations (orange vs. gray; hit- and miss-trials, respectively). (e) 3-D plot of DP for all neurons (predictive and non-predictive) and r_{sc} difference. The x and y axes indicate the DP and the color (legend at the top) is the mean difference in r_{sc} for each bin. Data were pooled from 12 sessions and 5 mice. (f) The 'marginal' mean (black) and median (red) from the data in *d*. This plot is essentially a 2D representation of *c*, made by averaging in z along the diagonals, starting from the center out. Error bars are the standard error (of the mean or median) computed by jackknifing (leave one out) the matrix in *c* on a session-by-session basis. Each animal contributed to the variance to a similar degree.

To test whether distinct correlation dynamics occurred within groups of neurons defined by whether their rate changes predicted task performance, we analyzed fluctuations in evoked df/f as a proxy for spike count (Yang et al., 2016; Kwon et al.,

2016; Peron et al., 2015; Ko et al., 2011) and computed spike-count related correlations

($\delta f\text{-}r_{sc}$) between pairs of significant hit-predictive and non-predictive sensory driven

neurons as the Pearson product-moment correlation between each cell's evoked df/f for

all trials meeting a conditioned criteria. The magnitude of df/f is related to the number of

spikes a neuron fires in time-windows of a few hundred ms. Because spike-count

correlations are measured from wide time-windows (hundreds of ms to many seconds),

the use of df/f from a Ca^{2+} indicator as a proxy of integrated spike count is reasonable.

That said, while df/f has previously been used to estimate spiking correlations (Ko et al.,

2011; Kwon et al., 2016), the df/f-derived correlations could give quantitatively different

values than those observed using electrophysiology. This potential quantitative, but not

qualitative, discrepancy exists among different methods of recording spikes (Cohen and

Kohn, 2011). While no nomenclature has emerged, we will refer to df/f derived

spike-count correlations as $\delta f\text{-}r_{sc}$ throughout the paper.

Non-Predictive Neurons Show Lower Spike Count Correlations on Hit Trials

In agreement with prior studies showing that decreased correlations typify engaged

Neocortex, the more numerous non-predictive neurons in our sample showed

decreased correlations on threshold-level Hit trials when compared to Miss trials

(**Figure 3a**, bottom portion of the figure; *orange* (hits) vs. *gray* (misses), * = p<0.0001

bootstrap mean difference test; see Methods for details). These findings occurred

despite there being no detectable change in the mean firing rate of this group (**Figure

3c**). Dynamics in SI are known to impact the perception and representation of threshold

level stimuli (LaMotte and Mountcastle, 1979; Cauller and Kulics, 1991; Siegle et al.,

2014; Chen et al., 2020) but they could have a different relationship to maximal stimuli. We therefore examined responses evoked by highly salient large amplitude deflections and also found more decorrelated responses on Ht trials (**Figure 3a**, *bottom*, dashed line 'max'; p<0.0001 bootstrap mean difference test). We also found a small but significant difference in δf-r_{sc} when we compared correctly rejected catch trials to false alarms (**Figure 3a**; bottom of the grey portion, dashed line 'no-stim'; p<0.001 bootstrap mean difference test). This result suggests that decorrelation is driven in part by choice related dynamics, and is not only a factor of stimulus variation.

Predictive Neurons Show Enhanced Spike Count Correlations

We next analyzed δf-r_{sc} amongst neurons that showed significant DP. Across all choice-conditioned trial types (hits, misses and false-alarms), hit-predictive neurons were more correlated than non-predictive neurons (**Figure 3a**; compare above and below dashed line; p<0.00001 bootstrap mean difference test). Further, significant DP neurons showed higher δf-r_{sc} on Hit trials versus Miss trials, opposite to the decreased correlations in the general population of non-predictive cells (**Figure 3a**, above dashed line, blue vs. gray; p<0.0001 bootstrap mean difference test). No significant increase in correlations was found for highly salient 'maximal' stimuli on hits versus misses, but an increase for the weakest stimuli, below threshold, was observed (**Figure 3a**, above dash blue vs. gray, label 'subthresh'; p<0.0001 bootstrap mean difference test). We also found increased δf-r_{sc} on false-alarm trials (**Figure 3a**, above dash gray vs. blue, label 'max'; p<0.0001 bootstrap mean difference test). This enhancement was larger than that observed when stimuli were present, suggesting that the perceptually-dependent

change in correlation state is in part driven by dynamics unrelated to the stimulus *per se*, such as feedback projections, and also that for the most informative neurons, the correlations created by feedback 'drive' may be partially offset by processes engaged by local stimulus-evoked dynamics blue (Kwon et al., 2016).

The magnitude of r_{sc} typically decreases with distance between neurons, in part due to functional local synaptic connectivity decreasing exponentially in Neocortex with distance (Ecker et al., 2010; Cohen and Kohn, 2011). Thus, differences in correlation magnitude between non-predictive and hit-predictive neurons could result from a systematic sampling bias if there were major differences in average pairwise distance. Suggesting modest clustering of task-predictive behavior, a small but statistically significant difference in average pairwise distance between non- and hit-predictive neurons was observed (160 ± 14 vs. 120 ± 22 µm, respectively, $p<0.00001$ bootstrap difference test). To test whether distance effects could explain the δf-r_{sc} results, we compared δf-r_{sc} on Hit and Miss trials as a function of pairwise distance within each group. We found that non-predictive neurons showed a decrease in δf-r_{sc} as a function of distance, as observed in the general population in prior studies (**Figure 3b**, left; asterisks denote $p<0.01$, bootstrap mean difference tests, post Bonferoni correction). Over all distances, non-predictive neurons showed lower δf-r_{sc} values on Hit trials when compared to misses (**Figure 3b**, right, $p<0.0001$ bootstrap mean test). In contrast, hit-predictive neurons showed little distance dependence to δf-r_{sc} (**Figure 3b**, right, $p>0.05$ all groups, bootstrap mean difference tests post Bonferoni correction). These

data indicate that the increased $\delta f\text{-}r_{sc}$ among Hit trials was not a by-product of a distance sampling bias.

Non-predictive and hit-predictive neurons are defined by the degree to which their mean rates for threshold stimuli differ by behavior outcome. Thus, there is no reason to believe the difference in non-predictive neuron correlations are explained by rate changes (de la Rocha, 2007). For our sample, firing rates between hit- and miss-trials for non-predictive neurons did not differ significantly, but they did for hit-predictive neurons (Figure 3c). However, we sought to determine if there might still be a systematic relationship between rate and correlation if neuron pairs of similar rates were compared. To do this, we computed the pairwise geometric mean of threshold-evoked df/f for all simultaneously observed pairs (as in **Figures 3a,3b, and 3c)** and their $\delta f\text{-}r_{sc}$ for threshold level stimuli only. We ordered all pairs from lowest to highest geometric df/f and calculated a running average and standard error (**Figure 3d**) for threshold level Hit trials (*colored blue for hit- and orange for non-predictive*) and Miss trials (*gray*).

For both non-predictive and significant DP neurons, a sharp rise in $\delta f\text{-}r_{sc}$ was observed for increases in rate within a narrow range around the lowest relative firing rates. Beyond this point, rate and correlation showed more complex relationship. Stimulus driven cells with no significant DP showed lower correlations on hit trials across a wide range of relative firing rates (**Figure 3d,** *orange vs. gray*), except at the highest rates where Hit and Miss trials converged. Pairs of higher DP cells showed differences in their rise, with a slower rise on Hit trials leading to lower correlations for pairings with low

firing rates. However, across most rates, significant DP cells showed greater

correlations on Hit trials (**Figure 3d,** *blue vs. gray*). And, for most pair-wise evoked df-f

magnitudes, the correlations for Hit-predictive pairs were higher than non-predictive

pairs. In sum, for most of the range of rates observed, neurons with significant and high

DP had higher correlations on Hit trials while neurons with no DP, and therefore no

significant detection-dependent rate change, show marked decorrelations. These

decorrelations are not explained by subtle rate decreases, because across the range of

observed rates, spiking decorrelated.

The above analyses employed a statistical criterion to segregate non-predictive versus

hit-predictive neurons. We next examined the continuous relationship between

task-predictive rate changes and correlations across the range of neuron pairs, without

segregation. We computed $\delta f\text{-}r_{sc}$ and DP for all sensory-responsive neurons in each

session and computed the change in $\delta f\text{-}r_{sc}$ between hits and misses. These data are

represented as a three-dimensional plot in **Figure 3e**, where the x and y-axis shows the

DP of each neuron in a pair, and color from cool to warm represents the $\delta f\text{-}r_{sc}$ difference

between hits and misses. As suggested by prior analyses, a relatively small group of

neurons with the highest DP demonstrate increases in correlation on Hit trials, while

neurons of intermediate, or chance, DP showed generally decorrelated responses.

Figure 3f visualizes this same relationship by plotting the 'marginal moments' (mean or

median of the pooled values between rows and columns along the diagonal) of $\delta f\text{-}r_{sc}$

against DP. The error bars show the jackknife derived standard error made by leaving

sessions out one at a time. This plot shows a distinct inflection for correlation increases

for DP values greater than 0.6, similar to the value we employed as a statistical cut-off (**Figure 2c**).

FS/PV Interneurons Show Robust Detect Probability, Including Pools of Cells with Hit- and Miss-Predictive Rate Increases

The above analysis predominantly reflects the dynamics of Layers 2/3 pyramidal cells, as we employed a non-specific neuron-targeted viral promoter in those experiments. In those data, neural dynamics that predict detection performance in SI are typified by rate increases in a small number of sensory responsive pyramidal neurons and correlation increases in those cells. In contrast, choice-invariant sensory responses were found in the majority of responsive SI neurons, that also showed decorrelation in spiking. These results were not, however, trivially a product of rate, as they were robust across a large range of matched rates. As modeled explicitly below, rate is not the only determinant of correlation, as balanced inhibition can also play a key role in promoting decorrelation (de la Rocha, 2007; Middleton et al., 2012; Renart et al., 2010; Doiron et al., 2016).

Parvalbumin-positive interneurons (PV+; 'fast-spiking') are an important regulator of vSI dynamics in perception, as they provide the majority of 'feedforward' inhibition evoked by sensory drive. The impact of PV+ neurons on correlations among excitatory neurons could have distinct effects depending on the time scale considered. On fast time scales (milliseconds), coordinated inhibition from PV+ cells in SI temporally focuses, and can synchronize, spiking across local pyramidal neurons (Cardin et al., 2009; Veit et al., 2017; Wang and Buzaki, 1996; Shin and Moore, 2019). However, theoretical work has

shown that, when rate correlations are considered on time scales of hundreds of

milliseconds, feedforward inhibition can decorrelate spiking responses even among

neurons showing rate increases (Middleton et al., 2012; Womelsdorf et al., 2014). While

inhibitory neurons must act in a correlated manner to augment synchrony (Wang and

Buzsáki, 1996; Gibson et al., 1999), it is not clear what the pattern of PV+ neuron

activity is under circumstances when slower spike-count correlations decrease.

Population level recordings of PV+ neurons during perceptual behaviors have been

limited due to a combination of technical challenges. PV+ neurons comprise a relatively

small group of all neocortical neurons in Layers 2/3, and a combination of their

propensity to fire at high rates while also maintaining low baseline intracellular Ca^{2+}

levels, makes Ca^{2+} imaging challenging (Chen et al., 2013). Nevertheless, GCaMP6s

has sensitivity sufficient to reveal PV+ neuron dynamics in awake mice, albeit with

slower responses and compressed dynamic range (Chen et al., 2013; Ringach et al.,

2016; Garcia-Junco-Clemente et al., 2019). To address the role of PV+ neurons in SI

during detection, we imaged their activity in two ways, first using cre-dependent

GCaMP6s expressed in the PV-cre mouse (**Figures 4a** and **4b**), and second, using a

cre-independent GCaMP6s construct in PV-cre mice that were crossed with a

cre-dependent LSL-tdTomato reporter animal (Ai14). The latter strategy allowed PV+

identification within the general population by their expression of tdTomato. Both

expression approaches revealed sensory evoked activity in a large proportion of PV+

neurons, with similar signal variance as pyramidal neurons, but with smaller peak df/f

values (**Figure 4b**. The quality of GCaMP responses based on frequency and

signal-to-noise characteristics were similar between cre-dependent and

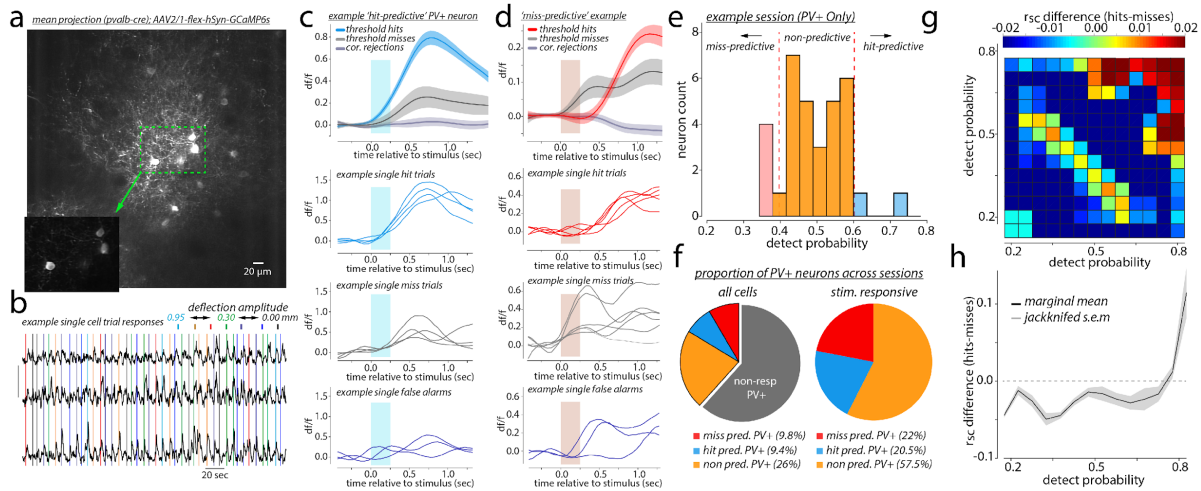cre-independent identification methods, and therefore the data were pooled. This

Figure 4. Perceptually Predictive Rate Dynamics Among PV+ Interneurons (a) Example field of view (mean of 80,000 x/y motion corrected frames) from a PV-Cre animal injected with AAV2/1-hSyn-flexed-GCaMP6s. The main image is exposed to show most neurons. The inset shows the brightest neurons (*green box*) exposed to show their non-saturated appearance. All neurons in this field showed nuclear exclusion. (b) Single cell responses for three example neurons from the field of view in *a*, over a number of adjacent trials. The y-scale bar is 20% df/f. Vertical colored lines denote onset of vibrissa deflections (amplitude is color coded; 0 mm trials were catch-trials). (c) An example of a stimulus-driven, and hit-predictive PV+ neuron. *Top*, trial average responses for Hit (blue) and Miss (red) threshold trials, and correctly rejected catch-trials (no-stimulus trials; gray lines). Solid lines at the mean, opaque envelope is s.e.m. The aqua box starting at time=0 denotes the period of time (0-250 ms, post-stim) that was used to compute detect probability. *2nd from top*, four example threshold Hit trials. 3rd from top, four example Miss trials. Bottom, all three false alarm trials (*purple*) from this session. (d) Same as c, but for a miss-predictive neuron. (e) Distribution of Detect Probability (DP) from PV+ neurons in an example session. Dashed red lines denote the significance cut-off, as in *Figure 2C* (f) Pie charts summarizing the proportion of hit-,miss- and non-predictive neurons within main 467 neuron sample (*left*), and the sub-sample of 214 stimulus-responsive PV+ neurons (*right*). The color code and proportions are given in the figure. (g) 3-D plot of DP for all neurons (predictive and non-predictive) and δf-r_{sc} difference.The x and y axes are DP and the color (legend at the top) is the mean difference in δf-r_{sc} for each bin. (h) The 'marginal' mean (*black*) from the data in *g*. This is a 2D representation of c, made by averaging in z along the diagonals, starting from the center out. Error bars are the standard error of the mean computed by jackknifing (leave one session out) the matrix in c on a session-by-session basis. Each animal contributed to the variance to a similar degree.

resulted in a sample of five mice total, with 467 putative-PV+ neurons imaged, and an

average of 23 imaged per behavioral session. As shown in example recordings (**Figure

4c, d**), consistent with prior studies showing a lack of PYR activity on False Alarms in SI

in a highly similar detection task (Kim et al. 2016), we also did not observe any

significant divergence in the mean response of the PV population on False Alarms and Correct Rejections during the sensory responsive period.

We hypothesized that PV+ neurons would show heterogenous DP and δf-r_{sc} relationships that reflect the heterogeneity observed among pyramidal neurons. A larger proportion of identified PV+ neurons showed significant DP than neurons from the general population (42.5 ± 6.1%; **Figure 4f**). Approximately half of PV+ neurons with significant DP showed higher rates on miss trials

Figure 5. The Distribution of Hit- and Miss-Predictive Putative Pyramidal (PV-) and PV+ Neurons is Similar in V1 and vSI. (a) *Top*, neural activity of V1 was imaged through a chronic cranial window in head-fixed water-restricted mice trained to perform a contrast-based visual detection task. *Bottom*, state-diagram of the detection task. (b) Mean psychometric curves (n=3 mice; n=12 imaging sessions) from trained mice, showing the relationship between response-rate and contrast of the visual stimulus. (c) Histogram, and box-plot, showing the distribution of DP for putative Pyramidal (PV-) neurons pooled across sessions and mice. (d) Same as *c*, but for PV+ neurons. (e) Pie charts summarizing the proportion of hit-, miss- and non-predictive neurons within the Pyramidal (left; n=275 neurons total), and the PV sample (right; n=318 neurons total).

('miss-predictive'; 22±3%). This category was found in the general population at near to chance levels (**Figures 2d** and **2e**), consistent with the small number of PV+ neurons in the general neuronal population of Layers 2/3 (Ringach et al., 2018; Rudy et al., 2011; Kubota et al., 2011).
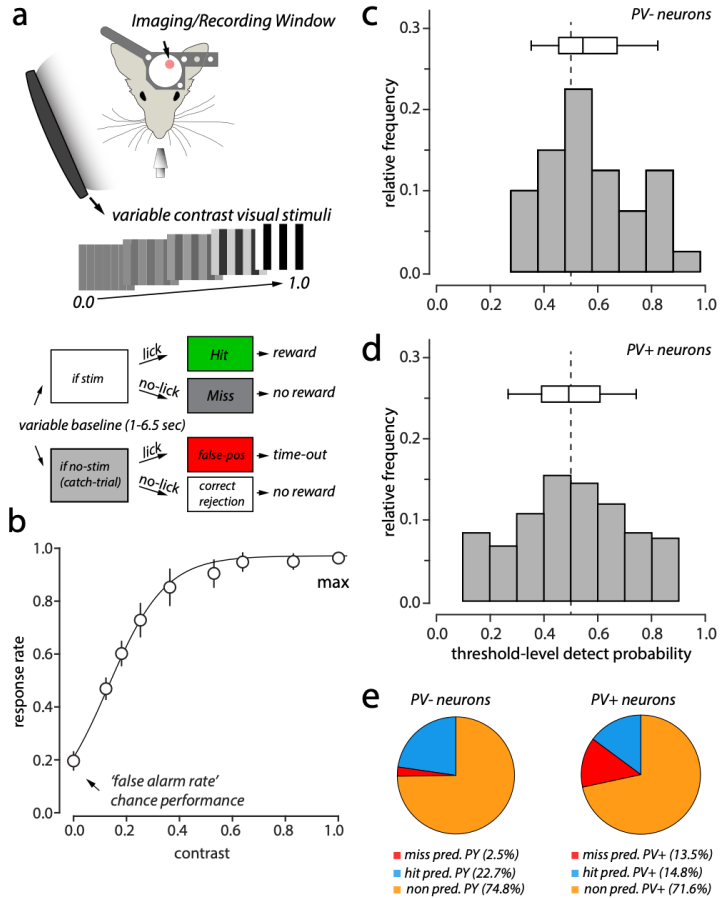
We next examined δf-r_{sc} among PV+ neurons (**Figures 4g** and **4h**) and found the same overall pattern of detection-dependent changes as in the general population. Specifically, pairs of PV+ neurons with high and significant DP values (hit-predictive) showed increased δf-r_{sc} on Hit trials, while pairs close to chance or miss-predictive were largely decorrelated (**Figure 4g** and **4h**). One prominent difference between PV+ neuron correlations and those of the general population was a diagonal region of high correlations found in the matrix left of the center (**Figure 4g**). The existence of nearly equal numbers of hit- and miss-predictive PV+ neurons, and the known dense electrical and chemical synaptic coupling among PV+ neurons[37,41,42] suggests these groups are contextually antagonistic.

PV+ Interneurons in V1 Show Task-Predictive Rate Changes that Mirror vSI

A key question begged by these vSI findings is whether the distinct groups of predictive PV+ cells are a specific feature of tactile detection, or a more common motif across modalities. To directly address this question, we trained mice on a visual contrast increment detection task (Histed et al., 2012; Glickfield et al., 2013; Histed and Maunsell, 2014; Cone et al., 2019) and carried out similar imaging experiments in primary visual Neocortex (V1) (**Figure 5a**). The structure of the task paralleled the vibrissa amplitude increment detection task, but the target stimulus was visual, and the stimulus strength was determined by contrast variation. We constructed psychometric performance curves (**Figure 5b**), and focused analyses on threshold-level trials. The mean reaction time for threshold-level contrast was 293 ± 17 ms (mean ± S.D.).

As in a subset of our vSI studies, we injected a cre-independent GCaMP6s construct in PV-cre mice crossed with a cre-dependent LSL-tdTomato reporter animal, and computed DP using evoked GCaMP6s activity on threshold-level hit- and miss-trials for PV+ (n=318 neurons from 3 mice) and PV- neurons, which are predominantly pyramidal (n=275 neurons from 3 mice). As in vSI, PV+ neurons showed a matched proportion of miss- (13.5 ± 2.8) and hit-predictive neurons (14.8 ± 3.6%; **Figures 5d**). Both hit- and miss-predictive PV+ were detected at rates greater than chance (**Figure 5e, *right***). In contrast, putative pyramidal neurons (PV-) showed a positively-skewed DP distribution (**Figure 5c**), with hit-predictive cells detected above chance (22.7% ± 4.2); **Figure 5e, *left***) but without a significant number of miss-predictive neurons (2.5% ± 1.6; **Figure 5e, *left***). These data strongly parallel those in SI. In both modalities, a relatively smaller number of PYR are predictive of behavior, and only through the emergence of cells with increased rates on Hit trials. In contrast, a larger number of PV+ predict behavior, and do so through both rate increases and rate decreases on Hit trials. This consistency in task-predictive behavior across cell types suggests that the same neural interactions among PV+ neurons and their local counterparts that predict variations in task performance around perceptual threshold exist across distinct cortical areas that subserve different sensory modalities.

How Inhibitory Heterogeneity Can Shape Outcome-Dependent Correlations

To better understand the rate and correlation findings that typify vSI and V1, and specifically the possible role of distinct excitatory and inhibitory neuron interactions, we

used computational modeling. We implemented a progression of neural and network models of increasing complexity to thoroughly follow the transformation from input correlation to output correlation with, and without, heterogenous inhibition akin to previous rate/correlation modeling efforts (de la Rocha et al., 2007; Middleton et al., 2012).

We first made a 'pool' of ten leaky integrate and fire (LIF) neurons that were not synaptically interconnected. Each neuron in the pool was subject to excitatory synaptic drive in a manner akin to a barrage of feedforward sensory excitation only. To systematically test the relationship between input conductance correlation and spiking correlation, we introduced and varied input correlations (ρ_{input}) in a controlled fashion (**Figure 6a**). In this first model, none of the LIF neurons were interconnected, so the firing of each could not introduce uncontrolled variance in the others. The drive to each neuron was a statistically generated spike train comprising random picks from a gaussian inter-spike interval (ISI) distribution with the same mean and variance. To vary ρ_{input} while maintaining the same mean and overall variance, we used Cholesky factorization. After generating a desired variance/co-variance matrix, Cholesky factorization provided a table of factors that scaled the random gaussian ISI picks for each neuron. This transformation led to a set of ten independent input spike trains with the same mean, variance and co-variance. These 'feedforward' spike trains were convolved with 'alpha-function' kernels whose shape is similar to neocortical synaptic potentials (**Figure 6a**). This convolution produced input conductance waveforms with the same ρ_{input} as the input spike trains. Importantly, this approach ensured that the ratio

of shared and unshared variance the neurons were subject to did not change as the overall rate of the neurons changed. We either convolved feedforward spike trains with just an excitatory synaptic kernel (**Figure 6a**, *top*), or an excitatory and an inhibitory kernel (**Figure 6a**, *bottom*), that was added with a delay of 8 ms to mimic feedforward inhibition (Middleton et al., 2012; Cruikshank et al., 2007).
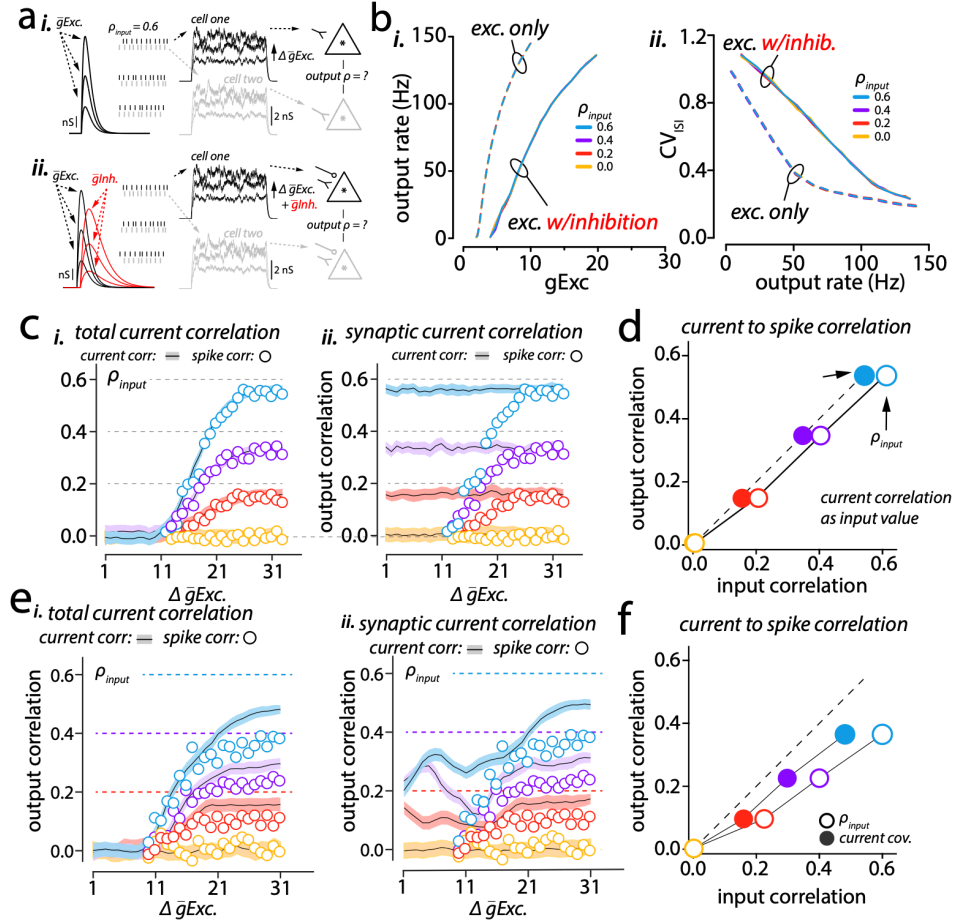

Figure 6. How Mixed Excitation and Inhibition Impact the Relationship Between Input and Output Correlations Among Simple Integrate-and-Fire Neuronal Models. (a) *i*, A "pool" of ten unconnected neurons were subject to a series of synaptic barrages that were modeled by generating "input" spike trains with a fixed correlation (ρ_{input}) and convolving a kernel that was a model waveform for an excitatory synaptic conductance. The strength of the input was varied by scaling the magnitude of the synaptic conductance kernel ($\bar{g}Exc$) to evoke "output" spiking in the model neurons at different rates. *ii*, Same as *i*, except the synaptic conductance waveform was both an excitatory conductance, and an 8 ms delayed inhibitory conductance. For models with inhibition and excitation, the strength of excitation $\bar{g}Exc$ and inhibition $\bar{g}Inh$ were varied together with a fixed proportion. (b) *i*, Plot of output spiking rate as a function of input strength, for excitation only (dashed lines) and for excitation with inhibition (solid lines). The color of each line corresponds to simulations for specific values of ρ_{input} given in the figure legend. *ii*, Same color scheme as *i*, except the CV of interspike-intervals (CV_{isi}) is plotted as a function of output spiking rate. (c) For simulations with just excitatory drive: Plots of correlation between membrane currents (*lines*), and spikes (*dots*; when drive was enough to evoke spikes) among the model neurons as a function of strength of synaptic drive. Correlations for just the intrinsic (non-synaptic) current components are shown in *i*, whereas correlations for just the synaptic components of the membrane current are show in *ii*. (d) Summary plot of output correlation as a function of input correlation for spikes (*solid dots*) and currents (*open dots*). (e) Same as c, but for simulations with excitation and inhibition. (f) Same as d, but for simulations with excitation and inhibition.

The purpose of this simple model is to allow an examination how output spiking correlations change as a function of spiking rate and ρ_{input} in a neuronal pool without any downstream, or secondary synaptic interactions, and to provide a foundation for our modeling extensions that are consistent with existing computational work and theory. Because it is known that neuronal correlations are a function of spike rate (de la Rocha et al., 2007), we varied the spiking rate of the neurons in our pool by increasing the maximal excitatory conductance ($\bar{g}Exc$), in a stepwise fashion (**Figure 6a,** *top*), or by scaling both gExc and the maximal inhibitory conductance ($\bar{g}Inhib$), scaled as a fixed proportion to $\bar{g}$Exc (**Figure 6a,** *bottom*). In de la Rocha et al. (2007), the authors derived an equation that predicts relationship between ρ_{input} and output spike correlations that emerge from excitatory drive (de la Rocha et al., 2007). The parameters that help shape this relationship, beyond the spike rate of the neurons, are the slope of the relationship between output frequency and current (FI curve), and the coefficient of variation in the output spike train's ISIs (CV_{isi}), which is the standard deviation of the ISIs normalized by mean (**Figure 6b,** *ii*). Although, their work showed that for noisy current injections and excitatory synaptic barrages, these non-rate factors have minimal impact as they are largely determined by the neuron's intrinsic properties and thus did not vary with the intensity of synaptic drive. However, these non-rate variables are all expected to be affected to varying degrees by inhibition, thereby providing a mechanism for inhibitory impact on input correlations. Thus, the first question we asked of the simple model was how does the systematic addition of inhibition to the excitatory drive, in a manner

consistent with thalamic feedforward synaptic sensory drive of sensory Neocortex

(Cruikshank et al., 2007), shape neuronal correlations?

We compared the FI curves for simulations with excitation only and excitation with

inhibition and found that these relationships were not affected by varying ρ_{input}, but did

differ in their slope (**Figure 6b, *i***). The relationships between CV_{isi} and spike rate were

also not affected by varying ρ_{input}, but adding inhibition led to an increase in ISI variability

across all rates (**Figure 6b, *i***). Both of these factors are expected to lead to an overall

decrease in output cell spiking correlation, in addition to the independent impact of rate

(de la Rocha et al., 2007).

As expected, output spike correlations (**Figure 6c**, *dots*) increased as increases in *ḡExc*

drove increases in firing rate, up to a value that was close to, but always below, ρ_{input} of

the feedforward excitatory conductance (**Figures 6c, *i***). The ultimate peak output spike

correlation was predicted by the peak total current correlation and the peak synaptic

current correlation (***Figure 6c, i*** and ***ii***, respectively; compare *dots* to *colored line plots*).

The lower spike correlations at lower spike rates are found because the total neural

conductance is dominated by uncorrelated intrinsic leak conductance, as under

conditions of weak drive, thus the leak current constitutes more of the total current than

at higher rates. This effect can be appreciated indirectly by comparing **Figures 6c *i* and**

ii, that show the total current correlation as a line with an error bar and the output spike

correlations plotted as a dot on top of the current correlation for *i* and the correlation in

just the synaptic current for *ii*. While the output correlations did not reach the input

conductance correlation (**Figure 6d**, *open circles*), when the ρ_{input} was corrected to match the level of the generated current, the maximal output spike correlation linearly correlated with the input correlation (**Figure 6d**).

Driving neural firing at different rates with excitation and inhibition also showed a clear relationship between output spike correlations and spike rate (**Figures 6e *i***). However, the steady-state output correlation when inhibition was present was always much lower than the ρ_{input} driving conductance, when compared to excitation only (compare **Figures 6c *i* & 6e *i***). Not only were output correlations reduced with inhibition, but steady-state total current correlations and synaptic current correlations were also significantly reduced (**Figures 6e *i* and *ii***). Thus, when output correlations were plotted as a function of ρ_{input}, correcting for the loss of input current correlation, as for excitation only (**Figure 6d**), was unable to account for all effects of inhibition (**Figures 6e *i* and *ii***).

Studying feedforward inhibition as deterministic ensures that its effects can be discerned without the impact of recurrent connectivity or other sources of unshared variance through synaptic connectivity patterns and/or differences in intrinsic properties between pyramidal and inhibitory neurons. However, the basic intrinsic properties of PV+ neurons and their well-described connectivity patterns in vSI ensures their impact on pyramidal neurons will likely increase as drive to the network increases. To begin to capture such features of neocortical networks, we implemented a small interconnected excitatory and inhibitory integrate and fire network subject to extrinsic input with variable ρ_{input} (**Figure 6**).

Varying ρ_{input} did not affect the FI curves of either inhibitory or excitatory neurons, but increasing G_{inhib}->G_{exc} reduced the gain of excitatory neurons and increased the CV_{isi} for all firing rates. Much like deterministic inhibition, ρ_{input} was diminished, but output spiking ρ was lowered further still for all firing rates. Likewise, steady-state output ρ was lower than steady-state ρ_{input} even when ρ_{input} was corrected for loss at the current level. Importantly, in this simple network, the relative magnitude of shared variance contributed by the inhibitory neurons was larger than ρ_{input}, because the excitatory and inhibitory neurons received statistically identical feedforward excitatory input, but the inhibitory neurons projected to all excitatory neurons. Thus, a spike in one inhibitory neuron led to inhibition in all excitatory neurons, thereby increasing ρ_{input} of the inhibitory conductance. As such, the loss of correlation in the postsynaptic excitatory neuron was not due to a shift in the ratio of shared to unshared variance. Likewise, the general phenomenon of inhibitory and excitatory currents decorrelating each other is not the result of the 'fan-out' connectivity of inhibitory neurons, because the same phenomenon was present with independent and deterministic inhibition (**Figure 6**). Thus, feedforward inhibition can reduce the magnitude of both ρ_{input}, and output spiking ρ among excitatory neurons in a rate-independent fashion.

We reasoned that if interconnected excitatory/inhibitory neuron networks are subject to two effectively distinct types of extrinsic drive (Sachidhanandam et al., 2013; Middleton
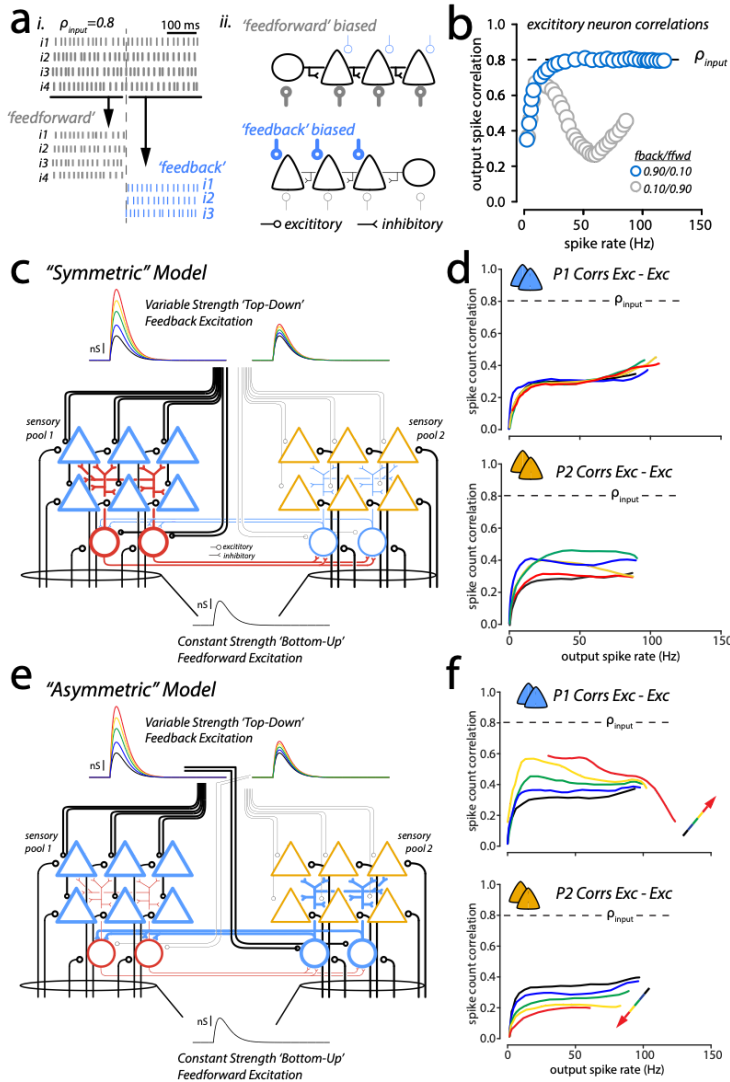
Figure 7. Network-level Modeling Show that Imbalanced Top-Down Feedback Can Create the Rate and Correlation Dynamics in Each Sub-Group that Predicted Perceptual Success (a) Model pools of synaptically-connected model excitatory and inhibitory neurons were subject to variable strength synaptic drive that had variable correlations in its inputs (similar to simulations in Figure 6). *i*, Modeled input spike trains were separated into "feedforward" (gray) and "feedback" (blue) by splitting the trains into two halves. Thus, feedforward inputs and feedback inputs would have the same statistics. ii, All neurons in a pool were eligible to receive "feedforward" inputs, but only the excitatory cells could receive "feedback" inputs. (b) Simulations were performed where the total excitation to the excitatory neurons varied in the proportion of feedforward and feedback contributions. *Blue dots* show the output spiking correlations as a function of spike rate when the feedback contributed 90% of the total excitation. *Gray dots* show the same, but for simulations where the 90% of the total excitation came from feedforward sources. The changes between the two graphs are primarily the result of differential recruitment of the inhibitory neuron in the pool. (c) The modeling approach in *a/b* was extended to pools of cortically inspired excitatory and inhibitory neurons. Two pools were modeled that each received equal strength "feedforward" excitatory inputs, but differed in the strength of feedback input they received. Pool 1 (*left*) is more sensitive to feedback inputs than Pool 2 (*right*). (d) Summary plot of spiking correlations among cells of Pool 1 (*top*) and Pool 2 (*bottom*). (e) Same as c, but instead of the two pools differing in the amount of feedback inputs they receive, the two pools differ in the relative sensitivity their excitatory and inhibitory neurons are to the feedback input ("asymmetric").

et al., 2012; Ecker et al., 2016), one akin to 'feedforward' sensory drive that recruits strong feedforward inhibition, and a second that recruits little to no inhibition on PYR (referred to here as 'feedback'), variations in these two inputs could create the distinct rate and correlation dynamics our imaging data showed in sensory pyramidal neuron groups. However, it should be noted that local network mechanisms can shape the nature of feedforward sensory excitation (Litwin-Kumar and Doiron, 2012) with behavioral consequences (Voigts et al., 2020). Thus, here, we use the

terms feedforward- and feedback-excitation as nomenclature whose aim is to maintain a distinction in the degree to which each excitation source recruits local inhibition.

To test this idea, we constructed a neural pool driven by a variable ratio of these 'feedforward' and 'feedback' sources of excitation (**Figure 7a, i**). Drive to the network was modeled as in preceding models, by generating spike trains with a constant mean rate, variance, and covariance. For each neuron, the spike train generated as its driver was split to create a feedforward portion and feedback portion ensuring equivalence of the input statistics. The only difference in the two drivers was that only feedforward input targeted inhibitory neurons. We then varied the ratio of feedforward and feedback contributions (**Figure 7a, ii**) while maintaining total excitatory conductance to the excitatory neurons. The resulting impact on excitatory neuron output rate and correlation for two different feedback/feedforward ratios is shown in **Figure 7b**. When feedforward drive dominated, rate and correlation increased together at low rates but soon dissociated, with correlations decreasing substantially as rates increased for much of the range. At high rates, the correlations among excitatory neurons began to increase again. In contrast, the feedback dominated example shows the simple predicted asymptotic relationship between rate and correlation, with correlation reaching a steady-state determined by ρ_{input}.

We next sought to determine if a network with only simple interruptions in symmetry (two types of pyramidal and inhibitory neurons) could produce the heterogeneous rate and correlation changes observed in our data. Based on the more elementary models

constructed (**Figures 6** and **7a**), simple changes in drive to one highly-interconnected, 'paired' E-I network would not produce the findings in our data, distinct rate and correlation changes in two different pools of pyramidal neurons. We therefore next applied feedback/feedforward inputs to two pools of excitatory neurons that showed similar feedforward connectivity/strength, but varied in their sensitivity to feedback projections. The full connectivity scheme and sizes of model pools examined are shown in **Figures 7c** and **7e**. Neuron groups are colored based on their sensitivity to excitatory feedback projections. The color scheme reflects our underlying hypothesis derived from the imaging studies, that is one group (*blue*) predicts detection with firing rate increases on top of their sensory driven rate (hit-predictive) because they are more sensitive to excitatory input, while the other pool (*amber*) is less sensitive to feedback, is more effectively balanced by inhibition, and will not show the simple asymptotic increase in correlation with rate. Testing the impact of independent levels of inhibition to the two pyramidal pools necessitated two pools of inhibitory interneurons, each wired to one pyramidal group. These interneuron pools were also interconnected, with stronger inhibitory strength between than within pools. See *Methods* for more details of model connectivity.

As in preceding simulations, we applied stepwise increases in feedforward *gExc* to drive neurons to different rates, but we also added feedback ("top-down") excitation that was not different statistically from the feedforward excitation. We tested two specific conditions that differed in the relative strength of feedback. In the first network tested, the strength of feedback drive for both the pyramidal and inhibitory neurons of pool 1

was higher than that of pool 2 (**Figure 7c**, rainbow colored conductance waveforms).
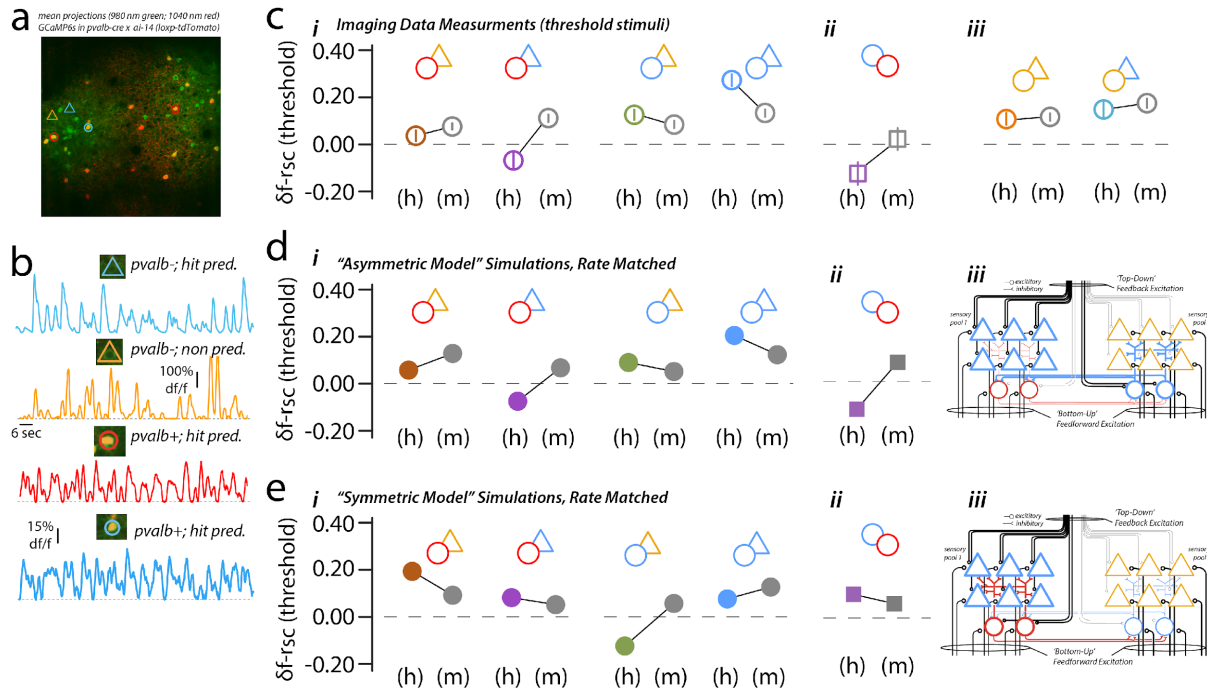

Figure 8. Simultaneous imaging of PV+ interneurons and PV- neurons reveal distinct correlations consistent with asymmetric, but not symmetric, model predictions. (a) Example montage images showing GCaMP6s (green) and tdTomato (red) expression from two different *pvalb*-cre mice bred to lsl-tdTomato reporter mice, and subsequently injected with a non cre-dependent GCaMP6s construct. (b) Example df/f traces from tdTomato(-) (*top* two traces with triangles) and tdTomato(+) neurons (*bottom* two traces with circles). Each example was a neuron scored as having either significantly hit-predicting DP (*blue*), non-significant DP dynamics (*orange*), or significantly miss-predicting DP (*red*). (c) i; Measured $\delta f\text{-}r_{sc}$ values between different pairings of PV+ and PV- neuron types on hit- (h; left) and miss-trials (m; right). Starting from left: pairs of miss-predictive PV+ neurons (red circles) and non-predictive PV- neurons (orange triangles), pairs of miss-predictive PV+ neurons (red circles) and hit-predictive PV- neurons, hit-predictive PV+ neurons (blue circles) and non-predictive PV- neurons (orange triangles), and hit-predictive PV+ neurons (blue circles) and hit-predictive PV- neurons (blue triangles). *ii*, Same as *i*, but for pairs of hit- (blue circles) and miss-predictive PV+ neurons (red circles). *iii*, Same as i and ii, but for pairs of non-predictive PV+ neurons (orange circles) and non-predictive PV- (left, orange triangles) and hit-predictive PV- (blue triangles). (d) Measured $\delta f\text{-}r_{sc}$ values were compared to spike count correlations derived from one of the two network models analyzed in *Figure 7* ("Asymmetric" or "Symmetric"). Here, the Asymmetric model is examined. *i-ii*, Computed correlation values based on the same conceptual groupings as *c*, but "hit-, miss- and non-predictive" correspond to the model neuron's higher, lower, or average sensitivity to feedback excitation relative to feedforward inhibition, respectively. And, PV+ (circles) are model inhibitory neurons, and PV- (triangles) are model excitatory neurons. *iii*, Shows the "asymmetric" model schematic from *Figure 7* examined here. (e) *i-iii*, Same as d, but for the "symmetric" model.

We termed this condition the "symmetric model" because the effects of feedback were similar within a pool, balanced input to excitatory and inhibitory targets. We computed output correlations between each pool's pyramidal cells as a function of output spiking, but varied the amount of feedback excitation proportionally as denoted by the different colors in **Figure 7d**. Despite increasing the total excitation to pool 1, output correlations

were unaffected. This effect emerged because as feedback increased, its effects on correlation were offset by proportionally increasing inhibition in a balanced fashion. Pool 2 was affected by the variations in feedback to pool 1, but the effects on correlation were mixed. For moderate increases in feedback correlations increased, but for stronger increases the increase was less pronounced. This effect resulted from variable disinhibitory effects from pool 1 inhibitory cells inhibiting those of pool 2. Overall, the symmetric model could not account for a rate-independent increase in correlation in some cells with a simultaneous decrease in others.

We also examined the effects of varying feedback across pools (**Figure 7e**). We termed this model the "asymmetric model" because the pyramidal cells of pool 1 and inhibitory cells of pool 2 were most sensitive to the feedback excitation, creating 'imbalanced' drive to excitatory and inhibitory targets. Increasing feedback in the asymmetric model led to rate-independent increases in output correlation among the pyramidal cells of pool 1, but also a decrease in correlations among pyramidal cells of pool 2. This result was due to feedback leading to a direct increase in excitation in pool 1, which alone will increase correlations, while pool 1 pyramidal cells' interneuron inputs was also progressively reduced, a removal of inhibition that should also increase correlations. For pool 2's pyramidal cells, increasing feedback excitation was balanced by increased feedback to their source of feedforward inhibition. The increased excitation in pool 2's inhibitory cells led to a progressive increase in inhibitory conductance in pool 2's pyramidal cells, in addition to driving increased inhibition in pool 1's inhibitory cells.

In sum, 'imbalanced' feedback input, preferring non-interconnected pools of excitatory and inhibitory cells, was able to capture the findings of our vSI and V1 imaging studies. This break in symmetry was sufficient to create all of the major subgroups of task-related cells observed in our data, across pyramidal and inhibitory circuits.

Model Driven Hypotheses Were Supported by Simultaneous Cell-type Specific Imaging

Using the successful asymmetric model architecture, we calculated pairwise interactions between all different subgroups observed in our imaging data, and tested whether parallel dynamics were found. To this end, we imaged PV-cre mice bred to ai14 lsl-tdTomato mice injected with non-flexed GCaMP6s (**Figure 8a**). This approach (Ringach et al., 2016) enabled simultaneous imaging of PV+ and non-PV+ neurons (n=3 animals; n=4 sessions). **Figure 8a** shows a montage image of the red and green imaging channels from a behavioral session. To determine the neurons expressing tdTomato (PV+), we first used GCaMP (*green*) imaging data to segment ROIs for analysis acquired with 980 nM excitation. Because strong green expression can 'bleed' into the red channel and cause false detection, the laser was also tuned to 1040 nM for acquisition of a small stack of images after each behavioral session. At 1040 nM, GCaMP absorption drops dramatically (Chen et al., 2013), whereas tdTomato absorption increases (Kerlin et al., 2010). We used red expression in the 1040 nM images to mark putative PV+ and differences between the 1040 and 980 images to confirm. **Figure 8b** shows example df/f traces during a behavioral session corresponding to the image in **Figure 8a**. In **Figure 8b,** the top two neurons were

tdTomato(-) and presumed pyramidal due to the baseline probability of observing this cell type and their high signal-to-noise ratio (SNR; Chen et al., 2013). The two example neurons below those are tdTomato(+) PV+ interneurons, that showed lower SNR, as expected (Chen et al., 2013; Ringach et al., 2016; Kerlin et al., 2010). Also noted in **Figure 8b** are hit-predicting pyramidal cells (*blue triangles*), non-predictive pyramidal neurons (*amber triangles*), miss-predicting PV+ neurons (*red circles*) and hit-predicting PV+ neurons (*blue circles*).

Figure 8c shows $\delta f\text{-}r_{sc}$ across groups of imaged hit-predicting and miss-predicting PV+ neurons for threshold hit- and miss-trials. **Figure 8c,i**, shows the relationship between hit- and miss-predicting PV+ and their hit- and non-predictive putative pyramidal cell (PV-) counterparts. Correlations between miss-predictive PV+ and non-predictive pyramidal neurons (n=62 pairs; *first* of the series) were small in magnitude and showed no strong relationship to detection outcome. Correlations between miss-predictive PV+ and hit-predictive pyramidal cells (*second* in the series) showed detection-dependent correlations with weakly negative correlations on hit-trials (-0.08 ± 0.04) and positive correlations (0.13 ± 0.02) on miss-trials. Hit-predictive PV+ showed detection-dependent correlation changes with non- and hit-predictive pyramidal (*third* and *fourth* in the series, respectively). For each, correlations were higher on hit trials, but the increases were most pronounced between hit-predictive PV+ and hit-predictive pyramidal. **Figure 8c,ii**, shows measured $\delta f\text{-}r_{sc}$ between pairs of miss- and hit-predictive PV+ neurons. On Miss trials, $\delta f\text{-}r_{sc}$ among pairs of miss-predictive PV+ and hit-predictive PV+ were small, but slightly positive (mean 0.01±0.02). On Hit trials $\delta f\text{-}r_{sc}$ was significantly negative (mean

-0.13±0.03; bootstrap difference test; p<0.0001), thus showing a significant decorrelation on Hit trials.

Figure 8c,*iii*, shows the results of computing δf-r_{sc} between non-predicting PV+ neurons and non-predictive pyramidal neurons (*first* in the series) and hit-predictive pyramidal neurons (*second* in the series). For both comparisons, there was little difference in the magnitudes of correlations and their differences on different outcome trial types. We did not model inhibitory neurons between pools that receive equal feedback or feedforward excitation. Based on our modeling assumptions, these neurons would correspond to "non-predictive" PV+ neurons. Further, based on our modeling assumptions, we would expect to see little to no outcome-dependent correlation changes between non-predictive PV+ neurons and either their non- or hit-predictive pyramidal neuron counterparts. We note that such a relationship could exist and would undermine the use of a simple two-pool model.

As a test of these model predictions, δf-r_{sc} was measured between 62 pairs of miss-predicting tdTomato(+) PV+, and hit-predictive tdTomato(-) putative pyramidal neurons (*second* in the series). On Miss trials, δf-r_{sc} between these subgroups was significantly positive, with a mean of 0.13 ± 0.02. On Hit trials, δf-r_{sc} between pairs was negative, with a mean of -0.08 ± 0.04. This outcome replicates the novel model prediction from the asymmetric feedback motif. **Figure 8d** shows the results of computing δf-r_{sc} for 62 pairs of miss-predicting tdTomato(+) PV+, and hit-predictive tdTomato(-) putative pyramidal neurons. On Miss trials, δf-r_{sc} between these subgroups

was significantly positive, with a mean of 0.13 ± 0.02. On Hit trials, δf-r_{sc} between pairs was negative, with a mean of -0.08 ± 0.04.

Figure 8d, and 8e show the correlations between the homologous modeled neuron pairs from simulations using the 'Asymmetric Model' (**Figure 8d**) and the 'Symmetric Model' (**Figure 8d**). For these comparisons 'hit-predictive' neurons are modeled as being more sensitive to feedback inhibition than 'non-predictive' neurons. Again, so-called 'miss-predictive' PV+ neurons were not explicitly modeled *a priori* , instead a key question of our network modeling of two pools of inhibitory cells (as in *Figure 7*) was whether differences in the sensitivity to feedback could give rise to a 'miss-predictive' inhibitory pool. Thus, for making comparisons between model cell-types and experimentally imaged outcome defined neurons, the homologue for "miss-predictive" PV+ neurons are the inhibitory cells of pool 1 (red) who primarily inhibit the excitatory neurons that are most sensitive to feedback. Results from the 'Asymmetric Model' (**Figure 8d**) qualitatively align with the experimentally determined results, whereas the qualitative relationships for the 'Symmetric Model' show significant differences, specifically negative correlations not observed experimentally between certain cell-type pairings, and weak correlations between hit-predictive (feedback biased) inhibitory and excitatory neurons.

Discussion

Here, we found a common motif, evident in SI and V1, that characterizes successful perceptual processing. In Layers 2/3 of both areas, two distinct subgroups of FS/PV emerged on successful trials that showed increases or decreases in evoked activity that predicted improved detection performance.   This inhibitory heterogeneity was accompanied by parallel emergence of a smaller pyramidal ensemble, that showed increased rate and correlation on Hit trials, while the majority of neurons showed no change in rate and decreased correlation.   A series of computational models demonstrated that imbalance in the drive to FS/PV subgroups, and in turn the inhibition generated to pyramidal populations, can explain the pyramidal ensemble formation observed.

Below, we discuss the possible origins of the observed FS/PV heterogeneity, how these findings inform views of optimal rate and correlation during active processing, and next step questions posed by the current results.

FS/PV Heterogeneity on Successful Trials

A canonical view of the role of FS/PV in sensory Neocortex is that they create excitatory/inhibitory balance and, therefore, a proportional and temporally-focused response to incoming perceptual stimuli (Simons and Carvell, 1989; Pinto et al., 2000; Wehr and Zador, 2003; Cruikshank et al., 2007; Xue et al., 2014; Chen et al., 2020). Such temporal limitations on feedforward sensory signals may be essential to constructing discrete representations that could support, for example, precise

associative learning (Froemke 2014). In contrast, inhibitory imbalance, evident in our data in multiple FS/PV subgroups with opposed task-predictive dynamics, may in contrast be essential to the preferential relay of information to enhance perceptual performance. Such imbalance was crucial in our model for creating the distinct pyramidal subgroup whose rate and correlation increases predict detection.

The view that 'E/I' balance is a crucial role for FS/PV in tactile processing was largely developed from detailed study of Layer 4 (Simons and Carvell, 1989; Cruikshank et al., 2007; Swadlow 2002), which receives the initial wave of feedforward lemniscal thalamocortical sensory input. Taken with these prior findings, the current data from Layers 2/3 suggest that the specific role of sensory responses amongst these FS/PV is distinct, consistent with other dissociations in the connectivity and dynamics of FS/PV between superficial and granular Layers (Xu et al., 2012).

Several intrinsic and extrinsic sources could generate the task-predictive FS/PV dynamics observed. In the model architecture developed, 'feedback' was invoked as the driver of asymmetric FS/PV behavior. Increased sensory-evoked SII activity predicts tactile detection success in many species (Kulics and Cauller and Kulics, 1991; de Lafuente et al., 2005; Moore et al., 2013), including in axons from SII recorded in mouse SI during vibrissa motion detection (Kwon et al., 2016). In contrast, as replicated here, only a relatively small subset of SI neurons show parallel firing increases on Hit trials (de Lafuente et al., 2005; Yang et al., 2016; Kwon et al., 2016). Given these prior findings and our model architecture, the role of SII inputs may be to depolarize SI

pyramidal neurons non-specifically, uniformly enhancing pyramidal threshold-level sensory responses on Hit trials (Yang et al., 2016; Kwon et al., 2016), and counterbalancing the increased hyperpolarization created by hit-predictive FS/PV. Such counterbalancing input would allow hit-predictive FS/PV to create inhibition-driven decorrelation across most neurons (Renart et al., 2010; Doiron et al., 2016) without driving a detectable change in their rate, as observed here. An alternative interpretation, also consistent with the successful model architecture, is that top-down feedback selectively targets hit-predictive FS/PV, or drives the appropriate disinhibitory circuit to do so (Zhang et al. 2014).

The distinct FS/PV subgroups observed on Hit trials could also emerge from neuromodulatory selectivity. Garcia-Junco-Clemente and colleagues (2019) showed that two distinct groups of FS/PV in frontal Neocortex are enhanced by norepinephrine or suppressed by acetylcholine, respectively. An increase in these neuromodulatory inputs during successful behavior could create the FS/PV subgroups we observed, presuming hit-predictive FS/PV are norepinephrine sensitive and miss-predictive cholinergic. This model-based prediction is consistent with studies showing cholinergic enhancement of visual task performance and decoupling of rate and r_{sc} in V1 (Pinto et al., 2013; Minces et al., 2017). If neuromodulatory drive creates these dynamics, the model framework explored here predicts either the emergence of sensitivity to specific neuromodulators among the FS/PV that gate task-appropriate relay neurons, or plasticity in the targeting of FS/PV that are sensitive to specific neuromodulators. Consistent with either prediction, visual and auditory perceptual learning can transform

FS/PV properties (Froemke 2014; Maor, 2020; Khan et al., 2018). Learning to associate an oriented visual stimulus with reward, and a distractor with non-reward, drives enhanced tuning selectivity of V1 FS/PV and a sharp decrease in correlations between FS/PV tuned for rewarded versus non-rewarded stimuli (Khan et al., 2018). The negative correlations observed here between the hit- and miss-predictive FS/PV subgroups is consistent with this result.

Further underscoring the importance of FS/PV heterogeneity for optimal neocortical processing are recent findings showing that activity in a subset of non-sensory responsive FS/PV predicts detection success (Shin and Moore, 2019). The regularity of firing in this group at 'gamma' inter-spike intervals (~25 milliseconds) predicted both detection success and increased pyramidal neuron firing rate (Shin and Moore, 2019). Optogenetic drive of FS/PV at gamma intervals, including sensory responsive and non-responsive cells, can also enhance detection success (Siegle et al., 2014), and phasic-modulation in fine timing of FS also predicts task success in attention-demanding paradigms (Yizhar et al, 2011; Kim et al., 2016). The present calcium imaging study lacked the temporal resolution to assess these fine time scales, but presumably these FS/PV dynamics contribute to the rate modulation and slower time-scale correlations observed.

Enhanced Rate and Correlation Dynamics in Distinct Pyramidal Ensembles

In this study, we measured rate and correlation changes that predict detection of weak sensory stimuli among large populations of identified cortical neurons. A full psychometric curve was obtained each session, allowing the identification of perceptual threshold, providing a standard benchmark across experiments. Further, targeting threshold-level stimuli for analysis was essential, as SI of rodents, monkeys and humans is necessary for successful detection of these hard-to-perceive tactile stimuli (LaMotte and Mountcastle, 1979; Cauller and Kulics, 1991; de Lafuente and Romo, 2005; Stüttgen and Schwarz, 2008; Yang et al., 2016; Kwon et al., 2016; Sachidhanandam et al., 2013; Yamashita and Petersen, 2016; Takahashi et al., 2016; Jones et al., 2007; Siegle et al., 2014). On threshold level hit trials, we found a reduction in spike count correlations ($\delta f\text{-}r_{sc}$) among sensory-responsive neurons with low DP. This result is consistent with several studies showing that the Neocortex is largely decorrelated during engaged sensory processing, broadly defined (Cohen and Maunsell, 2009; Mitchell et al., 2009; Renart et al., 2010; Middleton et al., 2012; Vinje and Gallant, 2000; Ecker et al., 2010). The present findings indicate that these decorrelations emerge from enhanced local inhibition mediated by hit-predictive FS/PV.

A subgroup of SI and V1 Layers 2/3 pyramidal neurons showed significant and high DP (Kwon et al., 2016). In contrast to the general sensory driven population, neurons with high DP also showed increased $\delta f\text{-}r_{sc}$ on Hit trials. Under the view that relay in Neocortex occurs through decoding of rate across the entire population, these high DP neurons would presumably be key, as they contribute the most additional spikes on a Hit trial. Under the view that relay relies on a specific 'ensemble' of cells that shows rate

and correlation enhancement on Hit trials, the significant and high DP neurons observed here presumably constitute this sub-group. As such, either interpreted from the perspective of information in the population as a whole (Shadlen and Newsome, 1998; Moreno-Bote et al., 2014; Renart et al., 2010; Doiron et al., 2016; Vinje and Gallant, 2000; Ecker et al., 2010), or in a framework in which selected ensembles encode information (Cauller and Kulics, 1991; Takahashi et al., 2016; Siegle et al., 2014; Womelsdorf et al., 2014; Wang and Buzsáki, 1996), the present findings indicate that enhanced correlations are not inherently punitive to detection behavior (Smith et al., 2011; Hashemi et al., 2018), but may be a necessary reflection of the inhibitory imbalance mechanisms driving local rate changes, or may be beneficial (Moreno-Bote et al., 2014; Goris et al., 2014; da Silveira and Berry, 2014). In support of this view, a prediction emerging from recent models is that increased correlations amongst the most sensitive neurons in a population should not impair read-out, while enhanced r_{sc} in less sensitive neurons (e.g., those with different peak tuning) will be negatively impactful (Moreno-Bote et al., 2014; Goris et al., 2014; da Silveira and Berry, 2014).

Consistent with the present findings, recent studies of selective attention targeting monkey higher neocortical areas have also reported heterogeneity in r_{sc}. In monkey SII, Gomez-Ramirez et al. (2014) showed that attention to a given feature predicts increased r_{sc} between neurons tuned to that tactile feature. In contrast, in monkey V4, Ruff and Cohen (2014) found that r_{sc} between neurons with similar spatial tuning was reduced when attention was directed to those receptive fields, while dissimilarly tuned cells showed higher r_{sc}. They interpreted these findings as supporting the conclusion

that shared noise in disparately tuned cells can be efficiently rejected by a downstream interpreter (Romo and Salinas, 2003). Whether downstream integration of correlation improves common mode rejection or, at the other extreme, whether correlations enhance successful information relay, our findings suggest that r_{sc} heterogeneity may be a consequence of the network mechanisms that also drive higher DP.

Our modeling results support the hypothesis that local variations in how excitation recruits inhibition leads to heterogeneity in the degree to which Layers 2/3 pyramidal neurons have behaviorally predictive changes in their sensory responsiveness. Specifically, we found that neurons with predictive rate changes should be subject to less inhibition whereas their non-predictive, but otherwise sensory responsive counterparts should be subject to more, and that a source of excitation that was distinct from sensory-driven feedforward-excitation could create this transient imbalance in local network inhibition. In Figures 7 and 8 we compare different model network connection schemes, and then used the favored scheme to examine correlation changes we had not yet tested. What typifies that model-derived hypothesis is that each neuron's pool of inhibitory neurons has vastly different sensitivities to non-feedforward sources of excitation. Our data shown in Figure 8 supports this hypothesis in that real data align well with model predictions, but it does not directly test it, nor do those analyses rule out other schemes. A large body of previous work have highlighted the diversity of excitatory and inhibitory neuron interactions that exist in neocortical networks (Gibson et al., 1999, Chen et al., 2017, Naka et al., 2018, Voigts et al., 2021). Further work has shown synaptic plasticity between excitatory and inhibitory neurons, as well as among

inhibitory neurons (House et al., 2011, Vogels et al., 2009; Vogels et al., 2013, Miska et al., 2018, Marchionni et al., 2022). Thus, the biological basis of such a seemingly specific connectivity scheme exists. However, further work will be needed to refine and directly test this proposed connectivity scheme.

Limitations of the Current Study

In the task employed here, subjects responded within a window after stimulus presentation for reward, building on the use of similar paradigms in sensory detection in monkey and rodent (de Lafuente et al., 2005; Carnevale et al., 2015; Stüttgen and Schwarz, 2008; Yang et al., 2016; Kwon et al., 2016; Sachidhanandam et al., 2013; Yamashita and Petersen, 2016; Takahashi et al., 2016). Unlike prior monkey studies, the current paradigm did not explicitly manipulate attention through directed cueing, nor did the task design dissociate criterion versus sensitivity shifts. To partly control for the level of task engagement, we rejected epochs in which the animal failed to detect maximal, readily perceived stimuli. This exclusion rule, which typically removed data from the end of behavioral sessions, substantially improved criterion and sensitivity measures. In area V4, rate increases and population-level r_{sc} decorrelation predict enhanced perceptual sensitivity following the allocation of attention, but not shifts in criterion (Luo and Maunsell, 2015). The transformations observed here in SI and V1 on Hit trials at threshold directly parallel these dynamics observed with sensitivity shifts in higher monkey visual Neocortex, and suggest they may emerge through similar mechanisms.

Imaging calcium indicators across a population of identified single neurons provides a high level of security in the definition of single neurons, and provides the large sample required to identify potentially rare response types (Kerlin et al., 2010). However, calcium imaging has a number of limitations. This approach lacks temporal precision to identify fast correlations (e.g. spike synchrony) that may also contribute to detection in SI (Shin and Moore, 2019; Siegle et al., 2014; Histed and Maunsell, 2014). Computing correlations with two-photon calcium imaging data can easily be confounded as well. If neurons are close to their saturation point, fluctuations in spiking will be obscured. We partly controlled for this factor by determining if there was a systematic relationship between baseline fluorescence intensity and detect probability: No relationship was observed in any sessions. These results suggest that our data were not systematically biased by variations in neuropil contamination, or correction methods that could lead to a common source of variability distorting correlation estimations. Other studies have shown a strong correspondence between r_{sc} computed from calcium imaging data with spiking measured intracellularly (Ko et al., 2011). Further, neurons with chance levels of DP showed a distance-dependent relationship in our data, as observed with electrophysiological and imaging methods that vary substantially in specific time-scales used to compute r_{sc} (Shadlen and Newsome, 1998; Cohen and Maunsell, 2009; Mitchell et al., 2009; Cohen and Kohn, 2011).

A direct implication of the present study is that an ensemble of cells with high DP and distinct correlation dynamics are particularly important to perception of threshold level

stimuli. In concept, the rate and/or correlation effects observed on Hit trials could enhance representation and information relay in Neocortex. Several kinds of subsequent studies can address these predictions. A systematic comparison of the efficacy of readout of SI or V1 signals using a variety of decoding approaches could provide insight into the import of the activity patterns observed (Carnevale et al., 2012; Carnevale et al., 2015). A balanced comparison of decoding approaches should include not only the large population of single neuron dynamics at a slower time scale provided here, but also the faster dynamics inaccessible to our two-photon imaging approach, including neural synchrony on <5 millisecond time scales (Siegle et al., 2014; Gomez-Ramirez et al., 2014). Another crucial next step is to compare the dynamics observed here with those obtained in discrimination, using two alternative forced choice designs, and with cued attention. These elaborations of the paradigm, and task designs allowing dissociation of criterion and sensitivity (Luo and Maunsell, 2015), will provide additional insights into the cognitive variables underlying the observed effects, and whether the distinct rate and correlation ensemble dynamics described here generalize in predicting perceptual success.

Chapter 4: Distinct behavioral dynamics in Layers II and III of mouse V1: predominance of parvalbumin cells with increased activity that predicts sensory detection

In Chapter 4 I demonstrate a first-authored research project that we will be submitting for publication. This Chapter elaborates on Chapter 3 by thoroughly investigating the Hit and Miss FS/PV cells that we discovered are predictive of behavioral outcome in the previous Chapter. We demonstrate that Layer II and III are functionally different in visual Neocortex. I conducted all of the experiments in Chapter 4 and worked closely with Dr. Christopher Deister and Dr. Christopher Moore on the logic and execution of this study and its corresponding analysis.

Abstract

In the previous Chapter, I describe new data supporting the existence of a fundamental 'motif' of Neocortical organization. Dual, opposed forms of task-dependent changes occur in two sub-groups of inhibitory interneurons. In one ('Hit' cells), increased firing on hit trials versus miss trials predicts successful performance of a detection task. In the other ('Miss' cells), decreased on hit trials versus miss trials firing predicts successful performance. Our formal computational modeling, which captures multiple subtle details of Primary Somatosensory and Visual Neocortical activity, indicates that Hit cells receive contextual input (e.g., of the type that might be an attentional control signal), and in turn inhibit Miss cells. Decreased Miss cell activity disinhibits those pyramidal neurons that they normally provide with feedforward inhibition, creating and amplifying sensory relay activity and perception.

In this Chapter, I show multiple forms of evidence that support the prediction that Hit cells are primary recipients of contextual information, and key controllers of optimal Neocortical dynamics. First, consistent with the general view that more superficial information in Neocortical Layers is more context sensitive, I have found Hit cells substantially outnumber Miss cells in Layer II, as compared to a Miss-biased distribution in Layer III. Further, while in our model Miss cells are the arbiter of sensory-driven, feedforward information onto the ensemble that carries the key task-dependent information, Hit cells do not inherently need to be stimulus responsive: their role in the model is to translate contextual information into disinhibition. In agreement, I discovered a larger population of non-sensory responsive Hit cells than non-sensory

responsive Miss cells, whereas Miss cells are nearly uniformly sensory responsive. These data, showing a predominance of Hit cells, particularly in Layer II close to the Neocortical surface, are also consistent with recent optogenetic studies showing the generic drive of PV enhances sensory detection, putatively through recruitment of these Hit cells (Siegle, Pritchett and Moore, 2014; Shin, H. PhD 2019).

In aggregate, these findings provide evidence for the predominance of Hit PV in supragranular Layers and support the suggestion that they are key to mediating contextual behavioral control signals. More generally, my findings reinforce the historical distinction between Layers II and III as independent processing domains that have distinct circuit properties and dynamics, a distinction typically ignored in current work. These results indicate that future studies should analyze potential differences between these Layers, leading to a more precise understanding of the functional circuitry underlying behavior.

Introduction

The structured, six-Layered Neocortex emerged with mammals, and has expanded with mammalian evolution (Allman, 1990; Kaas, 2006). Building on the existing and complex brain, it has added capacity for higher-dimensional and more flexible neural representations that optimize behavior based on prior learning (Rigotti et al., 2013; Siegel et al., 2015). As such, this structure is important for complex actions, cognition, and choice. Neocortical representations are also essential for perceptual performance, ranging from complex pattern recognition (Gross, 1992; Tsao and Livingstone, 2008) to

the added processing capacity necessary for the detection of threshold-level stimuli (Corkin, 1964; Siegle et al., 2014; Shin and Moore 2019).

The Neocortical role depends, at least in part, on the selective prioritization of signals depending on context (Maunsell and Treue, 2006; Moran and Desimone, 1985; Reynolds et al., 2000) that requires encoding of feedforward information (e.g. sensory afferent drive) and context dependent modulation (e.g. attending a feature). Primary Sensory Neocortex expresses both: in addition to its well-established encoding of sensory signals (Mountcastle et al., 1972; Hubel and Wiesel, 1962), primary sensory neurons have robust subthreshold substrates for rapid modulation (Borg-Graham et al., 1998; Moore and Nelson, 1998) and accordingly show many kinds of task-predictive information. For example, during detection of threshold signals, changes in baseline activity (e.g., oscillations) and immediate post-stimulus firing robustly predict task success (Moore et al., 2000; Jones et al., 2007; O'Connor et al., 2010; Siegle et al., 2014; Shin and Moore, 2019).

Interneurons, or local GABAergic cells, are widely regarded as key arbiters of Neocortical information flow (Innocenti, 1972; Cardin et al., 2009, Kim et al., 2016). The most common subtype in Neocortex are fast-spiking, Parvalbumin-positive interneurons (FS/PV) (Markram et al., 2004). These cells synapse on the soma to create somatic hyperpolarization (Rudy et al., 2011), a predominant source of rapid feedforward inhibition commonly observed in Primary Sensory Neocortex (Innocenti, 1972; Moore and Nelson, 1998; Cruikshank et al., 2007). Feedforward inhibition occurs when

information relay from an afferent (e.g., the lemniscal thalamus) contacts interconnected pairs of excitatory and FS interneurons, providing matched, or even exceptional, inhibition relative to the excitation arriving (e.g., Cruikshank et al., 2007). When E-I balance fails, this cortical state can lead to seizures and disorders of the Neocortex such as Autism (Medendorp et al., 2021, Chen et al., 2020).

Several lines of evidence also have suggested a role for increased FS/PV activity in enhancing signal flow during perceptual task performance in V1. Dan and colleagues showed that activation of FS/PV can enhance performance on Go/No-Go feature detection tasks (Lee et al., 2012). In SI, Shin and Moore (2019) found that increased evoked FS firing rates predict detection of vibrissal deflection in a similarly Go/No-Go task. Siegle, Pritchett, and Moore (2014) found that broad-scale optogenetic drive of PV-expressing neurons, which created both increased firing rates and synchronization of these cells, can also enhance sensory detection in this task. Shin and Moore more recently replicated these findings using an intersectional genetic approach that targeted expression to both PV and GAD expression cells in SI.

While the need for E-I balance, and prior results showing enhanced FS/PV can increase behavioral performance, suggest a role for increased FS/PV inhibition, the selective prioritization of signals from the periphery likely also requires disinhibition, to permit increased firing in pyramidal neurons that relay the preferred information. Vogels and Abbott (2009) captured this insight at a more abstract, logical level by showing that

models in which decreased inhibitory gain of specific input pathways allow focal imbalance and selective signal flow.

In direct agreement with the specific hypothesis that disinhibition is crucial to prioritized signal relay, we recently discovered that, in Primary Somatosensory and Visual Neocortex, FS/PV decrease in activity where there is successful detection. Using 2-photon imaging of genetically identified FS/PV, these FS/PV emerge into distinct ensembles predictive of successful perception. Specifically, a distinct subset showed greater sensory-evoked activity in response to successfully-detected sensory stimuli, referred to as "Hit" cells for ease of reference, and another subset decreased their firing on these trials ("Miss" cells) (Deister et al., 2023). This pattern is in contrast to pyramidal neurons, which only show significantly increased activity on detected trials (Deister et al., 2023).

Understanding these findings motivated the construction of a detailed computational model, shown in Figure 1a. This model architecture robustly captured the pairwise correlation structure and distinct rate and activity patterns found on Hit and Miss trials. The crux of this model is that FS/PV that receive stronger top-down input show greater activity on a Hit trial, and in turn inhibit Miss FS/PV that gate a distinct pyramidal ensemble. This pyramidal ensemble is, as per the disinhibition prediction, the small subgroup that shows enhanced firing on Hits. This motif is one in which predictive signals act through a subset of Hit interneurons to drive a cascade of downstream effects that enable relay of inhibition.

Findings showing a common motif of FS/PV inhibition across Neocortical areas, and the development of a detailed model that can capture their activity, pose several unanswered questions. The upper Neocortical Layers are typically associated with stronger contextual signals (Yamamori and Rockland, 2006; Hyvarinen, 1980). Hyvarinen et al., found that Layer II has more attention related signals and predictive cells than the deeper Layer III. This laminar analysis during tactile discrimination was one of the first to demonstrate the stronger effect of attention on Layer II vs. Layer III. This result suggests that Layers II FS/PV may receive stronger contextually-relevant modulation, corresponding to the Hit FS/PV in our model.

This distinction in the functional properties between Layer II and Layer III is also supported by more recent research that distinguishes between the canonical Layer II and III (Weiler et al., 2022, Meng et al., 2017). Prakash Kara and colleagues found an unexpected dependence of cortical depth in the visual system (O'Herron et al., 2020) and Simon Peron's group demonstrates additional functional distributions across Layers II/III in the somatosensory system (Voelcker et al., 2022). These studies in the mouse are some of the first to separate the canonical Layer II and III cortical layers, and even more evidence exists in the monkey, where the cytoarchitectural boundary between Layer II and Layer III is more concrete (Gur and Snodderly 2008). While our previous study combined Layers II/III as a computational unit, our current study separates these layers with the prediction that Layer II FS/PV receive stronger contextually-relevant modulation.

Additionally, our prior study focused only on sensory responsive FS/PV. However, other studies from our group (Shin and Moore, 2019) showed that ongoing activity in non-sensory responsive FS/PV is highly predictive of detection performance. Further, and more generally, context-dependent gating by FS/PV does not require that they are recruited by afferent incoming signals. In the basic intuition captured in our model, behaviorally-predictive firing - not a sensory response - is required in the distinct Hit and Miss FS/PV subgroups.

Here we systematically analyzed whether these crucial groups, Hit- or Miss-predictive FS/PV, show different responses in different layers and whether or not they had different sensory responsiveness. Using two-photon imaging of genetically identified FS/PV in primary visual Neocortex during a well-controlled visual detection task, the present study tested the possibility of differentiation in FS/PV dynamics during motivated behavior. Mice in our study were imaged each day of training to analyze emerging dynamics that may occur with sensory learning across the superficial lamina. Neocortical depths were also sampled each day spanning the range of Layer II and Layer III in the mouse, from 100 to 300 micrometers deep from the neocortical surface.

We have confirmed that, as shown previously, FS/PV show strong sensory responsiveness in the visual Neocortex (Andermann et al., 2011, Wilson et al., 2012). These findings were made in V1 during a visual contrast detection task. Additionally, we discover an uneven distribution of Hit and Miss cell ensembles across Layer II and Layer III. Results now indicate that the relative number and type of task-predictive

FS/PV differ across Layer II and Layer III of the sensory neocortical column. Further, this study demonstrates that Hit FS/PV cells are more likely to be non-stimulus driven than their Miss cell counterparts. This finding buttresses and adds to our imbalance model, in that the Hit cells are the ensemble receiving more top-down input. Miss cells are therefore more likely to be stimulus driven with balanced feedforward excitation. These non-responsive Hit cells are novel and support models of detection performance in the sensory neocortex.

Methods

Animals:

All experimental protocols were approved by the Institutional Animal Care and Use Committee at Brown University. Mice were housed on a 12-12 light/dark cycle and single housed with additional enrichment after surgical implantation. Male and female mice between the ages of 3 months and 5 months old were used for this study, and mice were balanced for sex. Behavioral testing and chronic imaging were conducted with 3 (2 male, 1 female) C57BL/6J mice (Jackson Laboratory).

Surgery:

Mice were surgically implanted at 8 weeks – 10 weeks of age. We implanted each mouse with a titanium headpost and cranial window for behavior testing and imaging. We also injected a virus into the neocortex. During the surgery, mice were anesthetized with 2% isoflurane and placed on a stereotactic frame (Kopf Instruments). The scalp was shaved, sterilized, and excised for the implantation of the headpost. To cement around the skull for head fixation, the skull was dried with Eye Spears (BVI), and a pocket was created by resecting muscle along the left and back portions of the skull.

The coordinates of the injection were then identified on the dorsal surface of the skull using a stereotaxic arm (Kopf Instruments) and marked with a pen. The headpost was then placed in position, and adhesive cement was applied to fix the headpost to the skull (C&B Metabond). Afterwards the cement could dry for 10 minutes. The craniotomy for the cranial window implant was initiated, first by shaving the skull to flatten the angle of the window. A pneumatic drill was used for shaving along with a carbide bit (NeoBurr FG4). The skull was irrigated with saline every two seconds of drilling to reduce heat. Once the skull was shaved, a second carbide bit (NeoBurr FG1/4) was used to drill the outline of a circular, 3 mm diameter craniotomy centered over V1. A tiny well of saline was made by filling the headpost well to cover the brain after the skull had been removed. Fine forceps were then used to remove the 3 mm piece of skull without damage to the dura.

Mice were injected using one of two viruses. For PV imaging, an AAV2/1-Syn-flex-GCaMP6s-WPRE-SV40 was used to label only FS/PV cells in the PV-cre mouse. For pan-neuronal imaging, an AAV2/1-Syn-GCaMP6s-WPRE-SV40 virus was used to label both cell populations. A micropipette was pulled for viral injections using a pipette puller (Sutter Instruments). A syringe pump (Stoelting) was used to load the virus into the pipette and infuse it into the brain. The center of V1 in the mouse was identified as 1.46 mm Anterior and 3.1 mm Lateral from the skull landmark lambda. Three sites centered on this V1 coordinate were then infected with virus for subsequent calcium indicator expression. Injections were made at a depth of 350 microns from the surface of the brain. 50 nl of virus was injected per site, at a rate of 10 nl/minute to ensure minimal tissue damage. The micropipette was left for five

minutes following each injection to prevent backflow. After the three injections, the cranial window was placed inside the craniotomy.

Cranial windows were made by placing 3 mm circular coverslips together surface to surface (Deckglaser, #0 Thickness). These coverslips were glued with optical adhesive and cured with a UV Light (Thor Labs). They were then glued to a third, 5 mm coverslip to make the outside portion of the window implant. Once the cranial window had been placed inside the craniotomy, a toothpick attached to a stereotactic arm was used to hold it in place. The window was then sealed using Metabond and left in place to dry. Once the surgery had been performed, the mouse was given 4 mg/kg of Meloxicam SR and monitored and weighed for the following three days.

Behavioral Paradigm:

A visual contrast detection task was designed to probe V1 function and neural dynamics mice.. Mice were placed on water restriction (1.2-1.5 mL water/day) for at least seven days before behavioral testing. Mice were imaged with a two-photon microscope during a go/no-go visual detection task. On the first and second day of training, all stimuli were rewarded to associate the stimulus with reward. Mice were then trained to report the detection of a visual stimulus with the lick of a reward spout connected to a capacitive center (Sparkfun). The correct detection of the tactile stimulus triggered a water droplet reward through a solenoid (McMaster-Carr). Mice generally performed 100-150 trials per day and were trained for 10 days of tactile detection. During behavioral testing, catch trials were presented to evaluate the false alarm rate. Catch trials were presented on 20% of trials, and mice received a time-out as punishment for false alarms.

Visual Stimulation:

The behavioral paradigm was built using a Teensy 3.6 microcontroller running Arduino software and Python. A small LED screen was used to deliver precisely controlled stimulation to the right eye during behavioral performance.

In Vivo Two-Photon Imaging:

Data were acquired using a two-photon microscope (Bruker/Prairie Technologies). An 8 kHz resonant galvanometer (CRS 8 Kz) was used for fast scanning in the x-axis, and a non-resonant galvanometer (Cambridge 6215) was used to increment in the y-axis. The imaging frame was 512 x 512 pixels and acquired at a frame rate of 30 Hz. Pixel size 0.96 um (Nikon 20x objective, x NA). A pre-chirped Ti-Sapphire laser (Spectra Physics, MaiTai was tuned to 960 nm to excited GCaMP6s, and was tuned to 1040 nm to excite tdTomato. Emitted photons were collected through the imaging path directed to a multialkali PMT (Hamamatsu, R3896) and were digitized with 14-bit resolution. Image acquisition was synchronized to behavioral control with TTL trigger pulses. A typical session lasted for 45 minutes to 1 hour. There was no indication of cellular damage or photobleaching over the training session or day-to-day.

Analyses:

Imaging Pre-Processing

Raw imaging data were recorded in Prairie View and moved from the imaging station for pre-processing. Raw data were converted to 16-bit tiff images stacks for each recording session (Image Block Ripping Utility). Pre-processing of the data was performed with custom written software by Dr. Christopher Deister (Image Analysis GUI, Github). Tiff

stacks were imported, and the first 6,000 frames were used to create a mean projection of the z-stack of data. Image stacks were then registered and corrected for motion. Images were then segmented using a cross-correlation algorithm. Each pixel's time course was identified, and its mean was subtracted. Then each surrounding pixel's time course was also calculated and mean-subtracted. Correlated regions were then identified by taking the cross correlation of the surrounding pixels. The resulting image was a binary mask of each cell's shape. Regions of interest (ROIs) corresponding to the area of each cell were then segmented. After each cell was identified, the mean pixel intensity of each ROI was calculated for each cell for each frame. The resulting time series was used to analyze calcium dynamics in single cells in the somatosensory Neocortex and visual Neocortex.

Fluorescent (F) time series data were analyzed with custom written software written in MATLAB. Time series data were first baselined by computing a ranked quantile cutoff. Data were baselined using the static baseline values in the computed quantile. Data were then normalized for dF/F by subtracting the baseline from the mean and dividing by the baseline.

Behavioral Analysis

Psychophysical analysis of the tactile detection task was conducted using MATLAB. Responses were characterized as hits or misses by analyzing the voltage of the capacitive lick sensor spout in the 1000 ms period following each stimulus time stamp. If a mouse licked to a stimulus, this was recorded as a hit, and if the mouse failed to lick to the stimulus, this was recorded as a miss. Additionally, catch trials or blanks were presented on 20% of trials to estimate the false alarm rate. False alarms were recorded

if the mouse licked on a catch trial, and correct rejections were recorded if a mouse refrained from licking on a catch trial.

To analyze Hit rate and false alarm rate an engagement threshold was set to ensure high performance of the mouse during the periods analyzed. Hit rate and false alarm rate were calculated by smoothing the Hit and Miss trial vector with a 100-window moving baseline. The skew of the Hit rate distribution was then calculated by subtracting the median of the Hit rate from the mean of the Hit rate. The bottom quartile of the distribution was calculated and the trials that contained the bottom quartile values were then identified. These trials were removed from the analysis, and the Hit rate and false alarm rates were then calculated from this new trial distribution after the engagement threshold.

D-prime (d') and criterion were also calculated and measures of the mouse's sensitivity and bias. D' was calculated as the normalized inverse of the Hit rate minus the normalized inverse of the false alarm rate. Criterion was calculated as one-half times the normalized inverse of the Hit rate plus the normalized inverse of the false alarm rate.

d' = norminv(Hit Rate)- norminv(FA Rate)

Criterion = norminv(Hit Rate)+norminv(FA Rate)

Histology:

Mice tested in the behavioral paradigm and chronic imaging preparation were sacrificed and perfused transcardially with 4% PFA. Mice were then decapitated, and the brain was removed and stored in PFA at 4°C for 36 hours. After PFA fixation the brain was then moved to a 30% sucrose solution and cryoprotected for another 36 hours. Mice brains were sectioned in 50-micron slices on a cryostat (Leica CM30505) and mounted on glass slides. An inverted fluorescent microscope (Zeiss Axiovert 200M) was used to identify virally infected, fluorescent regions. Regions of viral expression were compared to a brain atlas (Allen Mouse Brain Coronal Atlas) to confirm the location in the left primary visual Neocortex.

Results

We designed a visual contrast detection task (Meier and Reinagel, 2011; Montijn et al., 2015) to evaluate the relationship between task predictive FS/PV cell representation and behavior in a cohort of mice. This study was performed to evaluate certain features of our imbalance model, including the degree to which predictive cells vary by depth and their stimulus responsiveness (Figure 1a). Mice were trained to report the presence of a visual stimulus with a lick to a reward spout (Figure 1b). This psychophysical task rewarded the mouse for a correct identification of a stimulus, or Hit. Likewise, mice could Miss the stimulus and were unrewarded for that trial. We also delivered blank stimuli, or catch trials, to assay the animals' false alarm rates throughout the task. These blank stimuli were unrewarded and resulted in a time-out as a form of punishment if the animal licked to a blank stimulus (false alarm). Correct rejections improved d-prime behavioral sensitivity index during the task but were unrewarded.
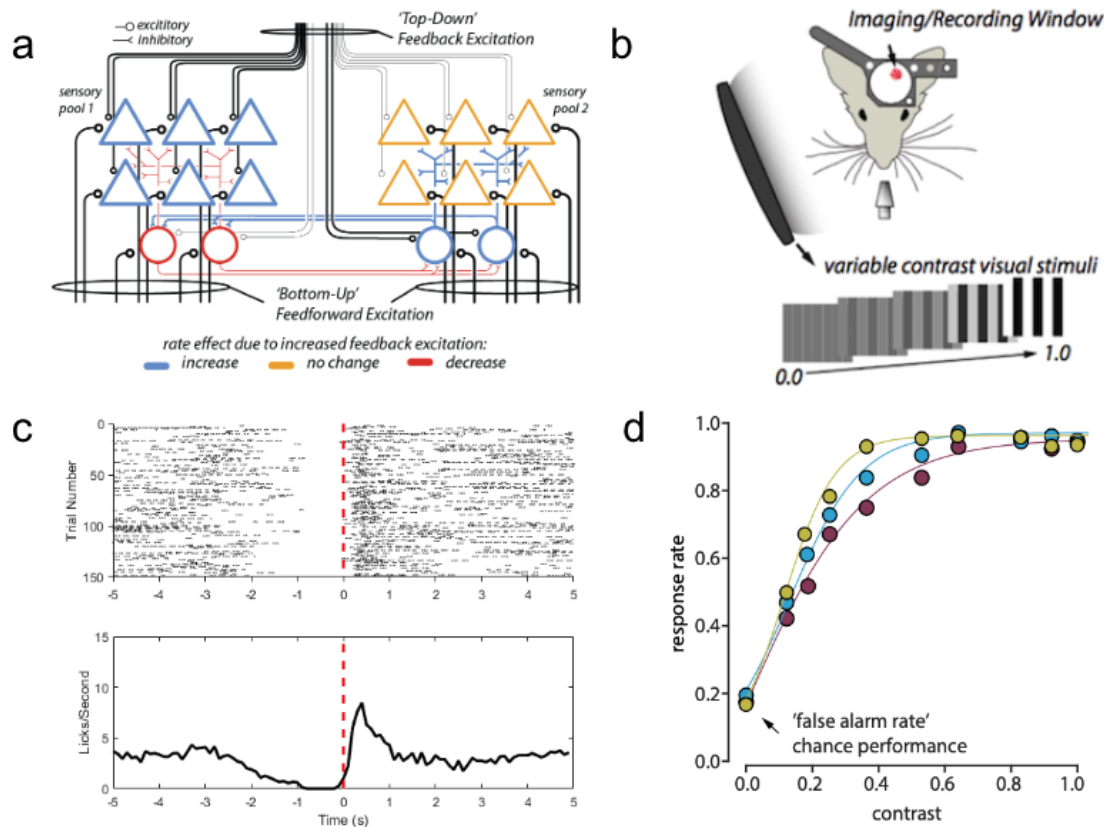
Figure 1. Inhibitory imbalance model revealed through a visual contrast detection task. (a) The inhibitory imbalance model is composed of four pools of cells, two inhibitory and two excitatory. Blue cells are ones that have been shown to increase their activity on successfully perceived trials and are labeled as "Hit" cells. Red cells are those that decrease their rates on successfully perceived trials and increase their rates on failed, or "Miss" trials. In the model, Hit cells are more contextually modified and receive more top-down input from higher cortical areas. Miss inhibitory PV cells are inhibited by Hit PV cells, thereby disinhibiting the Hit excitatory cells to open the gate for perceptually relevant signals to be relayed. (b) A schematic of the visual detection task in which mice receive visual stimulation while recording takes place in the contralateral visual Neocortex. (c) Raster plot showing licking rates of mice both pre-stimulus and post-stimulus. The dashed red line indicates the onset of the visual stimulus. Mice are trained for up to 150 trials per day. (d) Psychometric curves of 3 mice trained demonstrating their perceptual threshold and Hit rate at different stimulus intensities.

Mice performed more than 100 trials per day during training and task performance (Figure 1c). To achieve reward, mice were required to lick within 1-second of the stimulus presentation. This response produced a reward following 1.5 seconds post-stimulus. After the reward was consumed, a new trial would begin. Mice were required to withhold licking for a variable period of time (600 milliseconds to 3 seconds)

to induce a new stimulus presentation. Mice achieved strong behavioral performance

after training with low false alarm rates and nearly perfect performance on trials most

easy to perceive (Figure 1d). These trials with high-contrast helped the animal to learn

and stay engaged, but our functional analyses focused on data at the behavioral

threshold, defined as the stimulus contrast that is perceived half of the time.
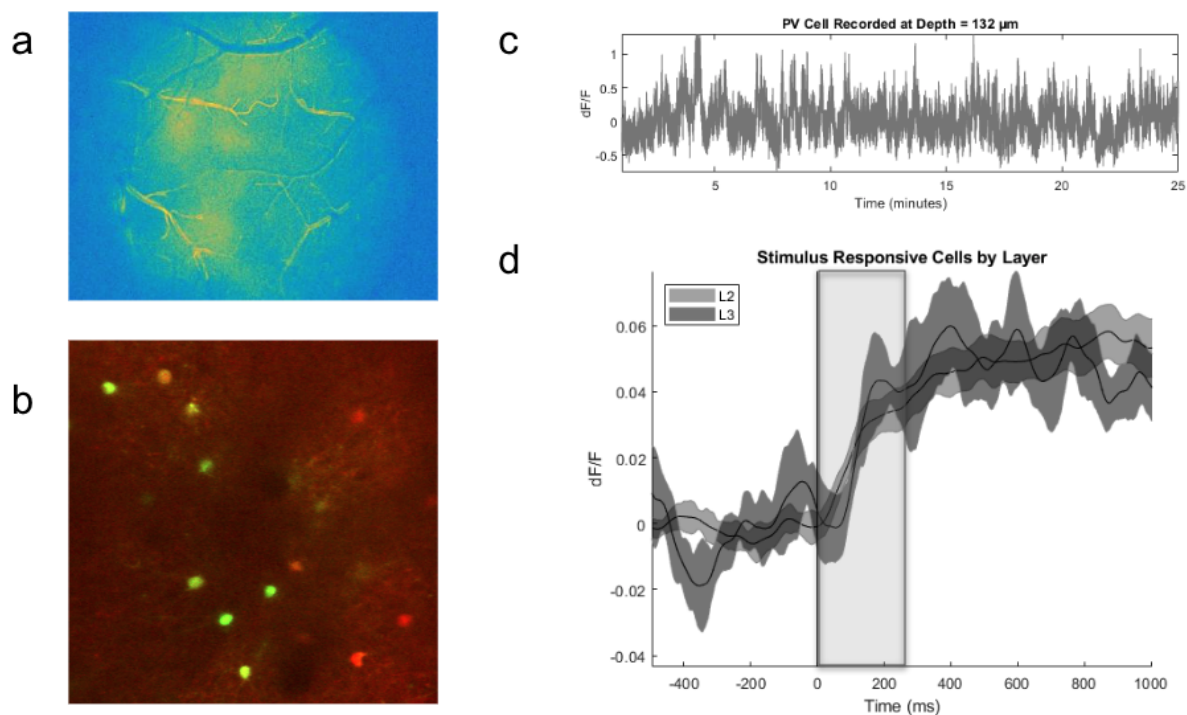

Figure 2. PV cell imaging and recording across Layers II and III of sensory neocortex. (a) Widefield imaging of GCaMP6s fluorescence labeling primary visual Neocortex (V1) in the mouse. A top-down view of the Neocortex through a chronically implanted cranial window. (b) Two-photon image of genetically-defined PV cells (red) virally infected with a calcium indicator, GCaMP6s (green). (c) A trace of a PV cell from Layer II recorded over twenty-five minutes. (d) Evoked activity of PV recorded from Layer II and Layer III. Mean evoked activity for PV recorded from Layer II and Layer III (n = 234 cells). The grey box represents the analysis period of evoked calcium activity.

We used two-photon microscopy to record genetically-identified PV during the visual

detection task. We confirmed our location of labeling in V1 through a number of

methods. First, anatomical landmarks including cerebral arteries were analyzed with

widefield imaging to corroborate our viral injection in V1 (Figure 2a). We also performed

histological identification of labeled cells in V1 after post-mortem tissue was collected

and sliced. Two-photon microscopy allowed us to record up to two-dozen PV cells at one time. Our average of PV cells per field of view (FOV) was 11 cells with a range of 5-22 cells recorded per imaging session (Figure 2b). FS/PV were recorded for dozens of minutes up to 1.5 hours during training, and showed the relatively lower signal-to-noise associated with these cells. An example of typical activity is shown in Figure 2c.
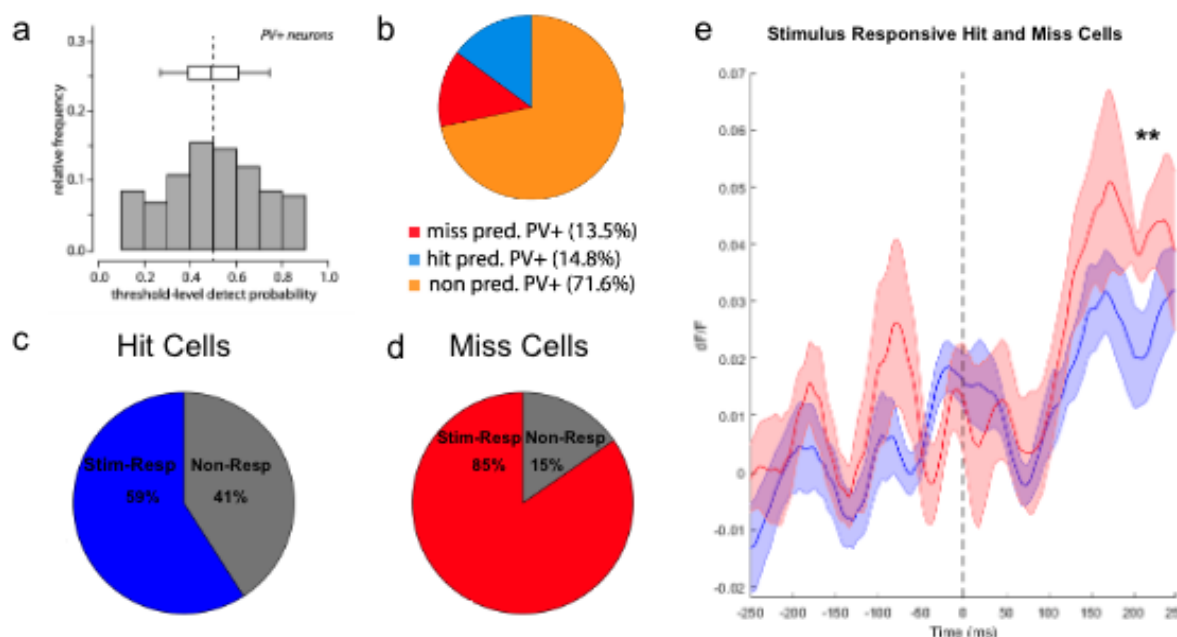

Figure 3. Hit and Miss FS/PV stimulus-responsiveness, stimulus-drive, and predictive nature. (a) Distribution of detect probability values of PV from Deister et al., 2023. Hit and Miss predictive PV have high DP values and low DP values, respectively. (b) Proportions of Hit, Miss, and non-predictive PV from a population of 224 collected PV. Hit and Miss stimulus-responsive PV are shown in roughly equal proportion. (c) Proportion of identified Hit PV that are stimulus-responsive (Stim-Resp) and non-stimulus-responsive (Non-Resp). Hit cells are less stimulus-driven than Miss cells. (d) The proportion of identified Miss cells that are stimulus-responsive. (e) Stimulus-evoked calcium activity of Hit (blue trace) and Miss (red trace) PV. Miss cells receive more drive.

We sampled across Layers II and III of the mouse visual Neocortex during our contrast detection task (Figure 2d). Functional differences between Layers II and III in the mouse have not been as extensively studied, although several studies demonstrate functional differences in the macaque. Our study evaluated the supragranular Layers

for functional differences amongst FS/PV, and we sampled FS/PV across distinct planes in Layers II and III (Figure 2d).

Based on our previous report that identified inhibitory imbalance in the somatosensory and visual cortices of the mouse (Deister et al., 2023), we identified cells that predicted Hit trials and Miss trials in their calcium activity during visual detection. Cells were identified as "Hit-predictive" or "Miss-predictive" based on their evoked activity in the post-stimulus window during behavioral performance. The cells that were Hit-predictive have increased evoked activity on Hit trials versus Miss trials, even with the same stimulus strength presentation. Miss-predictive cells had decreased activity on Hit trials compared to Miss trials, and increased their activity on Miss trials. Additionally, we implemented receiver-operating characteristic (ROC) analysis as a binary classification tool to classify cells as either Hit-predictive or Miss-predictive. The area under the ROC curve is the detect probability of a neuron when comparing the activity of the neuron on Hit trials and Miss trials (please see previous Chapter for further details of these analyses). Task-predictive PV were observed in most sessions (n = 18 sessions), and both Hit-predictive and Miss-predictive cells were observed in 4 sessions. We characterized these cells for each session and plotted their numbers and probabilities to visualize the number of predictive cells per session (Figure 3a and 3b). Hit cells were found to be 14.8% of stimulus-responsive PV, while Miss cells were seen in nearly equal proportion, 13.5% of stimulus-responsive PV.

Often, sensory neurophysiology studies focus exclusively on stimulus-responsive cells during neural analyses. However, task-predictive cells may, of course, include those that are not sensory responsive. Recent work from our laboratory (Shin and Moore, 2019), for example, has shown the existence of Fast-Spiking (putatively PV) interneurons in SI that predict detection task performance by their baseline rate, their adjusted synchrony and their gamma-band oscillatory behavior. Given the potentially important role of non-sensory FS/PV, we evaluated non-sensory responsive FS/PV. We found that 55.3% of PV cells were stimulus-responsive in the visual Neocortex. This finding is in agreement with a number of other studies of interneuron activity in the visual Neocortex, and with our parallel previous study of SI (Deister et al., 2023, Chapter 3).

Our computational model predicts that Hit cells translate contextual behavioral signals to create an optimal circuit condition for sensory relay. The Hit PV may, therefore, be behaviorally representative without necessarily being stimulus-driven. We determined that Hit cells were indeed more likely to be non-responsive to the stimulus (Figure 3c). Specifically, 59% of identified Hit cells were stimulus-responsive, while 85% of Miss cells were stimulus-responsive (Figure 3c and 3d). Further, when evaluating Hit cell and Miss cell evoked activity during high performance behavior, we determined that Miss cells were not only more likely to be sensory-responsive, but amongst sensory responsive PV from both groups, Miss also had greater evoked activity across trials to the visual stimulus (p = 3.01e-06; Figure 3e). Specifically, we found that Miss cells had increased activity at 225 ms post-stimulus, a time-point after the rise time of GCaMP6s,

a slower calcium indicator. This finding is consistent with the view that Miss cells

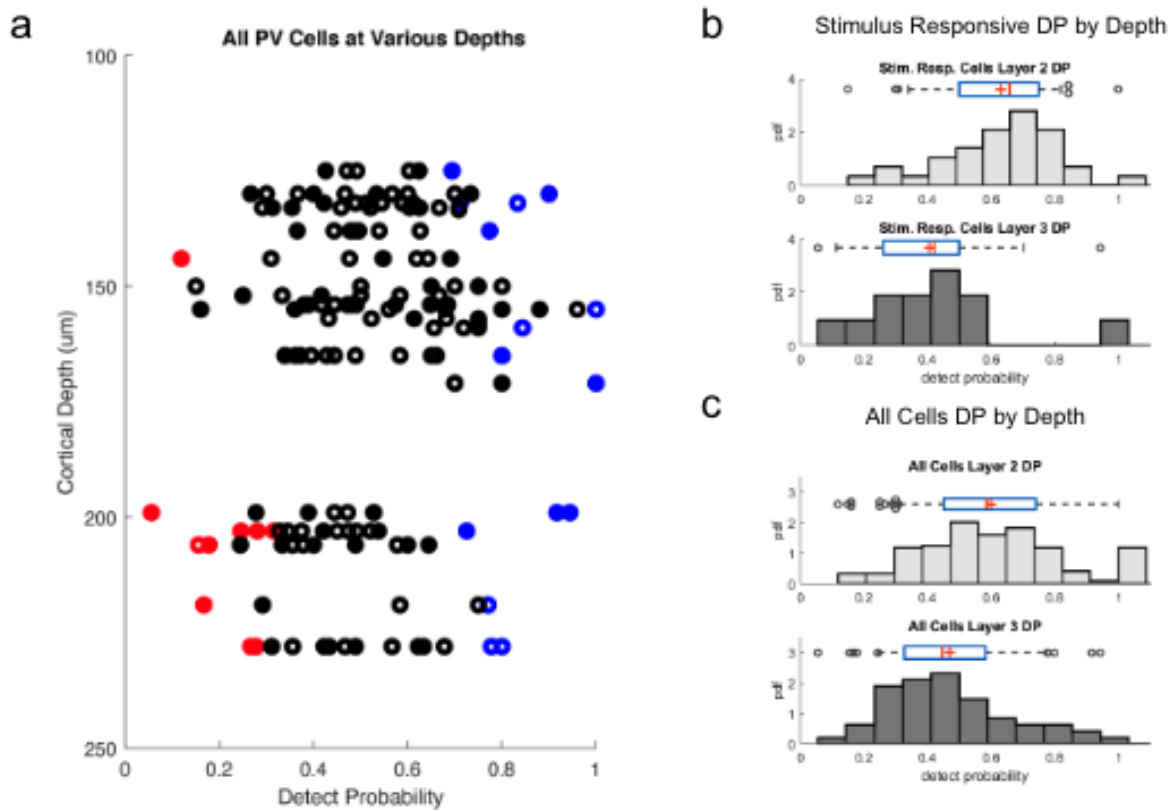receive greater feed-forward input from sensory thalamus.

Figure 4: Detect probabilities across Layers II/III of visual Neocortex. (a) Scatter plot of detection probabilities of identified PV across Layers II and III of V1. The y-axis has been inverted to represent the depth of the neocortex from the pial surface. Filled circles represent stimulus-responsive PV. (b) Histogram of the detect probability values of stimulus-responsive cells in Layer II and Layer III. DP values in Layer III are skewed toward Miss predictivity. (c) Histogram of the detect probability values of all identified PV in Layer II and Layer III. Detect probability values of all cells in Layer III are still skewed toward Miss predictivity.

Layers II and III of the sensory Neocortex have often been combined as a single

computational unit, although anatomical differences do exist between the supragranular

Layers. We characterized the behavioral representation of both stimulus-responsive

FS/PV and all FS/PV to determine if a functional difference exists between Layers II and

III FS/PV behavioral dynamics. We found that Hit FS/PV were more common in Layer II

than Miss cells (10 versus 1, respectively) and that the overall distribution was shifted to

Hit DP when considering only stimulus responsive PV (Mean 0.629 ± 0.17; Figure 4b) or

all PV (Mean 0.599 ± 0.21; Figure 4c). In sharp contrast, Layer III showed a greater

number of Miss than Hit PV (9 versus 6, respectively), and an overall shift to

Miss-predictive behavior when sensory responsive (Mean 0.407 ± 0.22; Figure 4b) and

all PV were considered (Mean 0.469 ± 0.20; Figure 4c). Between Layers, a bootstrap

statistical analysis showed these differences were significant for stimulus-responsive PV (p = 4.12e-06), and all PV (p = 8.57e-05).

As shown above in Chapter 3, the shared spike-count correlations (often referred to as 'noise correlations') can be robustly differentiated between functionally defined sub-groups. As shown in Figure 8 of that

Figure 5. Noise correlations between pairs of predictive cells (a) Noise correlations between paris of Hit cells during visual contrast detection. Trial-by-trial fluctuations between activity in Hit cells show weakly positive noise correlations. (b) Noise correlations between pairs of Miss cells recorded in the same field of view. Miss cell correlations are also weakly positive. (c) Noise correlations between Hit and Miss cells from pairs identified in the same field of view. These pairs demonstrate examples of anti-correlation amongst PV, which is rare and supports the imbalance model.

Chapter, only one sub-group comparison—that between Hit and Miss PV in SI—showed

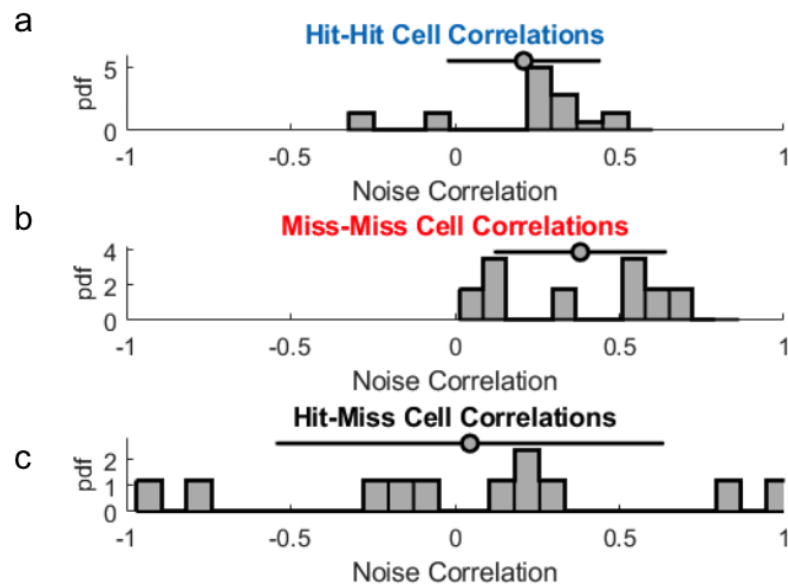negative spike-count correlations, a rare property that, in our computational modeling,

emerges from reciprocal inhibitory connections.   Interestingly, in a more limited sample, we replicated this result in our study of V1. Hit-Hit pairs and Miss-Miss pairs had, on average, weekly positive correlations in V1 (Figure 5a and 5b), as shown above for SI also.   In support of a conclusion of inhibitory relationships amongst predictive cells, most importantly that Hit PV are positioned to inhibit Miss PV, almost all pairs with negative correlations were observed amongst Hit-Miss pairs (Figure 5c).

Discussion

We investigated the laminar distribution of behaviorally representative and predictive FS/PV in awake behaving mice during a visual contrast detection task, and found that Miss cells reside deeper within Layer II and III. Hit cells were more superficial but also resided within Layer III. We also tested the degree to which predictive FS/PV were stimulus responsive or unresponsive. Systems neuroscience research generally focuses on responsive cells, but previous evidence led us to believe a cell could predict the behavioral outcome of a trial without necessarily responding to the stimulus. These two findings, when taken together, support and add to our inhibitory imbalance model. Hit cells located in Layer II receive more top-down activity than the Miss cells in Layer III, which are more stimulus-driven in agreement with their closer proximity to Layer IV.

Laminar Distribution of Hit and Miss Cells
A major focus of our study was to address the laminar distribution of Hit and Miss cells within Layer II and III of sensory neocortex. We not only identified Hit and Miss cells within Layer II and III as in our previous study, but also found Miss cells residing within

Layer III and almost absent in Layer II. Hit cells were both superficial and deeper within

Layer II and Layer III. Our study sought to corroborate and add to recent literature that

Layer II and Layer III are functionally distinct in mouse sensory Neocortex. The

canonical view based on anatomical evidence is that mouse Layers II/III are a single

computational unit or model, but our study challenges that notion with behaviorally

representative cells residing differently within the superficial Layers. This research not

only buttresses and improves our inhibitory imbalance model, but it can also add to

models of sensory Neocortex that have a laminar-specific focus and laminar terms.

Consistent with our previous findings, recent studies of mouse Layers II/III also find

gradients across these superficial Layers (O'Herron et al., 2020, Meng et al., 2017,

Voelcker et al., 2022).

Stimulus-Responsiveness of Hit and Miss Cells

Here, we not only confirmed our inhibitory imbalance motif (Deister et al., 2023) but also

added to the model with data that demonstrate Hit FS/PV receiving less-stimulus driven

activity and more top-down activity. Layer II is known to receive more signals from

higher-order cortical areas because of its proximity to Layer I. We recorded all cells and

used ROC analysis even on cells that weren't stimulus-responsive. We found that Hit

FS/PV could predict Hit trials in their activity without having stimulus-evoked activity.

Counter to this, Miss FS/PV that were recorded were nearly all-stimulus responsive.

We hypothesize that these Miss FS/PV that reside deeper in Layer III and are mostly

stimulus-responsive may be a downstream target of feed-forward inhibition in Layer IV.

The Miss FS/PV are closest to Layer IV due to their location in Layer III. Further studies

can test this notion with whole cell recordings, biocytin labeling, and *in vitro* slice physiology.

Limitations of The Current Study

Our present study recorded FS/PV across Layers II and III of the visual Neocortex. We used calcium imaging to label FS/PV cells with GCaMP6s and recorded populations of FS/PV cells throughout the superficial lamina of visual Neocortex. Due to the fact that interneurons are roughly 20% of neurons in the sensory Neocortex and that FS/PV cells are roughly 40% of all interneurons, the number of cells we recorded in a field of view was low. With the number of PV that are predictive being in the range of 30% of FS/PV in vision, we were limited in the number of predictive FS/PV we recorded in a session. Sessions contained either no predictive cells, a Miss cell, a Hit Cell, or rarely combinations of both. This led us to have a low sample for correlations amongst Hit and Miss cells.

Additionally, the calcium imaging that we used to record genetically-identified FS/PV populations is a slower method of recording, with the GCaMP6s signal known to rise on the order of 200 ms. Our sampling at 30 Hz did not allow for faster timescale information like neural synchrony and action potential firing. Recordings with electrophysiology would provide this information that our lab has previously shown to predict perception (Siegle et al., 2014, Shin et al., 2019).

Finally, our study did not contain any causal manipulations of Hit and Miss Cells during detection performance. FS/PV cells were recorded over several sessions and were correlated with the behavioral outcome. Hit and Miss cells emerged during task performance but were never directly stimulated. Two causal manipulations would add to this study in the future. First, stimulation of Layer II PV versus Layer III PV would provide insight into laminar function, with the prediction that Layer III stimulation would suppress behavior because of the overwhelming proportion of Miss cells. Additionally, Hit and Miss cells could be targeted singly, or in groups, to manipulate behavior based on the cell type stimulated. Our lab recently developed a photoswitchable Bioluminescent- Optogenetic method that can allow for planar stimulation or select ensemble manipulation. Employing this method in the future would further support our model and demonstrate the degree to which the Hit and Miss cells are crucial in the visual cortical column.

References

Abbott, L. F. (2008). Theoretical neuroscience rising. *Neuron*, *60*(3), 489–495. https://doi.org/10.1016/j.neuron.2008.10.019

Agetsuma, M., Hamm, J. P., Tao, K., Fujisawa, S., & Yuste, R. (2017). Parvalbumin-positive interneurons regulate neuronal ensembles in visual cortex. *Cerebral Cortex*, *28*(5), 1831–1845. https://doi.org/10.1093/cercor/bhx169

Alitto, H. J., & Dan, Y. (2010). Function of inhibition in visual cortical processing. *Current Opinion in Neurobiology*, *20*(3), 340–346. https://doi.org/10.1016/j.conb.2010.02.012

Allman, J. (1990). Evolution of Neocortex. *Comparative Structure and Evolution of Cerebral Cortex, Part I*, 269–283. https://doi.org/10.1007/978-1-4757-9622-3_7

Armstrong-James, M., Diamond, M. E., & Ebner, F. F. (1994). An innocuous bias in whisker use in adult rats modifies receptive fields of barrel cortex neurons. *The Journal of Neuroscience*, *14*(11), 6978–6991. https://doi.org/10.1523/jneurosci.14-11-06978.1994

Atallah, B. V., Bruns, W., Carandini, M., & Scanziani, M. (2012). Parvalbumin-expressing interneurons linearly transform cortical responses to visual stimuli. *Neuron*, *73*(1), 159–170. https://doi.org/10.1016/j.neuron.2011.12.013

Azouz, R., & Gray, C. M. (2003). Adaptive coincidence detection and dynamic gain control in visual cortical neurons in vivo. *Neuron*, *37*(3), 513–523. https://doi.org/10.1016/s0896-6273(02)01186-8

Berglund, K., Birkner, E., Augustine, G. J., & Hochgeschwender, U. (2013). Light-emitting channelrhodopsins for combined optogenetic and chemical-genetic control of neurons. *PLoS ONE*, 8, e59759. https://doi.org/10.1371/journ al.pone.0059759

Berglund, K., Birkner, E., Augustine, G. J., & Hochgeschwender, U. (2013). Light-emitting channelrhodopsins for combined optogenetic and chemical-genetic control of neurons. *PLoS ONE*, *8*(3). https://doi.org/10.1371/journal.pone.0059759

Berglund, K., Clissold, K., Li, H. E., Wen, L., Park, S. Y., Gleixner, J., Klein, M. E., Lu, D., Barter, J. W., Rossi, M. A., Augustine, G. J., Yin, H. H., & Hochgeschwender,

U. (2016). Luminopsins integrate opto- and Chemogenetics by using physical and biological light sources for opsin activation. *Proceedings of the National Academy of Sciences*, *113*(3). https://doi.org/10.1073/pnas.1510899113

Berglund, K., Clissold, K., Li, H. E., Wen, L., Park, S. Y., Gleixner, J., Klein, M.E., Lu, D., Barter, J.W., Rossi, M.A., Augustine, G.J., Yin, H.H., Hochgeschwender, U. (2016). Luminopsins integrate opto- and chemogenetics by using physical and biological light sources for opsin activation. *Proceedings of the National Academy of Sciences of the United States of America*, 113, E358–E367. https://doi.org/10.1073/pnas.15108 99113

Berglund, K., Fernandez, A. M., Gutekunst, C. N., Hochgeschwender, U., & Gross, R. E. (2019). Step‑function luminopsins for bimodal prolonged neuromodulation. *Journal of Neuroscience Research*, 98(3), 422–436. https://doi.org/10.1002/jnr.24424

Berglund, K., Tung, J. K., Higashikubo, B., Gross, R. E., Moore, C. I., & Hochgeschwender, U. (2016). Combined optogenetic and chemogenetic control of neurons. *Methods in Molecular Biology*, 1408,207–225.

Birkner, E., Berglund, K., Klein, M. E., Augustine, G. J., & Hochgeschwender, U. (2014). Non‑invasive activation of optogenetic actuators. *Proceedings of SPIE—International Society for Optical Engineering*, 8928, 89282F-1–89282F-9.

Borg-Graham, L. J., Monier, C., & Frégnac, Y. (1998). Visual input evokes transient and strong shunting inhibition in visual cortical neurons. *Nature*, *393*(6683), 369–373. https://doi.org/10.1038/30735

Bortone, D. S., Olsen, S. R., & Scanziani, M. (2014). Translaminar inhibitory cells recruited by layer 6 corticothalamic neurons suppress visual cortex. *Neuron*, *82*(2), 474–485. https://doi.org/10.1016/j.neuron.2014.02.021

Boyden, E. S., Zhang, F., Bamberg, E., Nagel, G., & Deisseroth, K. (2005). Millisecond‑timescale, genetically targeted optical control of neural activity. *Nature Neuroscience*, 8, 1263–1268. https://doi.org/10.1038/nn1525

Brodmann, K. (1909). *Vergleichende Lokalisationslehre der Grosshirnrinde in Ihren Prinzipien dargestellt auf Grund des Zellenbaues*. Barth.

Callaway, E. M. (1998). Local circuits in primary visual cortex of the macaque monkey. *Annual Review of Neuroscience*, *21*(1), 47–74. https://doi.org/10.1146/annurev.neuro.21.1.47

Carandini, M., & Churchland, A. K. (2013). Probing perceptual decisions in rodents. *Nature Neuroscience*, *16*(7), 824–831. https://doi.org/10.1038/nn.3410

Cardin, J. A., Carlén, M., Meletis, K., Knoblich, U., Zhang, F., Deisseroth, K., Tsai, L.-H., & Moore, C. I. (2009). Driving fast-spiking cells induces gamma rhythm and controls sensory responses. *Nature*, *459*(7247), 663–667. https://doi.org/10.1038/nature08002

Carnevale, F., de Lafuente, V., Romo, R., & Parga, N. (2012). Internal signal correlates neural populations and biases perceptual decision reports. *Proceedings of the National Academy of Sciences*, *109*(46), 18938–18943. https://doi.org/10.1073/pnas.1216799109

Carrillo-Reid, L., Han, S., Yang, W., Akrouh, A., & Yuste, R. (2019). Controlling visually guided behavior by holographic recalling of cortical ensembles. *Cell*, *178*(2). https://doi.org/10.1016/j.cell.2019.05.045

Cauller, L. J., & Kulics, A. T. (1991). The neural basis of the behaviorally relevant N1 component of the somatosensory-evoked potential in SI cortex of awake monkeys: Evidence that backward cortical projections signal conscious touch sensation. *Experimental Brain Research*, *84*(3). https://doi.org/10.1007/bf00230973

Chen, G., Zhang, Y., Li, X., Zhao, X., Ye, Q., Lin, Y., Tao, H. W., Rasch, M. J., & Zhang, X. (2017). Distinct inhibitory circuits orchestrate cortical beta and gamma band oscillations. *Neuron*, *96*(6). https://doi.org/10.1016/j.neuron.2017.11.033

Chen, Q., Deister, C. A., Gao, X., Guo, B., Lynn-Jones, T., Chen, N., Wells, M. F., Liu, R., Goard, M. J., Dimidschstein, J., Feng, S., Shi, Y., Liao, W., Lu, Z., Fishell, G., Moore, C. I., & Feng, G. (2020). Dysfunction of cortical GABAergic neurons leads to sensory hyper-reactivity in a Shank3 mouse model of ASD. *Nature Neuroscience*, *23*(4), 520–532. https://doi.org/10.1038/s41593-020-0598-6

Chen, T.-W., Wardill, T. J., Sun, Y., Pulver, S. R., Renninger, S. L., Baohan, A., Schreiter, E. R., Kerr, R. A., Orger, M. B., Jayaraman, V., Looger, L. L., Svoboda, K., & Kim, D. S. (2013). Ultrasensitive fluorescent proteins for imaging neuronal activity. *Nature*, *499*(7458), 295–300. https://doi.org/10.1038/nature12354

Chirico, G., Cannone, F., Baldini, G., & Diaspro, A. (2003). Two‑photon thermal bleaching of single fluorescent molecules. *Biophysical Journal*, *84*, 588–598. https://doi.org/10.1016/S0006-3495(03)74879-6

Chou, W. C., Liao, K. W., Lo, Y. C., Jiang, S. Y., Yeh, M. Y., & Roffler, S.R. (1999). Expression of chimeric monomer and dimer proteins on the plasma membrane of mammalian cells. *Biotechnology and Bioengineering*, 65, 160–169. https://doi.org/10.1002/(SICI)1097-0290(19991 020)65:2<160:AID-BIT5>3.0.CO;2-U

Cohen, M. R., & Kohn, A. (2011). Measuring and interpreting neuronal correlations. *Nature Neuroscience*, *14*(7), 811–819. https://doi.org/10.1038/nn.2842

Cohen, M. R., & Maunsell, J. H. (2009). Attention improves performance primarily by reducing interneuronal correlations. *Nature Neuroscience*, *12*(12), 1594–1600. https://doi.org/10.1038/nn.2439

Cone, J. J., Scantlen, M. D., Histed, M. H., & Maunsell, J. H. R. (2018). Different inhibitory interneuron cell classes make distinct contributions to visual perception. https://doi.org/10.1101/275172

Cook, E. P., & Maunsell, J. H. (2002). Dynamics of neuronal responses in macaque MT and VIP during motion detection. *Nature Neuroscience*, *5*(10), 985–994. https://doi.org/10.1038/nn924

Crochet, S., Poulet, J. F. A., Kremer, Y., & Petersen, C. C. H. (2011). Synaptic mechanisms underlying sparse coding of active touch. *Neuron*, *70*(1), 170. https://doi.org/10.1016/j.neuron.2011.03.017

Cruikshank, S. J., Lewis, T. J., & Connors, B. W. (2007). Synaptic basis for intense thalamocortical activation of feedforward inhibitory cells in neocortex. *Nature Neuroscience*, *10*(4), 462–468. https://doi.org/10.1038/nn1861

da Silveira, R. A., & Berry, M. J. (2014). High-fidelity coding with correlated neurons. *PLoS Computational Biology*, *10*(11). https://doi.org/10.1371/journal.pcbi.1003970

Deister, C. A., More, A. I., Voigts, J., Becheck S., Lichtin, R., Brown, T. C., Moore, C. I. (2023). Neocortical inhibitory imbalance predicts successful sensory detection. *In submission.*

de Lafuente, V., & Romo, R. (2005). Neuronal correlates of subjective sensory experience. *Nature Neuroscience*, *8*(12), 1698–1703. https://doi.org/10.1038/nn1587

de la Rocha, J., Doiron, B., Shea-Brown, E., Josić, K., & Reyes, A. (2007). Correlation between neural spike trains increases with firing rate. *Nature*, *448*(7155), 802–806. https://doi.org/10.1038/nature06028

Denk, W., Strickler, J. H., & Webb, W. W. (1990). Two-photon laser scanning fluorescence microscopy. *Science*, *248*(4951), 73–76. https://doi.org/10.1126/science.2321027

Denk, W., & Svoboda, K. (1997). Photon upmanship: Why multiphoton imaging is more than a gimmick. *Neuron,* 18, 351–357. https://doi.org/10.1016/S0896-6273(00)81237-4

Doiron, B., Litwin-Kumar, A., Rosenbaum, R., Ocker, G. K., & Josić, K. (2016). The mechanics of state-dependent neural correlations. *Nature Neuroscience*, *19*(3), 383–393. https://doi.org/10.1038/nn.4242

Doron, G., von Heimendahl, M., Schlattmann, P., Houweling, A. R., & Brecht, M. (2014). Spiking irregularity and frequency modulate the behavioral report of single-neuron stimulation. *Neuron*, *81*(3), 653–663. https://doi.org/10.1016/j.neuron.2013.11.032

Ecker, A. S., Berens, P., Keliris, G. A., Bethge, M., Logothetis, N. K., & Tolias, A. S. (2010). Decorrelated neuronal firing in cortical microcircuits. *Science*, *327*(5965), 584–587. https://doi.org/10.1126/science.1179867

Ecker, A. S., Denfield, G. H., Bethge, M., & Tolias, A. S. (2015). On the structure of population activity under fluctuations in attentional state. https://doi.org/10.1101/018226

Fagiolini, M., Fritschy, J.-M., Löw Karin, Möhler Hanns, Rudolph, U., & Hensch, T. K. (2004). Specific GABA a circuits for visual cortical plasticity. *Science*, *303*(5664), 1681–1683. https://doi.org/10.1126/science.1091032

Feldman, D. E., & Brecht, M. (2005). Map plasticity in somatosensory cortex. *Science*, *310*(5749), 810–815. https://doi.org/10.1126/science.1115807

Fenno, L., Yizhar, O., & Deisseroth, K. (2011). The development and application of optogenetics. *Annual Review of Neuroscience*, 34, 389–412.

Fino, E., & Yuste, R. (2011). Dense inhibitory connectivity in neocortex. *Neuron*, *69*(6), 1188–1203. https://doi.org/10.1016/j.neuron.2011.02.025

Fries, P., Reynolds, J. H., Rorie, A. E., & Desimone, R. (2001). Modulation of oscillatory neuronal synchronization by selective visual attention. *Science*, *291*(5508), 1560–1563. https://doi.org/10.1126/science.1055465

Froemke, R. C. (2015). Plasticity of cortical excitatory-inhibitory balance. *Annual Review of Neuroscience*, *38*(1), 195–219. https://doi.org/10.1146/annurev-neuro-071714-034002

Galarreta, M., & Hestrin, S. (1998). Frequency-dependent synaptic depression and the balance of excitation and inhibition in the neocortex. *Nature Neuroscience*, *1*(7), 587–594. https://doi.org/10.1038/2822

Garcia del Molino, L. C., Yang, G. R., Mejias, J. F., & Wang, X.-J. (2017). Paradoxical response reversal of top-down modulation in cortical circuits with three interneuron types. *ELife*, *6*. https://doi.org/10.7554/elife.29742

Garcia-Junco-Clemente, P., Tring, E., Ringach, D. L., & Trachtenberg, J. T. (2019). State-dependent subnetworks of parvalbumin-expressing interneurons in neocortex. *Cell Reports*, *26*(9). https://doi.org/10.1016/j.celrep.2019.02.005

Gentet, L. J., Kremer, Y., Taniguchi, H., Huang, Z. J., Staiger, J. F., & Petersen, C. C. (2012). Unique functional properties of somatostatin-expressing GABAergic neurons in mouse barrel cortex. *Nature Neuroscience*, *15*(4), 607–612. https://doi.org/10.1038/nn.3051

Gibson, J. R., Beierlein, M., & Connors, B. W. (1999). Two networks of electrically coupled inhibitory neurons in neocortex. *Nature*, *402*(6757), 75–79. https://doi.org/10.1038/47035

Gilbert, C. D., & Wiesel, T. N. (1979). Morphology and intracortical projections of functionally characterised neurones in the cat visual cortex. *Nature*, *280*(5718), 120–125. https://doi.org/10.1038/280120a0

Glickfeld, L. L., Histed, M. H., & Maunsell, J. H. (2013). Mouse primary visual cortex is used to detect both orientation and contrast changes. *The Journal of Neuroscience*, *33*(50), 19416–19422. https://doi.org/10.1523/jneurosci.3560-13.2013

Goldey, G. J., Roumis, D. K., Glickfeld, L. L., Kerlin, A. M., Reid, R. C., Bonin, V., Schafer, D. P., & Andermann, M. L. (2014). Removable cranial windows for long-term imaging in awake mice. *Nature Protocols*, *9*(11), 2515–2538. https://doi.org/10.1038/nprot.2014.165

Gomez, J. L., Bonaventura, J., Lesniak, W., Mathews, W. B., Sysa‑Shah, P., Rodriguez, L. A., Ellis, R.J., Richie, C.T., Harvey, B.K., Dannals, R.F., Pomper, M.G., Bonci, A., Michaelides, M. (2017). Chemogenetics revealed: DREADD occupancy and activation via converted clozapine. *Science*, 357, 503–507.

Gomez‑Ramirez, M., More, I. A., Pal, A., Connors, B. W., Kauer, J. A., Lipscombe, D., Hochgeschwender, U., Moore, C. I. (2017) Imaging and regulation of cortical neurons using bioluminescent molecules: A biological method for tracking neural dynamics and driving optogenetic elements in vivo. *Society for Neuroscience Abstracts,* 717.11 / VV43.

Gomez‑Ramirez, M., Trzcinski, N. K., Mihalas, S., Niebur, E., & Hsiao, S.S. (2014). Temporal correlation mechanisms and their role in feature selection: A single‑unit study in primate somatosensory cortex. *PLoS Biology*, 12, e1002004. https://doi.org/10.1371/journAl.pbio.1002004

Goris, R. L., Movshon, J. A., & Simoncelli, E. P. (2014). Partitioning neuronal variability. *Nature Neuroscience*, *17*(6), 858–865. https://doi.org/10.1038/nn.3711

Gross, C. (1992). Representation of visual stimuli in inferior temporal cortex. *Philosophical Transactions of the Royal Society of London. Series B: Biological Sciences*, *335*(1273), 3–10. https://doi.org/10.1098/rstb.1992.0001

Guizar-Sicairos, M., Thurman, S. T., & Fienup, J. R. (2008). Efficient subpixel image registration algorithms. *Optics Letters*, *33*(2), 156. https://doi.org/10.1364/ol.33.000156

Gur, M., & Snodderly, D. M. (2008). Physiological differences between neurons in layer 2 and layer 3 of primary visual cortex (V1) of Alert Macaque Monkeys. *The Journal of Physiology*, *586*(9), 2293–2306. https://doi.org/10.1113/jphysiol.2008.151795

Haddock, S. H., Moline, M. A., & Case, J. F. (2010). Bioluminescence in the sea. *Annual Review of Marine Science*, 2, 443–493. https://doi.org/10.1146/annurev-marine-120308-081028

Harris, K. D., & Shepherd, G. M. (2015). The neocortical circuit: Themes and variations. *Nature Neuroscience*, *18*(2), 170–181. https://doi.org/10.1038/nn.3917

Hashemi, A., Golzar, A., Smith, J. E. T., & Cook, E. P. (2018). The magnitude, but not the sign, of Mt Single-trial spike-time correlations predicts motion detection

performance. *The Journal of Neuroscience, 38*(18), 4399–4417. https://doi.org/10.1523/jneurosci.1182-17.2018

Hirsch, J. A., Wang, X., Sommer, F. T., & Martinez, L. M. (2015). How inhibitory circuits in the thalamus serve vision. *Annual Review of Neuroscience, 38*(1), 309–329. https://doi.org/10.1146/annurev-neuro-071013-014229

Histed, M. H., & Maunsell, J. H. (2013). Cortical neural populations can guide behavior by integrating inputs linearly, independent of synchrony. *Proceedings of the National Academy of Sciences, 111*(1). https://doi.org/10.1073/pnas.1318750111

Histed, M. H., Carvalho, L. A., & Maunsell, J. H. (2012). Psychophysical measurement of contrast sensitivity in the behaving mouse. *Journal of Neurophysiology, 107*(3), 758–765. https://doi.org/10.1152/jn.00609.2011

House, D. R. C., Elstrott, J., Koh, E., Chung, J., & Feldman, D. E. (2011). Parallel Regulation of feedforward inhibition and excitation during whisker map plasticity. *Neuron, 72*(5), 819–831. https://doi.org/10.1016/j.neuron.2011.09.008

Houweling, A. R., & Brecht, M. (2008). Behavioural report of single neuron stimulation in somatosensory cortex. *e-Neuroforum, 14*(1), 174–176. https://doi.org/10.1515/nf-2008-0105

Hu, H., Gan, J., & Jonas, P. (2014). Fast-spiking, parvalbumin + GABAergic interneurons: From cellular design to Microcircuit function. *Science, 345*(6196). https://doi.org/10.1126/science.1255263

Hubel, D. H., & Wiesel, T. N. (1959). Receptive fields of single neurones in the Cat's striate cortex. *The Journal of Physiology, 148*(3), 574–591. https://doi.org/10.1113/jphysiol.1959.sp006308

Hubel, D. H., & Wiesel, T. N. (1962). Receptive fields, binocular interaction and functional architecture in the Cat's visual cortex. *The Journal of Physiology, 160*(1), 106–154. https://doi.org/10.1113/jphysiol.1962.sp006837

Hubel, D. H., Wiesel, T. N., & LeVay, S. (1977). Plasticity of ocular dominance columns in monkey striate cortex. *Philosophical transactions of the Royal Society of London. Series B, Biological sciences, 278*(961), 377–409. https://doi.org/10.1098/rstb.1977.0050

Hyvarinen, J., Poranen, A., & Jokinen, Y. (1980). Influence of attentive behavior on neuronal responses to vibration in primary somatosensory cortex of the monkey.

Journal of Neurophysiology, *43*(4), 870–882.
https://doi.org/10.1152/jn.1980.43.4.870

Inagaki, S., & Nagai, T. (2016). Current progress in genetically encoded voltage indicators for neural activity recording. *Current Opinion in Chemical Biology*, 33, 95–100. https://doi.org/10.1016/j.Cbpa.2016.05.023

Inagaki, S., Tsutsui, H., Suzuki, K., Agetsuma, M., Arai, Y., Jinno, Y., Bai, G., Daniels, M.J., Okamura, Y., Matsuda, T., Nagai, T. (2017). Genetically encoded bioluminescent voltage indicator for multi-purpose use in wide range of bioimaging. *Scientific Reports*, 7, 42398. https://doi.org/10.1038/srep4 2398

Jadi, M. P., & Sejnowski, T. J. (2014). Cortical oscillations arise from contextual interactions that regulate sparse coding. *Proceedings of the National Academy of Sciences*, *111*(18), 6780–6785. https://doi.org/10.1073/pnas.1405300111

Jiang, X., Wang, G., Lee, A. J., Stornetta, R. L., & Zhu, J. J. (2013). The organization of two new cortical interneuronal circuits. *Nature Neuroscience*, *16*(2), 210–218. https://doi.org/10.1038/nn.3305

Jones, E. G. (2000). Microcolumns in the cerebral cortex. *Proceedings of the National Academy of Sciences*, *97*(10), 5019–5021. https://doi.org/10.1073/pnas.97.10.5019

Jones, S. R., Pritchett, D. L., Stufflebeam, S. M., Hämäläinen, M., & Moore, C. I. (2007). Neural correlates of tactile detection: A combined magnetoencephalography and biophysically based Computational Modeling Study. *The Journal of Neuroscience*, *27*(40), 10751–10764. https://doi.org/10.1523/jneurosci.0482-07.2007

Kaas, J. H. (2006). Evolution of the Neocortex. *Current Biology*, *16*(21). https://doi.org/10.1016/j.cub.2006.09.057

Kato, H. E., Zhang, F., Yizhar, O., Ramakrishnan, C., Nishizawa, T., Hirata, K., Ito, J., Alta, Y., Tsukazaki, T., Hayashi, S., Hegemann, P., Maturana, A.D., Ishatani, R., Deisseroth, K., Nureki, O. (2012). Crystal structure of the channelrhodopsin light-gated cation channel. *Nature*, 482, 369–374. https://doi.org/10.1038/natur e10870

Kawaguchi Y;Otsuka T;Morishima M;Ushimaru M;Kubota Y; (n.d.). *Control of excitatory hierarchical circuits by parvalbumin-FS basket cells in layer 5 of the frontal*

cortex: Insights for cortical oscillations. Journal of neurophysiology. Retrieved March 29, 2023, from https://pubmed.ncbi.nlm.nih.gov/30995139/

Kerlin, A. M., Andermann, M. L., Berezovskii, V. K., & Reid, R. C. (2010). Broadly tuned response properties of diverse inhibitory neuron subtypes in mouse visual cortex. *Neuron*, *67*(5), 858–871. https://doi.org/10.1016/j.neuron.2010.08.002

Khan, A. G., Poort, J., Chadwick, A., Blot, A., Sahani, M., Mrsic-Flogel, T. D., & Hofer, S. B. (2018). Distinct learning-induced changes in stimulus selectivity and interactions of GABAergic interneuron classes in visual cortex. *Nature Neuroscience*, *21*(6), 851–859. https://doi.org/10.1038/s41593-018-0143-z

Kim, C. K., Adhikari, A., & Deisseroth, K. (2017). Integration of optogenetics with complementary methodologies in systems neuroscience. *Nature Reviews Neuroscience*, 18, 222–235. https://doi.org/10.1038/Nrn.2017.15

Kim, H., Ährlund-Richter, S., Wang, X., Deisseroth, K., & Carlén, M. (2016). Prefrontal parvalbumin neurons in control of attention. *Cell*, *164*(1-2), 208–218. https://doi.org/10.1016/j.cell.2015.11.038

Kleinfeld, D., & Deschênes, M. (2011). Neuronal basis for object location in the VIBRISSA scanning sensorimotor system. *Neuron*, *72*(3), 455–468. https://doi.org/10.1016/j.neuron.2011.10.009

Knoblich, U., Siegle, J. H., Pritchett, D. L., & Moore, C. I. (2010). What do we gain from Gamma? local dynamic gain modulation drives enhanced efficacy and efficiency of signal transmission. *Frontiers in Human Neuroscience*, *04*. https://doi.org/10.3389/fnhum.2010.00185

Knopfel, T., Lin, M. Z., Levskaya, A., Tian, L., Lin, J. Y., & Boyden, E. S. (2010). Toward the second generation of optogenetic tools. *Journal of Neuroscience*, 30, 14998–15004. https://doi.org/10.1523/JNEUROSCI.4190-10.2010

Ko, H., Hofer, S. B., Pichler, B., Buchanan, K. A., Sjöström, P. J., & Mrsic-Flogel, T. D. (2011). Functional specificity of local synaptic connections in neocortical networks. *Nature*, *473*(7345), 87–91. https://doi.org/10.1038/nature09880

Kozai, T. D., & Vazquez, A. L. (2015). Photoelectric artifact from optogenetics and imaging on microelectrodes and bioelectronics: New challenges and opportunities. *Journal of Materials Chemistry B: Materials for Biology and Medicine*, 3, 4965–4978. https://doi.org/10.1039/C5TB0 0108K

Kubota, Y., Kondo, S., Nomura, M., Hatada, S., Yamaguchi, N., Mohamed, A. A., Karube, F., Lübke, J., & Kawaguchi, Y. (2015). Functional effects of distinct innervation styles of pyramidal cells by fast spiking cortical interneurons. *ELife*, *4*. https://doi.org/10.7554/elife.07919

Kubota, Y., Shigematsu, N., Karube, F., Sekigawa, A., Kato, S., Yamaguchi, N., Hirai, Y., Morishima, M., & Kawaguchi, Y. (2011). Selective coexpression of multiple chemical markers defines discrete populations of neocortical GABAergic neurons. *Cerebral Cortex*, *21*(8), 1803–1817. https://doi.org/10.1093/cercor/bhq252

Kwon, S. E., Yang, H., Minamisawa, G., & O'Connor, D. H. (2016). Sensory and decision-related activity propagate in a cortical feedback loop during touch perception. *Nature Neuroscience*, *19*(9), 1243–1249. https://doi.org/10.1038/nn.4356

Lee, S. H., Hjerling-Leffler, J., Zagha, E., Fishell, G., & Rudy, B. (2010). The largest group of superficial neocortical GABAergic interneurons expresses ionotropic serotonin receptors. *The Journal of Neuroscience*, *30*(50), 16796–16808. https://doi.org/10.1523/jneurosci.1869-10.2010

Lee, S., Kruglikov, I., Huang, Z. J., Fishell, G., & Rudy, B. (2013). A disinhibitory circuit mediates motor integration in the somatosensory cortex. *Nature Neuroscience*, *16*(11), 1662–1670. https://doi.org/10.1038/nn.3544 =

Lee, S.-H., Kwan, A. C., & Dan, Y. (2014). Interneurocolumnn subtypes and orientation tuning. *Nature*, *508*(7494). https://doi.org/10.1038/nature13128

Lee, S.-H., Kwan, A. C., Zhang, S., Phoumthipphavong, V., Flannery, J. G., Masmanidis, S. C., Taniguchi, H., Huang, Z. J., Zhang, F., Boyden, E. S., Deisseroth, K., & Dan, Y. (2012). Activation of specific interneurons improves V1 feature selectivity and visual perception. *Nature*, *488*(7411), 379–383. https://doi.org/10.1038/nature11312

Litwin-Kumar, A., & Doiron, B. (2012). Slow dynamics and high variability in balanced cortical networks with clustered connections. *Nature Neuroscience*, *15*(11), 1498–1505. https://doi.org/10.1038/nn.3220

Loomba, S., Straehle, J., Gangadharan, V., Heike, N., Khalifa, A., Motta, A., Ju, N., Sievers, M., Gempt, J., Meyer, H. S., & Helmstaedter, M. (2022). Connectomic comparison of mouse and human cortex. *Science*, *377*(6602). https://doi.org/10.1126/science.abo0924

Lu, J., Tucciarone, J., Lin, Y., & Huang, Z. J. (2014). Input-specific maturation of synaptic dynamics of parvalbumin interneurons in primary visual cortex. *Proceedings of the National Academy of Sciences*, *111*(47), 16895–16900. https://doi.org/10.1073/pnas.1400694111

Luo, T. Z., & Maunsell, J. H. R. (2015). Neuronal modulations in visual cortex are associated with only one of multiple components of attention. *Neuron*, *86*(5), 1182–1188. https://doi.org/10.1016/j.neuron.2015.05.007

MacLaren, D. A., Browne, R. W., Shaw, J. K., Krishnan Radhakrishnan, S., Khare, P., Espana, R. A., & Clark, S. D. (2016). Clozapine N‑oxide administration produces behavioral effects in long‑evans rats: Implications for designing DREADD experiments. *eNeuro*, 3, 1–14.

Maor, I., Shwartz-Ziv, R., Feigin, L., Elyada, Y., Sompolinsky, H., & Mizrahi, A. (2018). Neural correlates of learning pure tones versus natural sounds in the auditory cortex. https://doi.org/10.1101/273342

Marchionni, I., Pilati, N., Forli, A., Sessolo, M., Tottene, A., & Pietrobon, D. (2022). Enhanced feedback inhibition due to increased recruitment of somatostatin-expressing interneurons and enhanced cortical recurrent excitation in a genetic mouse model of Migraine. *The Journal of Neuroscience*, *42*(34), 6654–6666. https://doi.org/10.1523/jneurosci.0228-22.2022

Markram, H., Toledo-Rodriguez, M., Wang, Y., Gupta, A., Silberberg, G., & Wu, C. (2004). Interneurons of the neocortical inhibitory system. *Nature Reviews Neuroscience*, *5*(10), 793–807. https://doi.org/10.1038/nrn1519

Marshel, J. H., Kim, Y. S., Machado, T. A., Quirin, S., Benson, B., Kadmon, J., Raja, C., Chibukhchyan, A., Ramakrishnan, C., Inoue, M., Shane, J. C., McKnight, D. J., Yoshizawa, S., Kato, H. E., Ganguli, S., & Deisseroth, K. (2019). Cortical layer–specific critical dynamics triggering perception. *Science*, *365*(6453). https://doi.org/10.1126/science.aaw5202

McCormick, D. A., Connors, B. W., Lighthall, J. W., & Prince, D. A. (1985). Comparative electrophysiology of pyramidal and sparsely spiny stellate neurons of the neocortex. *Journal of Neurophysiology*, *54*(4), 782–806. https://doi.org/10.1152/jn.1985.54.4.782

Medendorp, W. E., Pal, A., Waddell, M., Björefeldt, A., Moore, C. I., & Hochgeschwender, U. (2020). Selective postnatal excitation of neocortical

pyramidal neurons results in distinctive behavioral and circuit deficits in adulthood. https://doi.org/10.1101/2020.01.18.911347

Meier, P., & Reinagel, P. (2011). Rat performance on visual detection task modeled with divisive normalization and adaptive decision thresholds. *Journal of Vision*, *11*(9), 1–1. https://doi.org/10.1167/11.9.1

Meng, X., Winkowski, D. E., Kao, J. P. Y., & Kanold, P. O. (2017). Sublaminar subdivision of mouse auditory cortex layer 2/3 based on functional Translaminar connections. *The Journal of Neuroscience*, *37*(42), 10200–10214. https://doi.org/10.1523/jneurosci.1361-17.2017

Meynert T. (1867). Der Bau der Grosshirnrinde und seine örtlichen Verschiedenheiten, nebst einem pathologisch-anatomischen Corollarium. *Vierteljschr Psychiat.* 1:77–93, 126–170, 198–217.

Middleton, J. W., Omar, C., Doiron, B., & Simons, D. J. (2012). Neural correlation is stimulus modulated by feedforward inhibitory circuitry. *The Journal of Neuroscience*, *32*(2), 506–518. https://doi.org/10.1523/jneurosci.3474-11.2012

Miller, K. D., Pinto, D. J., & Simons , D. J. (2001). Processing in layer 4 of the neocortical circuit: New insights from visual and somatosensory cortex. *Current Opinion in Neurobiology*, *11*(4), 488–497. https://doi.org/10.1016/s0959-4388(00)00239-7

Minces, V., Pinto, L., Dan, Y., & Chiba, A. A. (2017). Cholinergic shaping of neural correlations. *Proceedings of the National Academy of Sciences*, *114*(22), 5725–5730. https://doi.org/10.1073/pnas.1621493114

Miska, N. J., Richter, L. M. A., Cary, B. A., Gjorgjieva, J., & Turrigiano, G. G. (2018). Sensory experience inversely regulates feedforward and feedback excitation-inhibition ratio in rodent visual cortex. *ELife*, *7*. https://doi.org/10.7554/elife.38846

Mitchell, J. F., Sundberg, K. A., & Reynolds, J. H. (2007). Differential attention-dependent response modulation across cell classes in macaque visual area V4. *Neuron*, *55*(1), 131–141. https://doi.org/10.1016/j.neuron.2007.06.018

Montijn, J. S., Goltstein, P. M., & Pennartz, C. M. A. (2015). Mouse V1 population correlates of visual detection rely on heterogeneity within neuronal response patterns. *ELife*, *4*. https://doi.org/10.7554/elife.10163

Moore, C. I., Crosier, E., Greve, D. N., Savoy, R., Merzenich, M. M., & Dale, A. M. (2013). Neocortical correlates of vibrotactile detection in humans. *Journal of Cognitive Neuroscience*, *25*(1), 49–61. https://doi.org/10.1162/jocn_a_00315

Moran, J., & Desimone, R. (1985). Selective attention gates visual processing in the extrastriate cortex. *Science*, *229*(4715), 782–784. https://doi.org/10.1126/science.4023713

Moreno-Bote, R., Beck, J., Kanitscheider, I., Pitkow, X., Latham, P., & Pouget, A. (2014). Information-limiting correlations. *Nature Neuroscience*, *17*(10), 1410–1417. https://doi.org/10.1038/nn.3807

Mountcastle, V. B. (1957). Modality and topographic properties of single neurons of CAT's somatic sensory cortex. *Journal of Neurophysiology*, *20*(4), 408–434. https://doi.org/10.1152/jn.1957.20.4.408

Mountcastle, V. B., LaMotte, R. H., & Carli, G. (1972). Detection thresholds for stimuli in humans and monkeys: Comparison with threshold events in mechanoreceptive afferent nerve fibers innervating the monkey hand. *Journal of Neurophysiology*, *35*(1), 122–136. https://doi.org/10.1152/jn.1972.35.1.122

Naka, A., Veit, J., Shababo, B., Chance, R. K., Risso, D., Stafford, D., Snyder, B., Egladyous, A., Chu, D., Sridharan, S., Mossing, D. P., Paninski, L., Ngai, J., & Adesnik, H. (2019). Complementary networks of cortical somatostatin interneurons enforce layer specific control. *ELife*, *8*. https://doi.org/10.7554/elife.43696

Naumann, E. A., Kampff, A. R., Prober, D. A., Schier, A. F., & Engert, F. (2010). Monitoring neural activity with bioluminescence during natural behavior. *Nature Neuroscience*, 13, 513–520. https://doi.org/10.1038/nn.2518

Nichols, C. D., & Roth, B. L. (2009). Engineered G‑protein coupled receptors are powerful tools to investigate biological processes and behaviors. *Frontiers in Molecular Neuroscience*, 2, 1–10.

O'Connor, D. H., Clack, N. G., Huber, D., Komiyama, T., Myers, E. W., & Svoboda, K. (2010). Vibrissa-based object localization in head-fixed mice. *The Journal of Neuroscience*, *30*(5), 1947–1967. https://doi.org/10.1523/jneurosci.3762-09.2010

Olsen, S. R., Bortone, D. S., Adesnik, H., & Scanziani, M. (2012). Gain control by layer six in cortical circuits of Vision. *Nature*, *483*(7387), 47–52. https://doi.org/10.1038/nature10835

Pal, A., Gomez-Ramirez, M., Medendrop, W. E., Zaidi, Z., Kauer, J. A., Lipscombe, D., Connors, B.W., Moore, C.I., Hochgeschwender, U. (2017) Characterization, subcellular targeting and novel applications of a split Gaussia luciferase based genetically encoded calcium indicator. *Society for Neuroscience Abstract*, 717.11 / VV44.

Palagina, G., Meyer, J. F., & Smirnakis, S. M. (2017). Complex visual motion representation in Mouse Area V1. *The Journal of Neuroscience*, *37*(1), 164–183. https://doi.org/10.1523/jneurosci.0997-16.2017

Park, S. Y., Song, S. H., Palmateer, B., Pal, A., Petersen, E. D., Shall, G. P., Welchko, R.M., Hochgeschwender, U. (2017). Novel luciferase-opsin combinations for improved luminopsins. *Journal of Neuroscience Research*, 98(3), 410–421. https://doi.org/10.1002/jnr.24152

Pashaie, R., & Falk, R. (2013). Single optical fiber probe for fluorescence detection and optogenetic stimulation. *IEEE Transactions on Biomedical Engineering*, 60, 268–280. https://doi.org/10.1109/TBME.2012.2221713

Peron, S. P., Freeman, J., Iyer, V., Guo, C., & Svoboda, K. (2015). A cellular resolution map of barrel cortex activity during tactile behavior. *Neuron*, *86*(3), 783–799. https://doi.org/10.1016/j.neuron.2015.03.027

Petersen, C. C., Hahn, T. T., Mehta, M., Grinvald, A., & Sakmann, B. (2003). Interaction of sensory responses with spontaneous depolarization in layer 2/3 barrel cortex. *Proceedings of the National Academy of Sciences*, *100*(23), 13638–13643. https://doi.org/10.1073/pnas.2235811100

Pinto, D. J., Brumberg, J. C., & Simons, D. J. (2000). Circuit dynamics and coding strategies in rodent somatosensory cortex. *Journal of Neurophysiology*, *83*(3), 1158–1166. https://doi.org/10.1152/jn.2000.83.3.1158

Pinto, L., Goard, M. J., Estandian, D., Xu, M., Kwan, A. C., Lee, S.-H., Harrison, T. C., Feng, G., & Dan, Y. (2013). Fast modulation of visual perception by basal forebrain cholinergic neurons. *Nature Neuroscience*, *16*(12), 1857–1863. https://doi.org/10.1038/nn.3552

Plomp, G., Larderet, I., Fiorini, M., & Busse, L. (2018). Layer 3 dynamically coordinates columnar activity according to spatial context. https://doi.org/10.1101/277533

Poulet, J. F., & Petersen, C. C. (2008). Internal Brain State regulates membrane potential synchrony in barrel cortex of behaving mice. *Nature*, *454*(7206), 881–885. https://doi.org/10.1038/nature07150

Prakash, M., Medendorp, W. E., & Hochgeschwender, U. (2018). Defining parameters of specificity for bioluminescent optogenetic activation of neurons using in vitro multi electrode arrays (MEA). *Journal of Neuroscience Research*, 98(3), 437–447. https://doi.org/10.1002/Jnr.24313

Pritchett, D. L., Siegle, J. H., Deister, C. A., & Moore, C. I. (2015). For things needing your attention: The role of neocortical gamma in sensory perception. *Current Opinion in Neurobiology*, *31*, 254–263. https://doi.org/10.1016/j.conb.2015.02.004

Ramon y Cajal, S. (1911). Histologie du systeme nerveux de l'Homme et des vertebres. *Maloine (Paris)*, *2*, 891-942.

Renart, A., de la Rocha, J., Bartho, P., Hollender, L., Parga, N., Reyes, A., & Harris, K. D. (2010). The asynchronous state in cortical circuits. *Science*, *327*(5965), 587–590. https://doi.org/10.1126/science.1179850

Ress, D., Backus, B. T., & Heeger, D. J. (2000). Activity in primary visual cortex predicts performance in a visual detection task. *Nature Neuroscience*, *3*(9), 940–945. https://doi.org/10.1038/78856

Reynolds, J. H., Pasternak, T., & Desimone, R. (2000). Attention increases sensitivity of V4 neurons. *Neuron*, *26*(3), 703–714. https://doi.org/10.1016/s0896-6273(00)81206-4

Reynolds, J. H., Pasternak, T., & Desimone, R. (2000). Attention increases sensitivity of V4 neurons. *Neuron*, *26*(3), 703–714. https://doi.org/10.1016/s0896-6273(00)81206-4

Rigotti, M., Barak, O., Warden, M. R., Wang, X.-J., Daw, N. D., Miller, E. K., & Fusi, S. (2013). The importance of mixed selectivity in complex cognitive tasks. *Nature*, *497*(7451), 585–590. https://doi.org/10.1038/nature12160

Rikhye, R. V., Hu, M., Yildirim, M., & Sur, M. (2017). Reliable sensory processing in mouse visual cortex through inhibitory interactions between somatostatin and parvalbumin interneurons. https://doi.org/10.1101/187062

Rikhye, R. V., Yildirim, M., Hu, M., Breton-Provencher, V., & Sur, M. (2021). Reliable sensory processing in mouse visual cortex through cooperative interactions

between somatostatin and parvalbumin interneurons. *The Journal of Neuroscience*, *41*(42), 8761–8778. https://doi.org/10.1523/jneurosci.3176-20.2021

Ringach, D. L., Mineault, P. J., Tring, E., Olivas, N. D., Garcia-Junco-Clemente, P., & Trachtenberg, J. T. (2016). Spatial clustering of tuning in mouse primary visual cortex. *Nature Communications*, *7*(1). https://doi.org/10.1038/ncomms12270

Romo, R., & Salinas, E. (2003). Flutter discrimination: Neural codes, perception, memory and decision making. *Nature Reviews Neuroscience*, *4*(3), 203–218. https://doi.org/10.1038/nrn1058

Roth, B. L. (2016). DREADDs for neuroscientists. *Neuron,* 89, 683–694.

Ruff, D. A., & Cohen, M. R. (2014). Attention can either increase or decrease spike count correlations in visual cortex. *Nature Neuroscience*, *17*(11), 1591–1597. https://doi.org/10.1038/nn.3835

Runyan, C. A., & Sur, M. (2013). Response selectivity is correlated to dendritic structure in parvalbumin-expressing inhibitory neurons in visual cortex. *Journal of Neuroscience*, *33*(28), 11724–11733. https://doi.org/10.1523/jneurosci.2196-12.2013

Sachidhanandam, S., Sermet, B. S., & Petersen, C. C. H. (2016). Parvalbumin-expressing GABAergic neurons in mouse barrel cortex contribute to gating a goal-directed sensorimotor transformation. *Cell Reports*, *15*(4), 700–706. https://doi.org/10.1016/j.celrep.2016.03.063

Sachidhanandam, S., Sreenivasan, V., Kyriakatos, A., Kremer, Y., & Petersen, C. C. (2013). Membrane potential correlates of sensory perception in mouse barrel cortex. *Nature Neuroscience*, *16*(11), 1671–1677. https://doi.org/10.1038/nn.3532

Saito, K., Chang, Y. F., Horikawa, K., Hatsugai, N., Higuchi, Y., Hashida, M., Yoshida, Y., Matsuda, T., Arai, Y., Nagai, T. (2012). Luminescent proteins for high‑speed single cell and whole‑body imaging. *Nature Communications*, 3, 1262. https://doi.org/10.1038/ncomm s2248

Schröder, R., & Luhmann, H. J. (1997). Morphology, electrophysiology and pathophysiology of supragranular neurons in rat primary somatosensory cortex. *European Journal of Neuroscience*, *9*(1), 163–176. https://doi.org/10.1111/j.1460-9568.1997.tb01364.x

Shadlen, M. N., & Newsome, W. T. (1998). The variable discharge of cortical neurons: Implications for connectivity, computation, and information coding. *The Journal of Neuroscience*, *18*(10), 3870–3896. https://doi.org/10.1523/jneurosci.18-10-03870.1998

Sherfey, J., Ardid, S., Miller, E. K., Hasselmo, M. E., & Kopell, N. J. (2020). Prefrontal oscillations modulate the propagation of neuronal activity required for working memory. *Neurobiology of Learning and Memory*, *173*, 107228. https://doi.org/10.1016/j.nlm.2020.107228

Sheets, P. L., & Shepherd, G. M. G. (2011). Cortical circuits for motor control. *Neuropsychopharmacology*, *36*(1), 365–366. https://doi.org/10.1038/npp.2010.146

Shin, H., & Moore, C. I. (2019). Persistent gamma spiking in SI nonsensory fast spiking cells predicts perceptual success. *Neuron*, *103*(6). https://doi.org/10.1016/j.neuron.2019.06.014

Siegel, M., Buschman, T. J., & Miller, E. K. (2015). Cortical information flow during flexible sensorimotor decisions. *Science*, *348*(6241), 1352–1355. https://doi.org/10.1126/science.aab0551

Simons, D. J., & Carvell, G. E. (1989). Thalamocortical response transformation in the rat vibrissa/barrel system. *Journal of Neurophysiology*, *61*(2), 311–330. https://doi.org/10.1152/jn.1989.61.2.311

Smith, J. E., Zhan, C. A., & Cook, E. P. (2011). The functional link between Area MT neural fluctuations and detection of a brief motion stimulus. *The Journal of Neuroscience*, *31*(38), 13458–13468. https://doi.org/10.1523/jneurosci.1347-11.2011

Stüttgen, M. C., & Schwarz, C. (2008). Psychophysical and neurometric detection performance under stimulus uncertainty. *Nature Neuroscience*, *11*(9), 1091–1099. https://doi.org/10.1038/nn.2162

Sur, M., Merzenich, M. M., & Kaas, J. H. (1980). Magnification, receptive-field area, and "hypercolumn" size in areas 3b and 1 of somatosensory cortex in Owl Monkeys. *Journal of Neurophysiology*, *44*(2), 295–311. https://doi.org/10.1152/jn.1980.44.2.295

Swadlow, H. A. (2002). Thalamocortical control of feed–forward inhibition in awake somatosensory 'barrel' cortex. *Philosophical Transactions of the Royal Society of London. Series B: Biological Sciences*, *357*(1428), 1717–1727. https://doi.org/10.1098/rstb.2002.1156

Takahashi, N., Oertner, T. G., Hegemann, P., & Larkum, M. E. (2016). Active cortical dendrites modulate perception. *Science*, *354*(6319), 1587–1590. https://doi.org/10.1126/science.aah6066

Tiesinga, P. H., Fellous, J.-M., Salinas, E., José, J. V., & Sejnowski, T. J. (2004). Inhibitory synchrony as a mechanism for attentional gain modulation. *Journal of Physiology-Paris*, *98*(4-6), 296–314. https://doi.org/10.1016/j.jphysparis.2005.09.002

Tomm, C., Floyd Sarria, J.-C., & Petersen, C. C. H. (2009). The excitatory neuronal network of the C2 barrel column in mouse primary somatosensory cortex. *Neuron*, *61*(2), 301–316. https://doi.org/10.1016/j.neuron.2008.12.020

Tsao, D. Y., & Livingstone, M. S. (2008). Mechanisms of face perception. *Annual Review of Neuroscience*, *31*(1), 411–437. https://doi.org/10.1146/annurev.neuro.30.051606.094238

Tung, J. K., Gutekunst, C.-A., & Gross, R. E. (2015). Inhibitory luminopsins: Genetically-encoded bioluminescent opsins for versatile, scalable and hardware-independent optogenetic inhibition. *Scientific Reports*, *5*(1). https://doi.org/10.1038/srep14366

Tung, J. K., Shiu, F. H., Ding, K., & Gross, R. E. (2018). Chemically activated luminopsins allow optogenetic inhibition of distributed nodes in an epileptic network for non-invasive and multi-site suppression of seizure activity. *Neurobiology of Diseases,* 109, 1–10. https://doi.org/10.1016/j.nbd.2017.09.007

Urban, D. J., & Roth, B. L. (2015). DREADDs (designer receptors exclusively activated by designer drugs): Chemogenetic tools with therapeutic utility. Annual Review of Pharmacology and Toxicology, 55, 399–417. https://doi.org/10.1146/annurev-pharmtox-010814-124803

Veit, J., Hakim, R., Jadi, M. P., Sejnowski, T. J., & Adesnik, H. (2017). Cortical gamma band synchronization through somatostatin interneurons. *Nature Neuroscience*, *20*(7), 951–959. https://doi.org/10.1038/nn.4562

Vinje, W. E., & Gallant, J. L. (2000). Sparse coding and decorrelation in primary visual cortex during natural vision. *Science*, *287*(5456), 1273–1276. https://doi.org/10.1126/science.287.5456.1273

Vogels, T. P., & Abbott, L. F. (2009). Gating multiple signals through detailed balance of excitation and inhibition in spiking networks. *Nature Neuroscience*, *12*(4), 483–491. https://doi.org/10.1038/nn.2276

Vogels, T. P., Froemke, R. C., Doyon, N., Gilson, M., Haas, J. S., Liu, R., Maffei, A., Miller, P., Wierenga, C. J., Woodin, M. A., Zenke, F., & Sprekeler, H. (2013). Inhibitory synaptic plasticity: Spike timing-dependence and putative network function. *Frontiers in Neural Circuits*, *7*. https://doi.org/10.3389/fncir.2013.00119

Voigts, J., Deister, C. A., & Moore, C. I. (2020). Layer 6 ensembles can selectively regulate the behavioral impact and layer-specific representation of sensory deviants. *ELife*, *9*. https://doi.org/10.7554/elife.48957

Wang, C.-T., Lee, C.-T., Wang, X.-J., & Lo, C.-C. (2013). Top-down modulation on perceptual decision with balanced inhibition through feedforward and feedback inhibitory neurons. *PLoS ONE*, *8*(4). https://doi.org/10.1371/journal.pone.0062379

Wang, X.-J., & Buzsáki, G. (1996). Gamma oscillation by synaptic inhibition in a hippocampal Interneuronal network model. *The Journal of Neuroscience*, *16*(20), 6402–6413. https://doi.org/10.1523/jneurosci.16-20-06402.1996

Wang, X.-J., & Yang, G. R. (2018). A disinhibitory circuit motif and flexible information routing in the brain. *Current Opinion in Neurobiology, 49*, 75–83. https://doi.org/10.1016/j.conb.2018.01.002

Wehr, M., & Zador, A. M. (2003). Balanced inhibition underlies tuning and sharpens spike timing in auditory cortex. *Nature*, *426*(6965), 442–446. https://doi.org/10.1038/nature02116

Weiler, S., Guggiana Nilo, D., Bonhoeffer, T., Hübener, M., Rose, T., & Scheuss, V. (2022). Functional and structural features of L2/3 pyramidal cells continuously covary with pial depth in mouse visual cortex. *Cerebral Cortex*. https://doi.org/10.1093/cercor/bhac303

Welsh, J. P., Patel, K. G., Manthiram, K., & Swartz, J. R. (2009). Multiply mutated Gaussia luciferases provide prolonged and intense bioluminescence. *Biochemical and Biophysical Research Communications*, 389, 563–568. https://doi.org/10.1016/j.bbrc.2009.09.006

Wilson, N. R., Runyan, C. A., Wang, F. L., & Sur, M. (2012). Division and subtraction by distinct cortical inhibitory networks in vivo. *Nature*, *488*(7411), 343–348. https://doi.org/10.1038/nature11347

Xu, H., Jeong, H.-Y., Tremblay, R., & Rudy, B. (2013). Neocortical somatostatin-expressing GABAergic interneurons disinhibit the thalamorecipient layer 4. *Neuron*, *77*(1), 155–167. https://doi.org/10.1016/j.neuron.2012.11.004

Xu, X., & Callaway, E. M. (2009). Laminar specificity of functional input to distinct types of inhibitory cortical neurons. *The Journal of Neuroscience*, 29(1), 70–85. https://doi.org/10.1523/jneurosci.4104-08.2009

Xue, M., Atallah, B. V., & Scanziani, M. (2014). Equalizing excitation–inhibition ratios across visual cortical neurons. *Nature*, *511*(7511), 596–600. https://doi.org/10.1038/nature13321

Yamamori, T., & Rockland, K. S. (2006). Neocortical areas, layers, connections, and gene expression. *Neuroscience Research*, *55*(1), 11–27. https://doi.org/10.1016/j.neures.2006.02.006

Yamashita, T., & Petersen, C. C. H. (2016). Target-specific membrane potential dynamics of neocortical projection neurons during goal-directed behavior. *ELife*, *5*. https://doi.org/10.7554/elife.15798

Yang, H., Kwon, S. E., Severson, K. S., & O'Connor, D. H. (2015). Origins of choice-related activity in mouse somatosensory cortex. *Nature Neuroscience*, *19*(1), 127–134. https://doi.org/10.1038/nn.4183

Yizhar, O., Fenno, L. E., Prigge, M., Schneider, F., Davidson, T. J., O'Shea, D. J., Sohal, V. S., Goshen, I., Finkelstein, J., Paz, J. T., Stehfest, K., Fudim, R., Ramakrishnan, C., Huguenard, J. R., Hegemann, P., & Deisseroth, K. (2011). Neocortical excitation/inhibition balance in information processing and social dysfunction. *Nature*, *477*(7363), 171–178. https://doi.org/10.1038/nature10360

Zenchak, J. R., Palmateer, B., Dorka, N., Brown, T. M., Wagner, L. M., Medendorp, W.E., Petersen, E.D., Prakash, M., Hochgeschwender, U. (2018). Bioluminescence-driven optogenetic activation of transplanted neural precursor cells improves motor deficits in a Parkinson's disease mouse model. *Journal of Neuroscience Research*, 98(3), 458–468. https://doi.org/10.1002/jnr.24237

Zhang, F., Prigge, M., Beyriere, F., Tsunoda, S. P., Mattis, J., Yizhar, O., Hegemann, P., Deisseroth, K. (2008). Red-shifted optogenetic excitation: A tool for fast neural control derived from Volvox carteri. Nature Neuroscience, 11, 631–633. https://doi.org/10.1038/nn.2120

Zhang, F., Wang, L. P., Boyden, E. S., & Deisseroth, K. (2006). Channelrhodopsin-2 and optical control of excitable cells. *Nature Methods*, 3, 785–792. https://doi.org/10.1038/nmeth936

Zhang, S., Xu, M., Kamigaki, T., Hoang Do, J. P., Chang, W.-C., Jenvay, S., Miyamichi, K., Luo, L., & Dan, Y. (2014). Long-range and local circuits for top-down modulation of visual cortex processing. *Science*, *345*(6197), 660–665. https://doi.org/10.1126/science.1254126

Zhu, Y., Feng, B., Schwartz, E. S., Gebhart, G. F., & Prescott, S. A. (2015). Novel method to assess axonal excitability using channelrhodopsin-based photoactivation. *Journal of Neurophysiology*, 113, 2242–2249.https://doi.org/10.1152/jn.00982.2014